

**FINAL REPORT
PART I
The Study of Space Communications Spread
Spectrum Systems**

REPORT 90-1

PREPARED FOR THE DEPARTMENT OF COMMUNICATIONS

UNDER DSS CONTRACT NO. 36001-8-3528/01-SS

**SAW-BASED JOINT GROUP DEMODULATION
OF FREQUENCY SHIFT KEYED AND
DIFFERENTIAL PHASE SHIFT KEYED SIGNALS**

IC



Department of Electrical Engineering

Queen's University at Kingston

Kingston, Ontario, Canada

LKC
TK
5103.45
.S888
1990
V.1
C.2

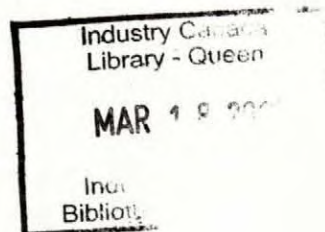
**FINAL REPORT
PART I
The Study of Space Communications Spread
Spectrum Systems**

REPORT 90-1

PREPARED FOR THE DEPARTMENT OF COMMUNICATIONS

UNDER DSS CONTRACT NO. 36001-8-3528/01-SS

**SAW-BASED JOINT GROUP DEMODULATION
OF FREQUENCY SHIFT KEYED AND
DIFFERENTIAL PHASE SHIFT KEYED SIGNALS**



TIC
S102.5
S888
1990
P.t. 1
S-Gen

FINAL REPORT

PART I

The Study of Space Communications Spread Spectrum Systems

REPORT 90-1

PREPARED FOR THE DEPARTMENT OF COMMUNICATIONS

UNDER DSS CONTRACT NO. 36001-8-3528/01-SS

**SAW - BASED JOINT GROUP DEMODULATION OF FREQUENCY
SHIFT KEYED AND DIFFERENTIAL PHASE SHIFT KEYED SIGNALS**

by

Peter T. Traynor

Peter J. McLane

Department of Electrical Engineering

Queen's University

Kingston, Ontario, Canada

March, 1990

SAW - BASED JOINT GROUP DEMODULATION
OF FREQUENCY SHIFT KEYED AND
DIFFERENTIAL PHASE SHIFT KEYED SIGNALS

by

Peter T. Traynor

Peter J. McLane

FINAL REPORT

PART I

DSS CONTRACT NO. 36001-8-3528/01-SS

Department of Electrical Engineering

Queen's University

Kingston, Ontario, Canada

March, 1990

Abstract

A surface acoustic wave (SAW) device based processor, capable of the joint group demodulation of FSK and DPSK signals, and intended for use in the Canadian EHF Satcom system is proposed. The processor is based on the ability of SAW filters to implement wide-band, real-time, Fourier transforms with an observation interval corresponding to the hop period of the system. The background for such an implementation is given. The SAW-based transforms are simulated using digital Fourier Transforms, and a quasi-analytical technique is applied to determine bit error rate performance of both binary and quaternary differential phase shift keying in the presence of narrow-band Gaussian noise. Signal parameters such as windowing, carrier separation, user bandwidth allocations, and non-linear characteristics of the SAW devices are also considered. Based on the results determined in this study, the SAW-based processor is capable of performing group DPSK demodulation. The maximum number of DPSK users depends on the time-bandwidth product of the SAW devices used in the implementation, varying from 3 users for $TB=512$ to 12 users for $TB=2048$. It is also shown that DBPSK consistently out-performs DQPSK for this application.

Contents

	Page
Abstract	<i>i</i>
Table of Contents	<i>ii</i>
List of Figures	<i>iv</i>
List of Tables	<i>vi</i>
Glossary of Abbreviations	<i>vii</i>
Glossary of Mathematical Notations	<i>viii</i>
Chapter 1	
1.1 Introduction	1
1.2 Satellite System Model	6
1.3 Literature Review	8
1.4 Presentation Outline	12
1.5 Contributions	13
Chapter 2	
2.1 Signalling Format and Group demodulation	14
2.2 FSK demodulation	21
2.3 DPSK demodulation	24
Chapter 3	
3.1 The Chirp Fourier Transform	32
3.2 The M-C-M Chirp Fourier Transform Arrangement	35
3.3 The C-M-C Arrangement	45
3.4 The Inverse Fourier Transform Processor	53
3.5 The Joint Group Demodulator	55
Chapter 4	
4.1 Simulation Methodology	59
4.2 Probability of Error Calculations	62
4.3 Computational Considerations	80

Chapter 5		
5.1	Outline of Simulation results	83
5.2	Windowing Considerations	84
5.3	Transform Truncation Considerations	96
5.4	Varying TB product SAW Devices	102
5.5	Non-linear Phase and Amplitude Response	117
Chapter 6		
6.1	Conclusions	131
6.2	Suggestions for Future Work	133
References		134
Appendix A		
A.1	SAW devices	137
A.2	Implementation Considerations	162

List Of Figures

1.1	The On-Board processing concept	2
1.2	Satellite Processor System Model	7
1.3	Felsteads Proposed Demodulator	9
2.1	Uplink Signalling Pattern For N FSK and L DPSK users	15
2.2	Fourier Transform Based Group Demodulation Technique	17
2.3	Signal Timing and Bandwidth Allocations	20
2.4	LDR Demodulator Time Mapping for Quaternary FSK	23
2.5	Fourier Transform of a Baseband DPSK Signal	27
2.6	Spectrum Truncation for DPSK Demodulation	29
3.1	The M-C-M and C-M-C configurations	34
3.2	Convolution of Rectangular Gating Functions	39
3.3	Processing FSK tones in the C-M-C arrangement with ping-pong multipliers	49
3.4	The Group Demodulator based on the 100% duty cycle C-M-C configuration	56
4.1	Methodology of Analysis	61
4.2	Detector Structure for Quaternary DPSK	63
4.3	Undistorted and Distorted Pulse Shapes	66
4.4	Phase Angle Between Two Vectors Perturbed by Gaussian Noise	70
4.5	Decision Boundaries for DQPSK	71
4.6	Decision Boundaries for DBPSK	77
4.7	Generalized BER/waveform algorithm	82
5.1	Windows Examined	86
5.2	Input binary Sequence	87
5.3	FFT Output with One Active User	88
5.4	One Active User with Rectangular Windowing of the Transform	89
5.5	One Active User with a Kaiser-Bessel Window on the Transform	91
5.6	Simulated Spectral Output for Two Active Users with $\Delta f_u = 2/T$	92
5.7	Two Active Users with a Kaiser-Bessel Window on the Transform	94
5.8	Fourier Transform of the Windowing Functions	95
5.9	BER Performance for DBPSK with Varying Δf_u	97
5.10	Power Spectral Densities of Quaternary and Binary DPSK	100

5.11	Fractional in-band Power of Quaternary and Binary DPSK	101
5.12	Modified Sample Input Sequence	104
5.13	Sample Output with TB = 512	105
5.14	Sample Waveform Output, TB = 1024	107
5.15	Sample Waveform Output, TB = 2048	108
5.16	BER Results for DBPSK	109
5.17	BER Results for DQPSK	110
5.18	BER Results for DBPSK with Two Interfering Users at Equal Power	112
5.19	BER Results for DQPSK with Two Interfering Users at Equal Power	113
5.20	BER Results for DBPSK with Two Interfering Users at 10 dB greater Power than the Reference User	114
5.21	BER Results for DQPSK with Two Interfering Users at 10 dB greater Power than the Reference User	115
5.22	Modified Processor Model	120
5.23	Amplitude and Phase non-linearities for the Demodulator with TB = 512	122
5.24	Amplitude and Phase non-linearities for the Demodulator with TB = 1024	123
5.25	Sample Waveform Output with $\Phi(f)=0$	124
5.26	Sample Waveform Output with $\Phi(f)=15p-p$	125
5.27	Sample Waveform Output with $\Phi(f)=30p-p$	126
5.28	BER Results for DBPSK with Processor Incorporating Non-linearities	127
5.29	BER Results for DQPSK with Processor Incorporating Non-linearities	129
A.1	Propagation of An Acoustic Wave	139
A.2	The Interdigital Transducer	142
A.3	The Cross-field and In-line Electric Field Approximations	144
A.4	$E\theta(z)$ for a Uniform IDT	147
A.5	Input/Output IDT pairs	150
A.6	Finger-pair overlap (apodization) to Achieve an Arbitrary Amplitude Response	152
A.7	An Input/Output Amplitude Apodized IDT pair	154
A.8	Chirped Waveform and Corresponding Impulse Amplitudes	161
A.9	Dummy and Double Electrode Structures	164

List of Tables

3.1	Dualism of the C-M-C and C-M-C configurations	46
3.2	Critical Processor Parameters for a Processor with an Analysed Bandwidth of 2.56 MHz	52
3.3	Generalized SAW Device Characteristics for the IFT Processor	54
3.4	Critical Parameters for the FT Processor with an Analysed Bandwidth of 20.48 MHz	57
3.5	Critical Parameters for the IFT Processor with an Analysed Bandwidth of 5 MHz	58
5.1	DFT/SAW Processor Parameters	103
A.1	Finger Placements and Apodizations for the TB=512 Chirped Waveform Filter	166
A.2	Finger Placements and Apodizations for the TB=1024 Chirped Waveform Filter	166

Glossary of Abbreviations

ACI	Adjacent Channel Interference
bps	Bits per second
CFT	Chirp Fourier Transform
C-M-C	Convolve-Multiply-Convolve (arrangement)
DFT	Digital Fourier Transform
DPSK	Differential Phase Shift Keying
DS/PN	Direct Sequence/Pseudo Noise
EHF	Extremely High Frequency
FDMA	Frequency Division Multiple Access
FFT	Fast Fourier Transform
FH	Frequency Hopping
FSK	Frequency Shift Keying
FT	Fourier Transform
IDT	Interdigital Transducer
IF	Intermediate Frequency
IFT	Inverse Fourier Transform
LDR	Low Data Rate
M-C-M	Multiply-Convolve-Multiply (arrangement)
MDR	Medium Data Rate
pdf	Probability Density Function
p-p	Peak to Peak
RAC	Reflective Array Compressor
SatCom	Satellite Communications

SAW	Surface Acoustic Wave
SNR	Signal to Noise Ratio
T1	Data Transmission Rate of 1.54 Mbps
TB	Time-Bandwidth Product
TDM	Time Division Multiple Access

Glossary of Mathematical Notations

$A_k(t)$	Distorted Pulse shape over the k^{th} baud interval
B_{dpsk}	DPSK portion of B_{IF}
B_{fsk}	FSK portion of B_{IF}
B_{IF}	Intermediate Frequency Bandwidth
$C_1(t)$	Premultiplication chirp in M-C-M
$C'_1(t)$	First convolution filter in C-M-C
$C_2(t)$	Post Multiplication chirp in M-C-M
$C'_2(t)$	Second convolution filter in C-M-C
$D_j(t)$	j^{th} DPSK user's sequence
$D_{jk}(t)$	DPSK symbol on k^{th} baud in j^{th} hop
f_{cj}	Carrier frequency of DPSK user j
δf	Frequency offset on f_{cj}
f_i	i^{th} user's FSK tone
δf_i	Frequency offset on the i^{th} user's FSK tone
$F(\psi)$	Distribution function of ψ
$F(\psi \Delta\phi)$	Distribution function of ψ with condition that $\Delta\phi$ is sent
$F(\Omega)$	CFT of $f(t)$
$g(t)$	Pulse shape of a DPSK symbol

$H_0(t)$	Convolution filter in M-C-M
$H'_0(t)$	Multiplication filter in C-M-C
K^2	Piezoelectric coupling factor
L	Number of DPSK users
N	Number of FSK users
N_w	Number of discrete points in window
$n(t)$	Additive Gaussian Noise
$p(\psi)$	Probability density function of ψ
$P(E \Delta\phi_k, \rho_k, \rho_{k-1})$	Probability of symbol error given the received vector with ϕ_k , ρ_k , and ρ_{k-1}
$P_{be}(M)$	Average bit error probability for M-ary DPSK
$P_{be}(M D_j)$	Conditional probability of bit error, given that the j^{th} sequence of ξ DPSK symbols is sent
$P_{be}^k(M)$	Probability of bit error on the k^{th} baud of M-ary DPSK
$P_{se}^k(M I_j)$	$P_{be}(M)$ conditioned on the presence of interference condition I_j
$P_{se}^k(M)$	Probability of symbol error on the k^{th} baud of M-ary DPSK
R_{ck}	In-phase component of noise corrupted and sampled DPSK symbol
R_{sk}	Quaterature component of noise corrupted and sampled DPSK symbol
$S_i(t)$	i^{th} FSK user's tone
T_b	time duration of DPSK symbol

T_H	Frequency Hop Period
v_o	SAW velocity with conducting surface present
v_r	SAW velocity (electrically free surface)
$w_f(t)$	Windowing function for FSK detection
$W(f)$	Fourier Transform of $w_f(t)$
$W_i(t)$	Amplitude weighting of i^{th} SAW device
X_k	Integrated and sampled pulse over the k^{th} baud interval
Y_k	Integrated and sampled pulse over the k^{th} baud interval
Z	z-direction length of the IDT
β	Bandwidth expansion factor of window
Δf_u	Bandwidth allocated to each DPSK user
$\Delta \phi_k$	$\phi(t+T) - \phi(t)$
ϵf	FSK demodulator frequency resolution
η	$B_{\text{fsk}} / B_{\text{IF}}$
$\theta_i(t)$	Phase jitter on the i^{th} user's FSK tone
θ_i	Random phase offset on the i^{th} FSK tone
θ_j	Phase offset on f_{cj}
$\theta_k(t)$	Noise corrupted version of ϕ_k
μ	$d\omega/dt$
ξ	Number of DPSK data symbols/frequency hop
$\Pi(t)$	Unity Amplitude Rectangular gating function

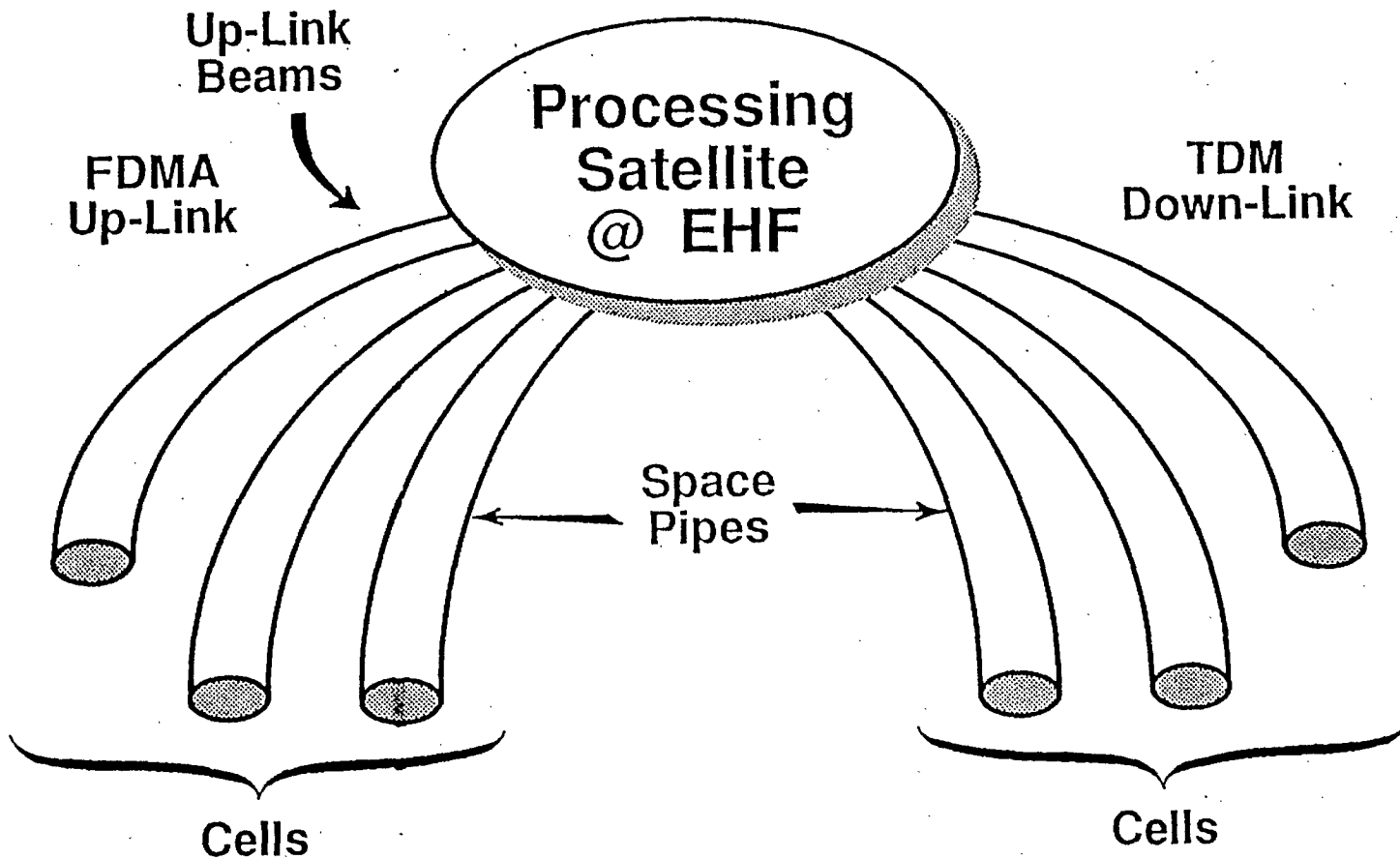
ρ_k	SNR on the k^{th} baud interval
$\sigma(t, z)$	Time-space dependent charge density
λ_k	SNR reduction on the k^{th} baud interval
ϕ_k	DPSK phase over k^{th} symbol interval
ψ_k	$\left[\theta(t+T) - \theta(t) \right] \text{mod}(2\pi)$
ω	Radian frequency

Chapter 1

1.1 Introduction

This study presents the background for and analysis of a proposed group demodulator for use in the Canadian EHF Satellite Communications (SatCom) system. This system makes use of signal processing functions on-board the satellite and requires an on-board demodulator with the capability of simultaneously processing a number of frequency division multiple access (FDMA) signals on multiple uplink beams. The demodulator also converts these signals to a time division multiplexed (TDM) format after which other signal processing functions, described subsequently, can be performed. The satellite then re-transmits the signals in TDM format on one or more possible downlink beams. These concepts are illustrated by Figure 1.1. In this Figure the "pipe" like structures represent up-links to and down-links from the processing satellite receiver. Each pipe represents an antenna beam and each beam is composed of several users, separated via FDMA on the uplink and TDM on the down-link. This thesis will concentrate on the demodulation of FDMA uplink signals.

The system supports two classes of digital communications users; a low data rate (LDR) user group which uses frequency shift keying (FSK) with bit rates up to 64



The EHF SatCom Concept

Figure 1.1

Kbps, and a medium data rate (MDR) group which uses differential phase shift keying (DPSK) with bit rates near the T1 (1.54 Mbps) range.

Group demodulation refers to the capability of a single demodulator structure to simultaneously convert a number of user signals from specified carrier frequencies to baseband. Typically, all users in the "group" have the same modulated signal structure. The receiver under study here, however, is capable of group demodulation of both FSK and DPSK users without channelizing these users into two independent structures.

Conventional communications satellites have traditionally been simple R.F. repeater stations which demultiplex received signals, amplify and then retransmit them. Continued advances in signal processing techniques and technology, however, have led to the development of more sophisticated signal processing functions on-board the satellite. On-board signal processing, as it is envisioned for the EHF SatCom system, can provide a number of advantages over the conventional transponder approach. Some of these include signal spreading/despreading, baseband signal regeneration and signal routing to either different transmitting beams (beam hopping) or intersatellite crosslinks. Although the cost of this extra processing is usually measured as additional spacecraft weight and power consumption, these costs can be offset by the increased

communications efficiency which allows for lower power operation and small antennas.

Signal despreading is required where spread-spectrum techniques have been used at the transmitter to help secure the communications link against intentional jamming. Most spread-spectrum systems use either frequency hopping (FH) or direct sequence/pseudo noise (DS or PN) techniques. In the FH case the carrier frequency is switched at discrete time intervals over a wide bandwidth; in DS techniques the data is multiplied by a pseudo-random spreading function. Both methods require a synchronized despreading facility on-board the satellite to demultiplex the message signals. In addition, as demodulation and remodulation are performed on the satellite, the two-link satellite transmission path is reduced to two single-link paths in tandem. This regeneration of the baseband signal also allows for a number of coding (or interleaving) and routing functions to be performed. On-board routing of data can be accomplished by using a TDMA formatted baseband output data stream. This facility also provides packet switching and beam hopping capabilities. In this case any routing information is assumed to be contained as a header in the regular data stream.

A system incorporating these features requires a demodulator capable of processing multiple users. Previous studies [1], [2] have examined the use of separate

The demodulator proposed by Felstead [3], which will be presented subsequently, is based on a surface acoustic wave (SAW) device implementation of a real time Fast Fourier transform (FFT) technique. In this study a digital Fourier transform (DFT) is used to approximate the performance of the SAW-based FFT processor. The distinct advantage of Felstead's system is that PSK symbols are demodulated on a hop basis, where each hop is several symbols in duration. This yields a significant synchronization advantage as, otherwise, a T1-rate symbol synchronization must be maintained between the satellite and the earth-based terminal.

Although Felstead's technique allows for the joint demodulation of FSK and DPSK users, our analysis will concentrate on the latter. The performance analysis for FH-FSK users has been given in work performed by Ma [7]. The goals of this report are twofold:

(i) a performance analysis of the receiver proposed by Felstead for the medium data rate (DPSK) users will be presented,

(ii) a communications theory for SAW based demodulators for use in digital communications will be given.

1.2 Satellite System Model

The assumed satellite system model is illustrated in Figure 1.2. The front end of the structure translates the FH spread spectrum signals into the IF frequency bandwidth of the demodulator. The group demodulator then has as input all the FSK and DPSK signals over a constant IF bandwidth where coherence of each signal is maintained over periods corresponding to the duration of the spreading (frequency) hop. For the FSK case, the demodulator estimates which tones have been sent; in the DPSK case, it converts the signals to a common secondary IF frequency where standard differential detection is performed. In both cases the SAW-based processor converts the input FDMA signals to a TDM format. Thus it functions as a transmultiplexer, allowing the power-limited down-link to be operated in a beam switched TDM mode. It is assumed that any routing, down-link coding, or interleaving functions are performed in the baseband signal processor. The final stage of the on-board processing is the retransmission of the data on an appropriate down-link carrier and down-link beam; this is performed by the satellite transmitter of the system shown.

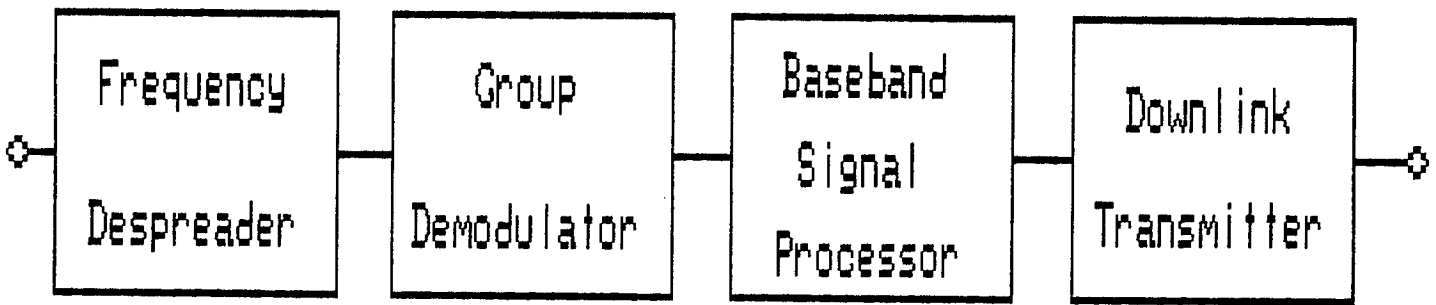


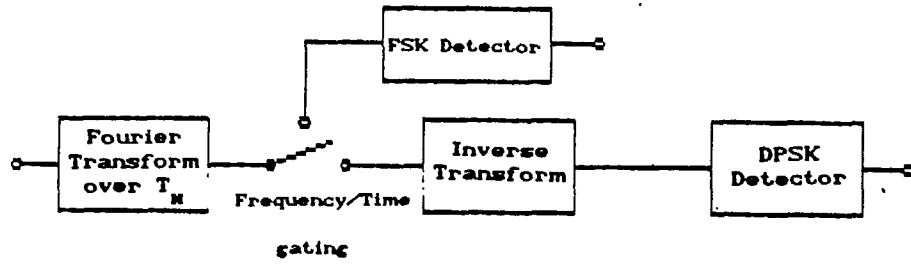
Figure 1.2 satellite system Model

1.3 Literature Review

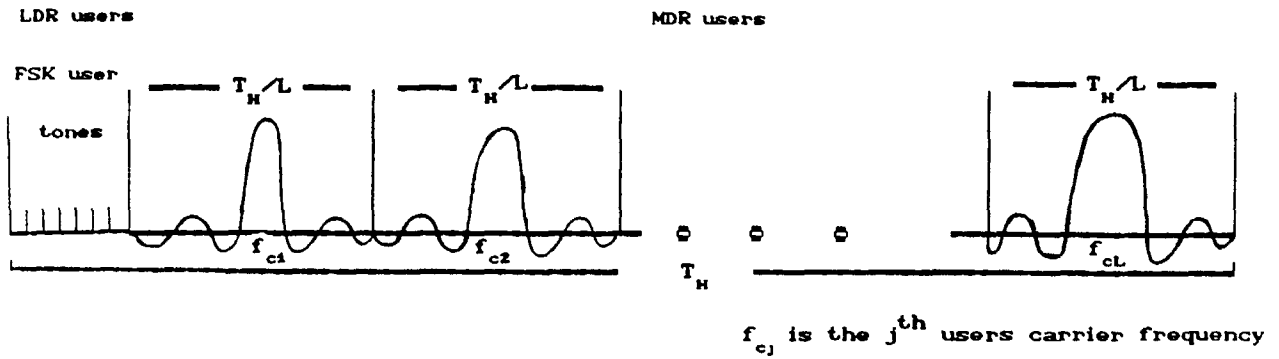
The concept of performing joint group demodulation on blocks of DPSK and FSK symbols was originally proposed by Felstead in [3]. The basis of this technique is the ability to perform a Fourier transform over the input bandwidth of L DPSK and N FSK users, with an observation interval corresponding to the (spread-spectrum) frequency hop period, T_H . The fundamentals of this technique are illustrated by the demodulator shown in Figure 1.3a. Over the period T_H , ξ DPSK symbols are received from each MDR user and a single tone is received from each LDR user. The result of performing this transformation is the Fourier domain representation of ξ DPSK symbols, centered about each of the L MDR user carrier frequencies and a series of N impulses, corresponding to the N FSK tones. Since the Fourier transform processor is implemented with SAW devices in this proposal, this frequency output is given as a time domain representation. Thus the frequency separation of the spectrums corresponds to a delayed output separation in time. This is illustrated by 1.3b. This output is then time-gated. The FSK tones are detected via an envelope detector, and the MDR user spectrums are inverse transformed about each of the L carrier frequencies to produce a time

Figure 1.3 Felsteads Proposed Demodulator

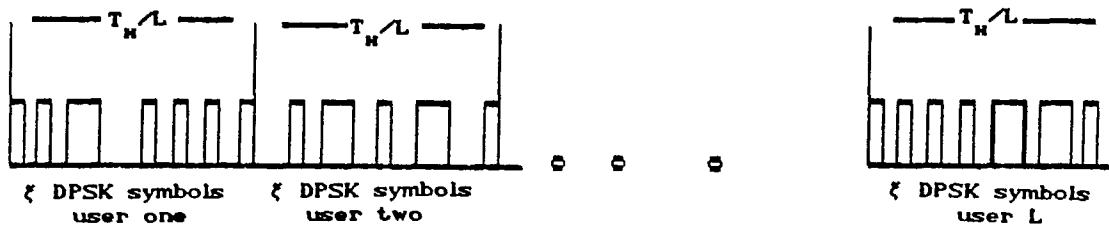
(a) Demodulator Structure



(b) Fourier Domain Output



(c) MDR output after the Inverse Fourier Transform



multiplexed signal as is illustrated (in baseband) in Figure 1.3c.

Notice that symbol level timing for the DPSK users can be obtained on-board the satellite using standard techniques and timing for the transforms can be extracted from the frequency de hopping clock, thus providing the synchronization advantage mentioned earlier.

Many studies have been devoted to the effects of FSK demodulation with FH systems [4], [5], [6]. Ma [7] studied the effects of windowing on such a system and concludes that windowing is a necessity for FH-FSK systems. Some work has been done on windowing of PSK data [2], but this is normally performed over a period corresponding to the symbol duration and does not have direct application to this study.

SAW based demodulators for either PSK or FSK data have been considered in some studies [1],[8]. For the most part those designed for FSK demodulation have performed satisfactorily [8], [9], [10], but attempts to use similar techniques for medium data rate PSK users have encountered excessively strict timing requirements and have not performed well.

Grant et al [10] and Otto [11] present detailed descriptions of SAW implementations for the chirp Fourier transform (CFT), which is the algorithm used to achieve the SAW-based FFT. In particular [10] provides experimental proof of the validity of the SAW CFT processor.

The two most common SAW devices are the reflective array compressor (RAC) and interdigital transducer (IDT). Of these two, the IDT is the simplest to analyse and produce. Its theory of operation has been presented by various authors [12], [13], [14] with varying degrees of complexity. The simpler models provide a good understanding of SAW operation without significant computation. The more complex models presented in these references require significant computation but yield correspondingly better results. Since the presentation of SAW devices given in Appendix A is meant to be tutorial in nature, the simpler models are presented.

Analysis of the DPSK users has been performed using quasi-analytical techniques outlined in [21]. These techniques include a noiseless simulation of the demodulator with averaging over an assumed probability density function (pdf). The noise distribution is assumed to be Gaussian, resulting in the pdf determined by Pawula, Rice, and Roberts in [15] and applied by Pawula in [16] and [17].

1.4 Presentation Outline

Chapter One has provided the general background for this study in the context of the EHF satellite communications system. The specific implementation for the demodulator and signal structure used are outlined in Chapter Two. The third Chapter provides an analytical treatment of a SAW implementation of the proposed demodulator. The fourth Chapter provides the mathematics necessary to perform bit error rate analysis using the quasi-analytical method. Chapter five provides results from application of these techniques to studies of different system parameters. These system parameters include optimum windowing for the DPSK users, the effects of varying DPSK user (channel) bandwidth, and an investigation of varying time-bandwidth (TB) products in the SAW devices used in this implementation. In addition, the effects on performance of amplitude and phase ripple in typical SAW devices is given. Conclusions and suggestions for future study appear in Chapter six. For completeness, Appendix A is included to provide some physical background and modelling techniques for SAW IDTs. It also presents some implementation considerations of particular interest for the applications studied here.

1.5 Contributions

In [3], the initial proposal, effects such as windowing of the transform and gating the spectrum about each user were not considered. As is subsequently shown these processes can have a significant effect on the performance of the demodulator and so are included in the analysis. Bandwidth allocations and the effect of interfering users, as well as processor time-bandwidth product and SAW device amplitude and phase ripple are also taken into consideration in this analysis. A communications theory of SAW devices used to perform the Fourier transforms is presented and some physical limitations of these devices are related to the performance of Felstead's demodulator for DPSK. Appendix A provides a physical description of IDT SAW devices and presents some simple models. The author felt it helpful to develop some background in this area, but this appendix is not mandatory to understanding the thesis. It is presented here for the interested reader.

Chapter 2

2.1 Signalling Format and Group Demodulation

The received uplink signal from a single beam will consist of N users of M -ary FSK at what is termed a low data rate (LDR) and L users of DPSK at a medium data rate (MDR). Each FSK user transmits a single tone per hop interval. Assuming one tone per symbol (fast hopping), this corresponds to a maximum data rate of $\log_2(M)/T_H$ bps. The DPSK users transmit a data frame of ξ symbols per hop, where $\xi = 1.54 \times 10^6 T_H$ for binary signalling and $\xi = 0.77 \times 10^6 T_H$ in the quaternary case; since this implies more than one symbol is received per hop, the DPSK demodulator is a slow hopping system. The resulting medium data rate is assumed to be comparable to a T1 rate, i.e. 1.54 Mbps. DPSK users are separated from each other and from the LDR users via FDMA. Incorporated into the uplink transmission is a FH spread spectrum system with hop length T_H . Figure 2.1 illustrates a possible signalling pattern with such a configuration. In this illustration the discrete lines represent possible FSK tones (a consecutive FSK frequency assignment is assumed). The blocks used in the MDR user expansion represent that segment of the IF bandwidth allocated to each DPSK user.

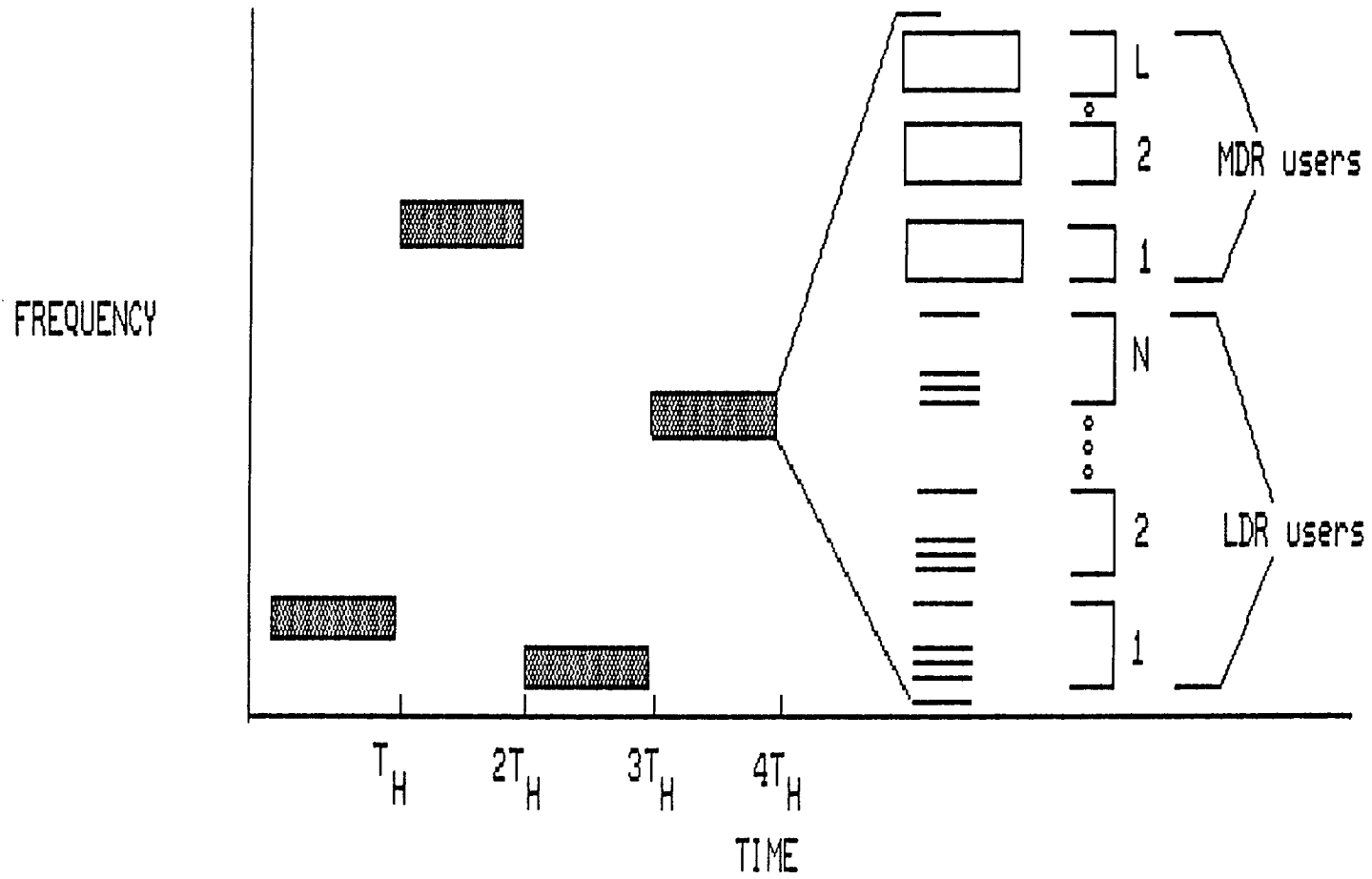


Figure 2.1 Uplink Signalling Pattern for
N FSK and L DPSK users

Demodulation is performed by mapping the composite signal onto a TDMA data stream using Felstead's Fourier transform (FT) technique as illustrated in Figure 2.2. This illustration is simply a re-representation of Figure 1.3a, but two switches are used in place of one to help simplify the subsequent presentation. As this Figure indicates, a Fourier transform is performed over the time duration of the hop interval, T_H . As a result of this SAW-based transform, the frequency domain output is mapped onto a time domain axis. The bandwidth analysed in this transformation is termed the IF bandwidth and denoted as B_{IF} . On output from the FT processor, the lower frequency portions of B_{IF} will contain pulses corresponding to the Fourier domain representation of each of the N FSK tones sent; this segment of B_{IF} is termed B_{fsk} . The remaining portion of the IF bandwidth will contain the Fourier domain representation of ξ DPSK symbols for each of the L DPSK users, centred around each MDR user's carrier frequency. This portion of B_{IF} is termed the DPSK bandwidth, denoted as B_{dpsk} .

In the DPSK portion of the demodulator, an inverse Fourier transform (IFT) is performed L times per hop over the bandwidth allocated to each DPSK user, denoted as Δf_u . This process converts the frequency domain representation of the signals back into a time domain format where standard differential detection can be performed.

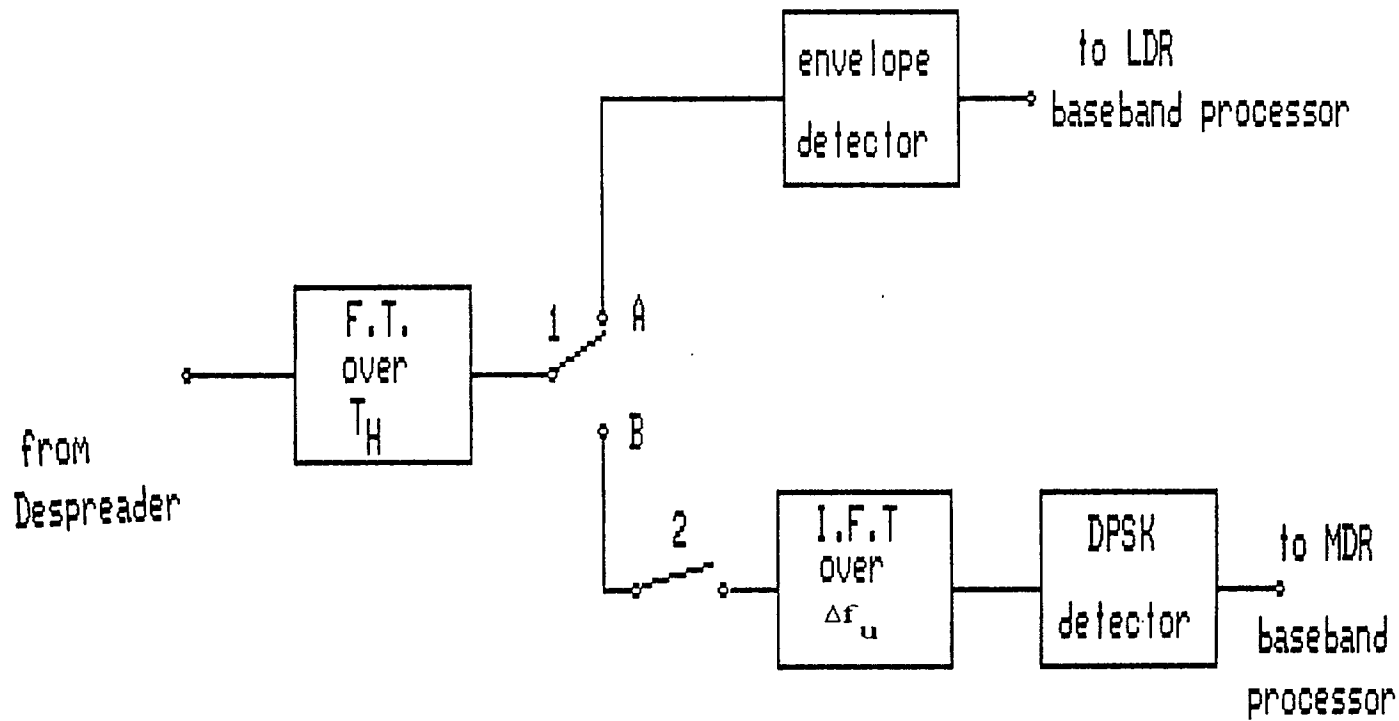


Figure 2.2 Fourier Transform Based
Joint Group Demodulation Technique

The FT processor maps the frequency domain output onto a linear time scale according to the relation

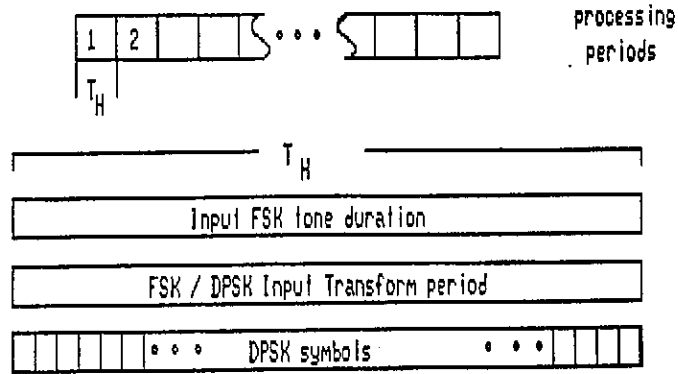
$$f = \mu t \quad (2.1)$$

where μ is a physical parameter of the processor known as the dispersive slope and t is the time delay of the output, measured using the hop duration as a reference. Using this relationship, timing and bandwidth equivalences are determined and illustrated in Figure 2.3. The signalling layout is decomposed into time segments in Figure 2.3a and a possible bandwidth allocation is shown in Figure 2.3b. This diagram also illustrates the relationship between B_{IF} , B_{fsk} , B_{dpsk} , and Δf_u . An equivalent time for mapping for the FT output in Figure 2.3b is shown in Figure 2.3c. Note that after the FT has been performed, the FSK and DPSK users are time separated. This implies that switch 1 in Figure 2.2 moves from position A to B at time $t = \eta T_H$ of each hop interval, where, $\eta = B_{fsk}/B_{IF}$.

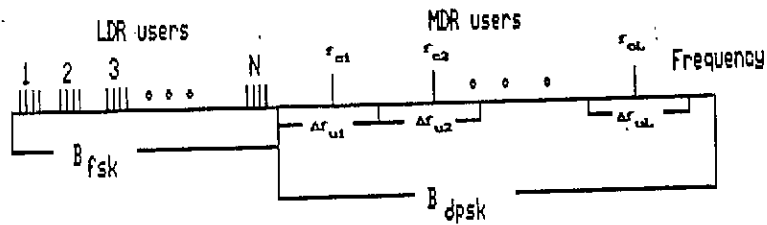
On input to the demodulator, it is assumed that the received signal has been despread so the input signal, $f(t)$, is given by

$$f(t) = \sum_{i=1}^N S_i(t) + \sum_{j=1}^L D_j(t) \quad (2.2)$$

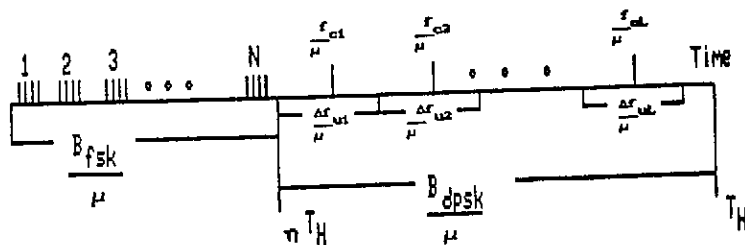
Figure 2.3 Signal Timing and Bandwidth Allocations



a: FT processor timing



b: a possible frequency allocation



c: corresponding time mapping

where $S_i(t)$ represents the i^{th} FSK user's tone for this hop interval and $D_j(t)$ is the j^{th} DPSK users sequence over the same hop interval. FSK demodulation is performed over the initial ηT_H of each hop and is described more thoroughly in the following section. The remaining portion of the signal, representing the DPSK users, is demodulated via a time/gating inverse FT process discussed in section 2.3 .

2.2 FSK Demodulation

After translation of the LDR signal to the IF band by the despreader and disregarding timing offsets, the LDR user input to the FT processor can be written as

$$S_i(t) = A_i \cos [2\pi(f_i + \delta f_i)t + \theta_i(t) + \theta_i] + n(t) \quad (2.3)$$

where

A_i is the signal magnitude

f_i is the signal frequency

δf_i is a frequency offset

$\theta_i(t)$ is phase jitter

θ_i is a random phase offset

and

$n(t)$ is white gaussian noise.

Other authors have investigated the effects of phase jitter, [18], [19] and frequency offsets [7]. Among the conclusions reached is that windowing is necessary in a practical system where power imbalances and frequency offsets are likely to occur. From [7], the optimum window is a function of the level of interference and noise, but for this study it is sufficient to note that the optimum window can be incorporated into the FT processor.

The output of the FT processor to the input FSK data is then given by

$$\text{FT} \left\{ \sum_{i=1}^N S_i(t) \right\} = \sum_{i=1}^N A_i \delta(f - (f_i + \delta f_i)) * W(f) \quad (2.4)$$

where $W(f)$ is the Fourier transform of the windowing function used, $\delta(f)$ is a delta function in the Fourier domain, and $*$ denotes convolution. This output can be amplitude detected to determine the time/frequency position of the pulse, corresponding to the particular symbol sent.

If the FSK frequency resolution of the processor is denoted by ϵf , the minimum required bandwidth for the M-ary FSK users is $NM\epsilon f$. If guard bands are used between sets of consecutive frequency assignments and at the edges of the available bandwidth, $B_{\text{fsk}} = [MN+N+1]\epsilon f$. In either case, each frequency bin corresponds to a pulse separation in time of $\Delta t = \epsilon f / \mu$. An example of the output time mapping for quaternary FSK, with N users separated by guard bands is shown below in Figure 2.4. Using this time mapping, it is possible to determine which symbol was sent by detecting which of the frequency bins reserved for each user contains the largest amplitude pulse (maximum likelihood detection). Timing information for this process can be extracted from the despreader, which is synchronized to the hop interval.

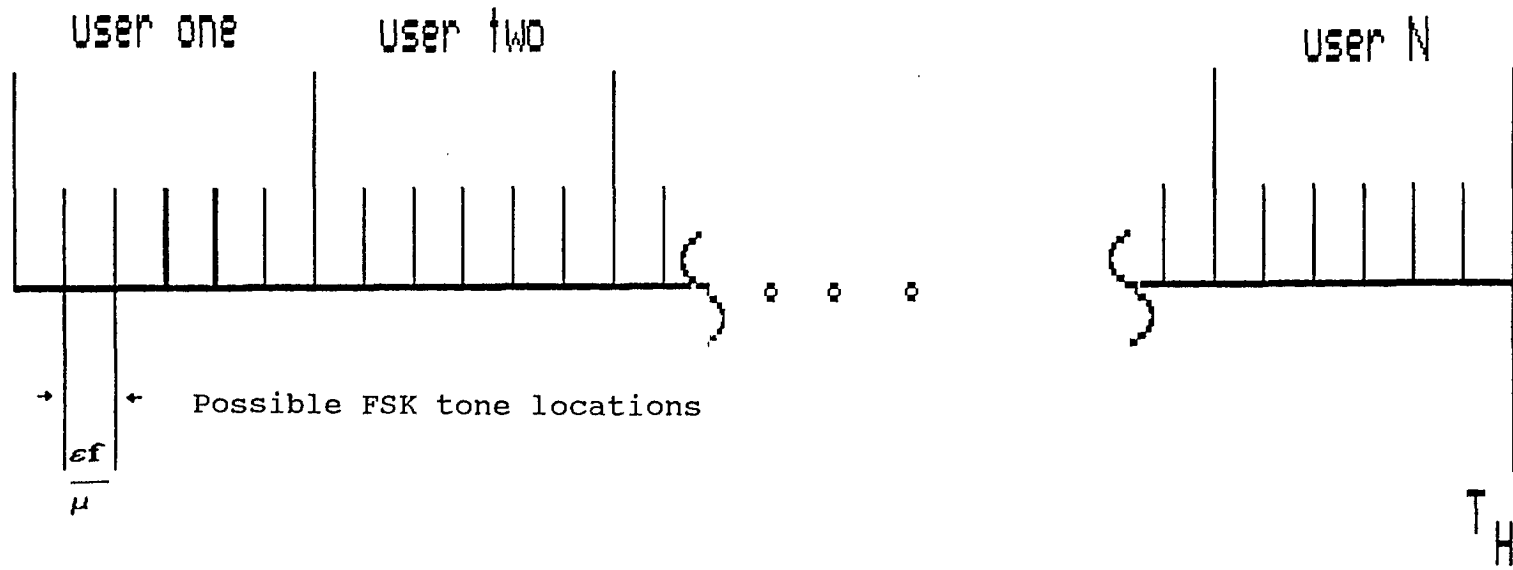


Figure 2.4 LDR Demodulator Time Mapping
For Quaternary FSK

Detailed analysis of FH-FSK demodulators based on similar techniques have been presented elsewhere [1], [3], [10]. Since the primary interest of this study is the group demodulation of DPSK data, demodulation of the LDR users will not be considered in any greater detail.

2.3 DPSK DEMODULATION

On output from the despreader, the DPSK signal $D_j(t)$ can be written in the form

$$D_j(t) = \text{Re}\left\{u_j(t)e^{j(2\pi(f_{c_j} + \delta f)t + \theta_j(t) + \theta_j)}\right\} + n(t) \quad (2.5)$$

where

f_{c_j} is the carrier frequency of user j

δf is a frequency offset due to imperfect despreading

$\theta_j(t)$ is phase jitter over the ξ symbols

θ_j is a phase offset on the carrier, constant over the duration of the hop.

and

$n(t)$ is assumed to be additive white gaussian noise.

The term $u_j(t)$ is the baseband representation of ξ DPSK data symbols, expressed as

$$u_j(t) = \sum_{k=1}^{\xi} e^{j\phi_k} g(t-n\tau). \quad (2.6)$$

In equation 2.6 $g(t)$ is the pulse shape of the DPSK symbol, assumed here to be

$$g(t) = \begin{cases} 1 & 0 \leq t \leq \tau \\ 0 & \text{otherwise.} \end{cases} \quad (2.7)$$

τ is the symbol duration, so for binary DPSK $\tau = T$ and ϕ_k can take on the values 0 or π . In this study the bit rate is fixed at 1.6 Mbps so for the quaternary DPSK case, $\tau = 2T$ and ϕ_k can take on the values 0, $\pi/2$, π , or $-\pi/2$. As in the FSK case, a Fourier transform is performed over the hop duration T_H . In this case, however, the output of the FT processor will be the Fourier domain representation of ξ DPSK symbols, centred on each user's (IF translated) carrier frequency. Discounting the effects of phase jitter and in the absence of noise, the output of the FT processor can be expressed as

$$\sum_{j=1}^L U_j(f) \delta \left(f - (f_{cj} + \delta f) \right) \quad (2.8)$$

where $U_j(f)$ represents FT $\left\{ u_j(t) \right\}$, the Fourier transform

of the baseband signal.

Using equation 2.6, the FT of $u_j(t)$ is given by

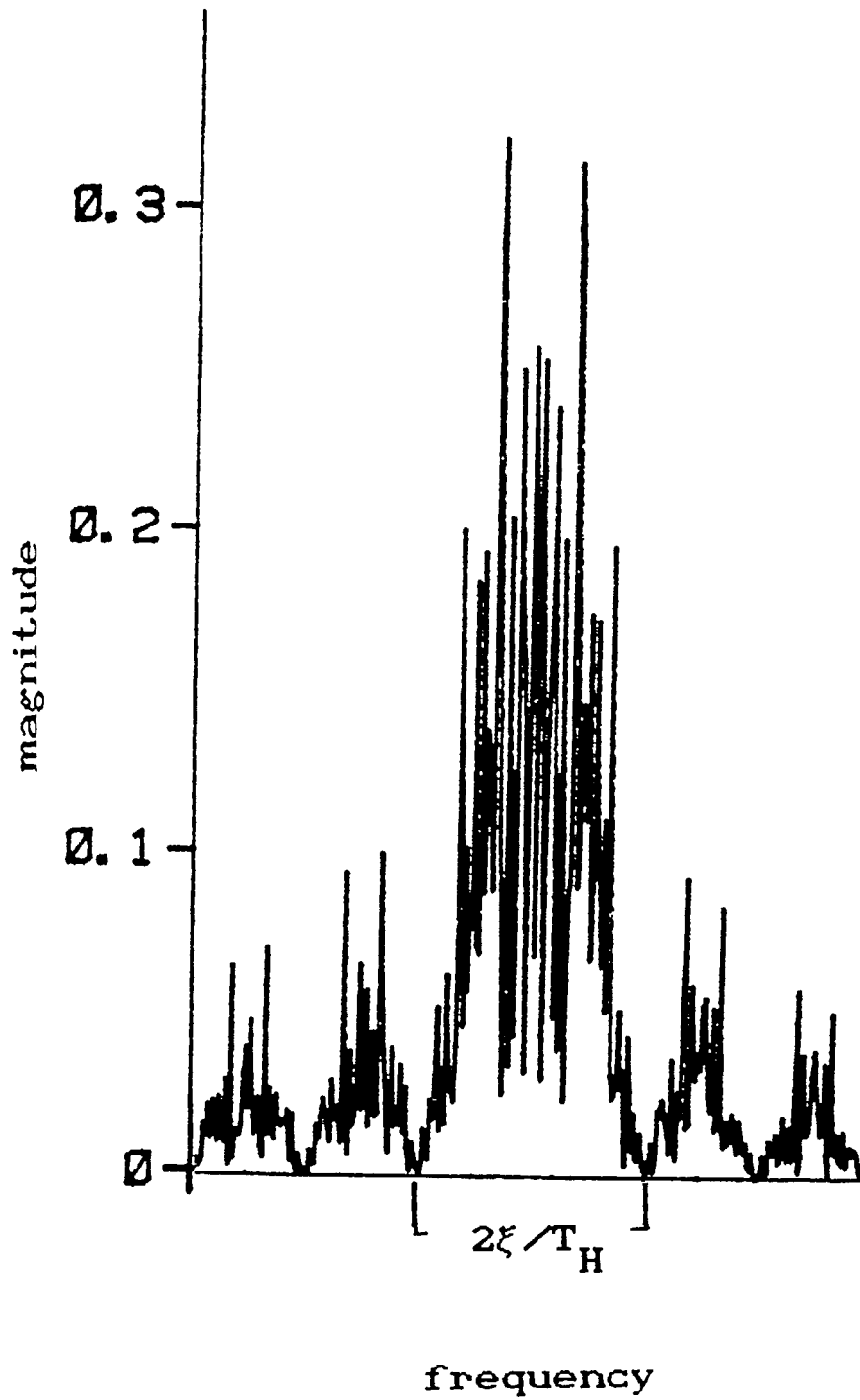
$$\sum_{k=1}^{\xi} e^{j\phi_k} \text{FT} \left\{ g(t-k\tau) \right\} = \sum_{k=1}^{\xi} e^{j(\phi_k - 2\pi f\tau)} \text{FT} \left\{ g(t) \right\} \quad (2.9)$$

An example of $\text{FT} \left\{ u_j(t) \right\}$ is shown below in Figure 2.5 for $\xi=50$.

The result shown in Figure 2.5 was obtained by using a 2048 point DFT with an observation interval corresponding to 50 μsec . Note that the envelope shape of $U_j(f)$ corresponds to the sinc function produced by $\text{FT}\{g(t)\}$. In this case the main lobe has a width corresponding to twice the symbol rate. This is directly analogous to the characteristic of a PN spread spectrum signal, where the main lobe width is twice the chip rate.

The equivalent time domain mapping of the output, as described by equation 2.1, results in each user's spectrum is centered at $t = \frac{f_{cj}}{\mu}$, where f_{cj} is the carrier frequency of user j and it is assumed that no frequency offsets have occurred. If the frequency separation between users is assumed equivalent to the user bandwidth, Δf_u , then each truncated spectrum occupies a time interval of $\Delta t = \Delta f_u / \mu$. By momentarily opening switch 2 (in Figure 2.2) every Δt

Figure 2.5 Fourier Transform of $u_j(t)$
with $\xi = 50$ and using rectangular windowing

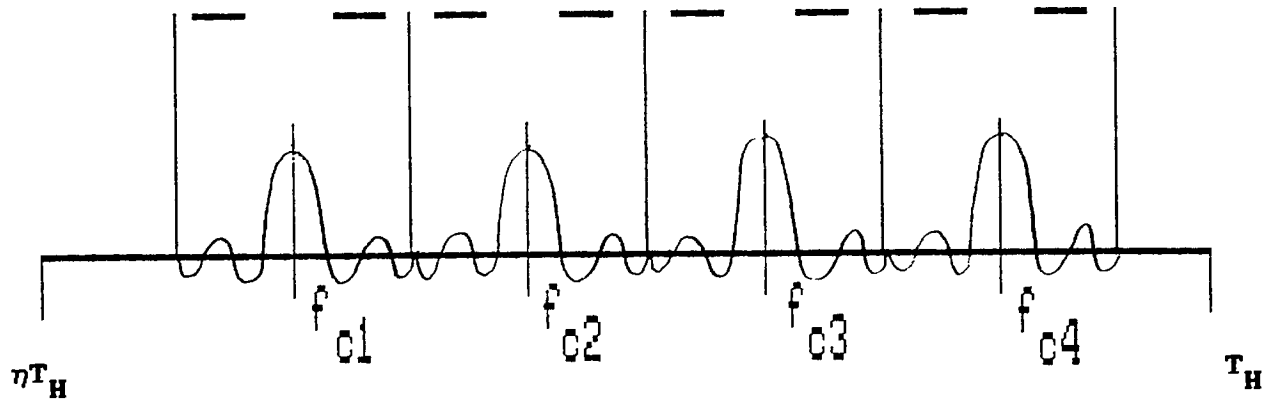



seconds, the output spectrum is time gated about each center frequency. An example of this is illustrated in Figure 2.6 for the case where four MDR users are considered and truncation of each spectrum is performed over the range

$$\frac{f_{cj}}{\mu} - \frac{\Delta f_u}{2\mu} \leq t \leq \frac{f_{cj}}{\mu} + \frac{\Delta f_u}{2\mu} . \quad (2.10)$$

By performing an inverse Fourier transform (IFT) independently over each truncated spectrum, the frequency domain representation of $u_j(t)$ is converted back into a time domain approximation of the original, denoted as $\hat{u}_j(t)$, and the input FDMA signals have been converted into a time-compressed TDMA data stream at a common carrier IF_2 . The value of IF_2 is a function of the device parameters used to realize this processor, as will be indicated in the following Chapter. If a frequency offset due to dehoppping is present and constant over the hop interval, the IFT processor output appears shifted to $IF_2 + \delta f$.

The time compression is a result of truncating the bandwidth of each user from B_{IF} to Δf_u . The amount of this compression depends on the DPSK user bandwidth and the first IF bandwidth, B_{IF} according to



where  represents a transform as in figure 2.5

The bandwidth allocated to each user is denoted as Δf_u
 f_{c_j} is the j^{th} users carrier frequency

Figure 2.6 Spectrum Truncation for DSPK Demodulation

$$\text{Time compression ratio} = \frac{\Delta f_u}{\mu T_H} = \frac{\Delta f_u}{B_{IF}} \quad (2.14)$$

where

$$\mu = \frac{B_{IF}}{T_H} \quad (\text{by design}) \text{ has been used.} \quad (2.14b)$$

So the downlink symbol rate will be $\Delta f_u / \mu T_H$ times greater than the uplink symbol rate for any given DPSK user.

Because the IFT processor output appears serially (in TDMA format) and at a common intermediate frequency, a single DPSK detector can be used for all MDR users in this group (on this beam). This implies that symbol timing for the DPSK detector can also be accomplished using standard techniques. Felstead's method of group DPSK demodulation has less severe transform timing requirements than the DPSK transform method proposed in [1]. In that technique the Fourier transform is performed over each DPSK symbol period, so ξ transforms are required for each hop interval, requiring timing information ξ times more accurate for the FT processor. In initial tests of such a system these timing requirements and the effects of narrowly truncating each transform led to significant performance degradation [1]. Using Felstead's technique, only one FT and L IFT operations are required per hop. Additionally, timing cycles for these operations can be derived with good accuracy from the system despreading clock, which is already synchronized to the

frequency hopping rate.

As will be shown later, a disadvantage of this technique is that high accuracy, very large time-bandwidth (TB) products are required for the SAW devices used in this implementation. The effects of varying TB product on the performance and capacity of this demodulator is investigated more thoroughly in Chapter 5.

Before proceeding with a detailed BER analysis of Felstead's demodulator, the FT and IFT processors will be described in greater detail. These processors use a SAW-based technique to perform a chirp Fourier Transform (CFT). The CFT algorithm, and possible SAW implementations of it, are discussed in Chapter 3.

Chapter 3 SAW based Fourier Transform Processors

3.1 The Chirp Fourier Transform

The chirp Fourier transform (CFT) is an algorithm which yields a continuous Fourier transform through the use of linearly frequency modulated (chirped) waveforms. It does not involve the processing of samples and should not be confused with the chirped z transform (CZT).

The CFT algorithm can be derived from the Fourier Transform relationship

$$F(\Omega) = \int_{-\infty}^{\infty} f(t) e^{-j2\pi\Omega t} dt = \int_{-\infty}^{\infty} f(t) e^{j\pi(-2\Omega t)} dt \quad (3.1)$$

by making the substitution

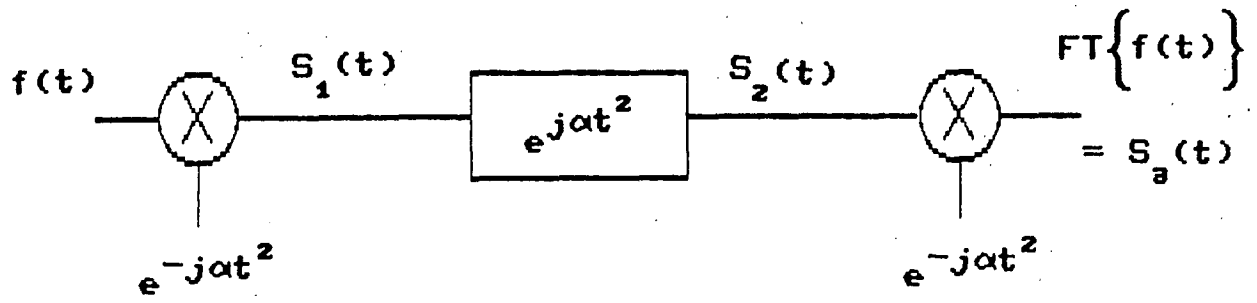
$$-2\Omega t = (\Omega - t)^2 - \Omega^2 - t^2. \quad (3.2)$$

Then (3.1) becomes the chirp Fourier transform, defined as

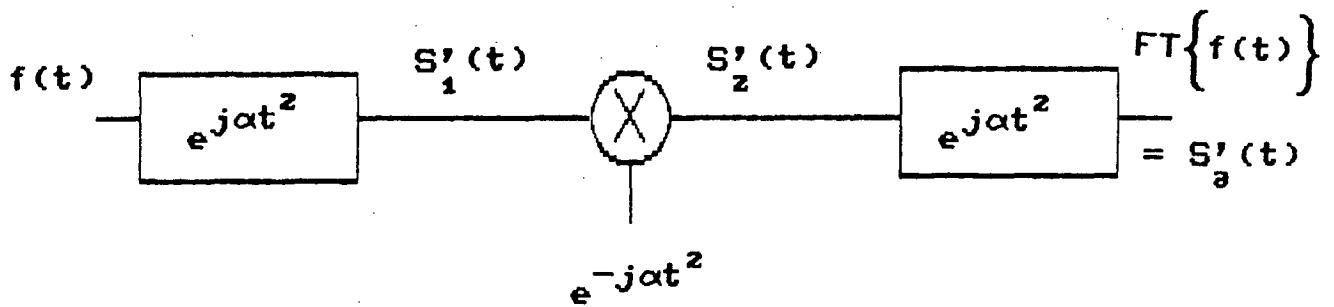
$$F(\Omega) = \left[\int_{-\infty}^{\infty} f(t) e^{-j\pi t^2} e^{j\pi(\Omega-t)^2} dt \right] e^{-j\pi\Omega^2}. \quad (3.3)$$

The term in square brackets suggests a premultiplication of the input function $f(t)$ by $e^{-j\alpha t^2}$ followed by convolution with a filter having an impulse response $e^{j\alpha t^2}$. The remaining term can be interpreted as a post multiplication by $e^{-j\alpha t^2}$. Equation (3.3), then, yields the structure shown in Figure 3.1a below, which is termed the multiply-convolve-multiply (M-C-M) arrangement of the CFT. Because of the dualized nature of multiplication and convolution in the time and frequency domains, an equivalent arrangement can be derived by interchanging the operations of convolution and multiplication. The result shown in Figure 3.1b is taken from Otto [11] and known as the convolve-multiply-convolve (C-M-C) arrangement. Although both arrangements yield the same CFT results, implementation considerations will tend to favour one over the other, depending on the application, as will be discussed subsequently. Because only one convolution is required in the M-C-M algorithm, an analysis will be performed for this technique and analogous conditions will be drawn for the C-M-C approach by evoking the time-frequency duality of these arrangements. This presentation follows closely the work performed by Grant in [10].

Figure 3.1 The M-C-M and C-M-C configurations



3.1a: The M-C-M configuration



3.1b: The C-M-C configuration

3.2 The M-C-M Chirp Fourier Transform Arrangement

The waveforms used for multiplication are generated by impulsing physically realizable SAW chirp filters; the convolution filter is also a SAW chirp filter. Impulsing each of these devices produces a linearly frequency modulated (chirp) waveform; positive chirps sweep from low to high frequency, negatively sloped chirps sweep from high to low frequency. Using the notation in the M-C-M configuration of Figure 3.1a and following the presentation given by Grant [10] , the impulse responses used are assumed to have the following form:

Premultiplication Chirp

$$C_1(t) = \Pi\left(\frac{t - t_1}{T_1}\right) W_1(t) \cos\left\{ \omega_1 t - \frac{1}{2} \mu t^2 + \varphi_1 \right\} \quad (3.4a)$$

Convolution Filter

$$H_0(t) = \Pi\left(\frac{t - t_0}{T_0}\right) W_0(t) \cos\left\{ \omega_0 t + \frac{1}{2} \mu t^2 + \varphi_0 \right\} \quad (3.4b)$$

Post Multiplication Chirp

$$C_2(t) = \Pi\left(\frac{t - t_2}{T_2}\right) W_2(t) \cos\left\{ \omega_2 t + \frac{1}{2} \mu t^2 + \varphi_2 \right\}. \quad (3.4c)$$

In these expressions,

- (i) $W_i(t)$ is an arbitrary amplitude weighting function (window).
- (ii) φ_i is an unassigned phase term.
- (iii) μ is the dispersive slope of the device, it represents the instantaneous angular frequency so that $d\omega/dt = \mu$.
- (iv) $\Pi\left(\frac{t - t_i}{T_i}\right)$ is a unit amplitude rectangular gating function of duration T_i centred at the time $t = t_i$.

For convenience, the first multiplication and convolution chirps will be denoted as

$$C_1^-(t) = \cos\left\{ \omega_1 t - \frac{1}{2} \mu t^2 + \varphi_1 \right\} \quad (3.5a)$$

$$H_0^+(t) = \cos\left\{ \omega_0 t + \frac{1}{2} \mu t^2 + \varphi_0 \right\} . \quad (3.5b)$$

Two methods of performing the M-C-M algorithm must be distinguished at this point. When the impulse response of the convolution filter is of longer time duration than that of the premultiplier chirp ($T_0 > T_1$) the arrangement is denoted as M(s)-C(l)-M where "s" is used to denote short chirp and "l" denotes a long duration chirp. In the alternative M-C-M arrangement, the premultiplier impulse response has a longer time duration than the convolution chirp ($T_0 < T_1$), and is denoted M(l)-C(s)-M. For reasons which

will be noted later, the M(s)-C(1)-M arrangement is more applicable to the group demodulator under study and so it will be explicitly analysed.

After premultiplication of the input signal $f(t)$ by $C_1(t)$ and convolution with $H_0(t)$, the signal $S_2(t)$ is given by the convolution integral

$$S_2(t) = \int_{-\infty}^{\infty} f(\tau) \Pi\left(\frac{\tau - T_1/2}{T_1}\right) \Pi\left(\frac{(t-\tau) - T_0/2}{T_0}\right) C_1^-(\tau) H_0^+(t-\tau) d\tau \quad (3.6)$$

where $C_1^-(t)$ and $H_0^+(t)$ are the negative and positive sloped chirps of $C_1(t)$ and $H_0(t)$ respectively. It is assumed here that $W_1(t)$ and $W_0(t)$ are of unity value over the duration of their respective signals, and that the processing cycle takes its time origin from the impulse applied to the premultiplying chirp filter (where any delay between this impulse and the output $C_1(t)$ has been ignored).

Consider the effect of the two gating functions on the convolution integral (3.6) by examining the following convolution, and noting that $T_1 < T_0$ in this arrangement. Define the convolution of the two gating functions in (3.6) as $SC(t)$, where

$$SC(t) = \int_{-\infty}^{\infty} \Pi\left(\frac{\tau - T_1/2}{T_1}\right) \Pi\left(\frac{(t-\tau) - T_0/2}{T_0}\right) d\tau \quad (3.7)$$

The output of such a convolution is zero for $t \leq 0$, increases linearly to a maximum at $t = T_1$. It remains at this value until $t = T_0$, after which it decreases linearly to zero at $t = T_0 + T_1$. This is illustrated in Figure 3.2.

This convolution result has significant implications on the transform output. Those regions of $SC(t)$ which are not flat, i.e. $t < T_1$ and $t > T_0$, produce significant distortions in the valid Fourier transform output. Because of this, only the flat topped portion of $SC(t)$ over the range $T_0 < t < T_1$ is considered as the true Fourier transform output. This is incorporated into equation 3.6 as a time-gating, and thus $S_2(t)$ is redefined as

$$S_2(t) = \Pi\left(\frac{t-t'}{T'}\right) \int_{-\infty}^{\infty} \hat{f}(\tau) C_1^+(\tau) H_0^-(t-\tau) d\tau \quad (3.8a)$$

where

$$t' = \frac{1}{2} (T_0 + T_1) \quad (3.8b)$$

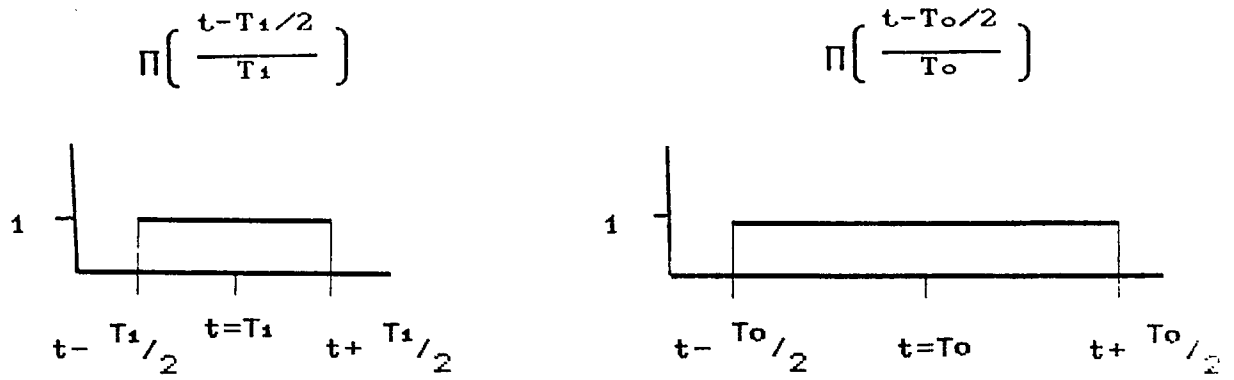
$$T' = T_0 - T_1 \quad (3.8c)$$

and

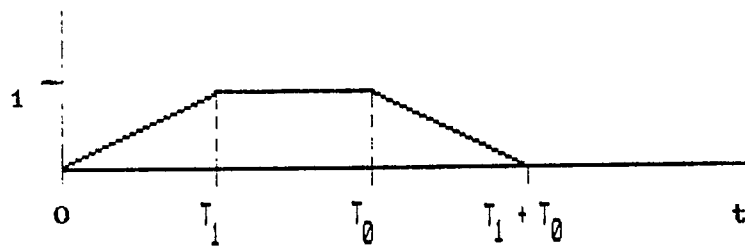
$$\hat{f}(t) = f(t) \Pi\left(\frac{t-T_1/2}{T_1}\right). \quad (3.8d)$$

In equation 3.8a, using the complex exponential expansion of the cosine terms and making the following substitutions:

Figure 3.2 Convolution of $\Pi\left(\frac{t-T_1/2}{T_1}\right)$ and $\Pi\left(\frac{t-T_0/2}{T_0}\right)$



SC(t)



$$\Theta_1 = \omega_1 \tau - \frac{1}{2} \mu \tau^2 + \varphi_1 \quad (3.9a)$$

and

$$\Theta_2 = \omega_0 (t-\tau) + \frac{1}{2} \mu (t-\tau)^2 + \varphi_0 \quad (3.9b)$$

results in

$$S_2(t) = \frac{1}{4} \Pi \left(\frac{t-t'}{T'} \right) \int_{-\infty}^{\infty} \hat{f}(\tau) \left(e^{j(\Theta_1 + \Theta_2)} + e^{-j(\Theta_1 + \Theta_2)} \right) d\tau \quad (3.10)$$

Note that those terms in equation 3.8 which are relatively quickly varying, that is terms centered at the sum frequency $(\omega_0 + \omega_1)$, will not make a significant contribution to the integral and have been neglected in the expansion of equation 3.10. Expanding the remaining terms in (3.10) yields

$$S_2(t) = \frac{1}{4} \Pi \left(\frac{t-t'}{T'} \right) \left\{ e^{j\Phi(t)} \int_{-\infty}^{\infty} \hat{f}(\tau) e^{-j\Omega\tau} d\tau + e^{-j\Phi(t)} \int_{-\infty}^{\infty} \hat{f}(\tau) e^{+j\Omega\tau} d\tau \right\} \quad (3.11a)$$

where

$$\Phi(t) = \omega_0 t + \frac{1}{2} \mu t^2 + \varphi_0 + \varphi_1 \quad (3.11b)$$

and

$$\Omega = \omega_0 - \omega_1 + \mu t \quad (3.11c)$$

Since $f(t)$ is real, $\hat{f}(t)$ is equivalent to its complex conjugate, $\hat{f}^*(t)$, and so (3.11a) can be written as

$$S_2(t) = \frac{1}{4} \Pi\left(\frac{t-t'}{T'}\right) \left\{ \int_{-\infty}^{\infty} X(\tau) e^{-j\Omega\tau} d\tau + \int_{-\infty}^{\infty} X^*(\tau) e^{j\Omega\tau} d\tau \right\} \quad (3.12a)$$

where

$$X(\tau) = \hat{f}(\tau) e^{j\Phi(\tau)} \quad (3.12b)$$

Noting that $\text{FT}\{f^*(t)\} = F^*(-f)$, equation 3.12a can be expressed as the sum of the Fourier transform of $X(t)$ and $X^*(t)$. Denoting $X(\Omega)$ as the FT of $X(t)$, (3.12a) becomes

$$S_2(t) = \frac{1}{4} \Pi\left(\frac{t-t'}{T'}\right) \left\{ X(\Omega) + X^*(\Omega) \right\} \quad (3.13)$$

$$= \frac{1}{2} \Pi\left(\frac{t-t'}{T'}\right) \text{Re} \left\{ \hat{F}(\Omega) e^{j\Phi(\Omega)} \right\} \quad (3.14)$$

$$= \frac{1}{2} \Pi\left(\frac{t-t'}{T'}\right) \left\{ \hat{F}_R(\Omega) \cos(\Phi(\Omega)) + \hat{F}_I(\Omega) \sin(\Phi(\Omega)) \right\} \quad (3.15)$$

$$= \frac{1}{2} \Pi\left(\frac{t-t'}{T'}\right) |\hat{F}(\Omega)| \cos\left[\Phi(\Omega) + \theta(\Omega)\right] \quad (3.16)$$

In equation 3.16, polar notation has been used to represent $\hat{F}(\Omega) = |\hat{F}(\Omega)| \angle \theta(\Omega)$ and $\hat{F}(\Omega) = \hat{F}_R(\Omega) + j\hat{F}_I(\Omega)$. As these expressions indicate, the amplitude spectrum of the input

signal exits as the envelope of $S_2(t)$ over the time interval $T_1 < t < T_0$. This time interval corresponds to the frequency range defined by 3.17 below

$$\omega_0 - \omega_1 + \mu T_1 \leq \Omega \leq \omega_0 - \omega_1 + \mu T_0 \quad (3.17)$$

Thus the bandwidth analysed is given by

$$B = B_{IF} = \frac{\mu(T_0 - T_1)}{2\pi} \quad (3.18)$$

with center frequency

$$f_{co} = \frac{(\omega_0 - \omega_1) + \frac{1}{2}\mu(T_0 + T_1)}{2\pi} \quad (3.19)$$

Post multiplication of (3.16) by $C_2(t)$ is performed to extract the phase information from $S_2(t)$, so the processor output is given by

$$S_3(t) = S_2(t) \Pi\left(\frac{t - t_2}{T_2}\right) W_2(t) \cos\left\{\omega_2 t + \frac{1}{2}\mu t^2 + \varphi_2\right\}. \quad (3.20)$$

where $W_2(t)$ is the amplitude window applied to the transform and for now will be left undefined. By setting $t_2 = t'$, $T_2 = T'$, and selecting the low frequency terms this expression becomes

$$s_3(t) = \frac{1}{4}\Pi\left(\frac{t-t'}{T'}\right) |\hat{F}(\Omega)| W_2(t) \cos\left\{(\omega_0 - \omega_2)t + \theta(\Omega) + \varphi_1 + \varphi_0 - \varphi_2\right\} \quad (3.21)$$

$$= \frac{1}{4}\Pi\left(\frac{t-t'}{T'}\right) W_2(t) \left\{ \hat{F}_R(\Omega) \cos\left[(\omega_0 - \omega_2)t + \varphi_0 + \varphi_1 - \varphi_2 \right] - \hat{F}_I(\Omega) \sin\left[(\omega_0 - \omega_2)t + \varphi_0 + \varphi_1 - \varphi_2 \right] \right\}. \quad (3.22)$$

From equation (3.22) it follows that the phase spectrum, $\theta(\Omega)$, is phase modulated on the carrier $\omega_{IF} = (\omega_0 - \omega_2)$. For the case where $\omega_1 = \omega_2$, the output is at baseband and a quadrature postmultiplication would be required to extract $\hat{F}_I(\Omega)$ (see [10], section 2.3).

A major disadvantage of this arrangement is a duty cycle of less than 100%. It is shown by Grant [10] that because only those portions of the output over the time interval $T_1 < t < T_0$ are considered as the valid FT, the maximum duty cycle for this arrangement is 50%. To achieve 100% duty cycle then, two parallel channels must be constructed. In an application, this effectively doubles the weight and power consumption requirements of the processor. An alternative is to implement either the M(1)-C(s) or the C-M-C arrangement.

In the M(1)-C(s) arrangement the duration of the premultiplier chirp is greater than the duration of the convolution impulse ($T_1 > T_0$). Although this allows 100% duty cycle operation, the resulting transform is taken over a gating function which is itself a function of time. Thus the observation interval over which the transform is computed at a given instant includes only a fraction of the input (time domain) signal. Because of this, phase information is not consistent across the transform of one input period, making the M(1)-C(s) implementation inappropriate for our application. It should be noted though, that this technique is applicable in demodulators of non-coherent FSK, where the spectral components are constant for the duration of the premultiplier chirp and lack of phase information does not degrade performance. In this case a second multiplier is not required since the spectral amplitude information already exists on a phase modulation after the convolution filter. This fact follows from equation (3.16) where it is clear that an amplitude detector will yield $|\hat{F}(\Omega)|$. The C-M-C arrangement offers the capability of 100% duty cycle operation without the loss of phase information. This implementation is now considered.

3.3 The C-M-C arrangement

In the C-M-C transform arrangement (Fig. 3.1b) the time gated input signal is convolved with a chirp filter, multiplied by a (long) chirp of equal but opposite dispersion, and then convolved with another chirp filter. The time domain analysis of this arrangement is significantly more complex than that of the M-C-M arrangements. However, as noted earlier, the C-M-C configuration is the time-frequency dual of the M-C-M configuration. This implies that, as indicated in [11], the impulse responses of the devices used in the C-M-C configuration are time-reversed replicas of those used in the M-C-M configuration. Alternatively, this means that the frequency direction of each chirp changes direction, for example up-chirps in one configuration become down chirps in the other. This is indicated by the sign of the exponential terms in Figures 3.1a and 3.1b. Furthermore, this duality implies that whatever applies to dispersion and bandwidth in one configuration applies to bandwidth and dispersion in the other. Table 3.1, from Grant [10], summarizes the significant equivalences of this dualism. Equations 3.23 through 3.25 list the impulse responses of the C-M-C configuration, which again are physically realizable real functions.

M-C-M

Maximum signal duration : T_1

Maximum signal bandwidth: $B_2 = B_0 - B_1$

For $B_s > B_0 - B_1$: truncation of transform output

For $T_s > T_1$: truncation of input signal

C-M-C

Maximum signal duration : $T_2 = T_0 - T_1$

Maximum signal bandwidth: B_1

For $B_s > B_1$: truncation of the output bandwidth

For $T_s > T_0 - T_1$: truncation of input signal

Table 3.1 Dualism of the M-C-M and C-M-C arrangements

The chirp waveforms for the C-M-C arrangement are:

$$C'_1(t) = \Pi\left(\frac{t - t'_1}{T'_1}\right) W'_1(t) \cos\left\{\omega_1 t + \frac{1}{2} \mu t^2 + \varphi_1\right\} \quad (3.23)$$

$$H'_0(t) = \Pi\left(\frac{t - t'_0}{T'_0}\right) W'_0(t) \cos\left\{\omega_0 t - \frac{1}{2} \mu t^2 + \varphi_0\right\} \quad (3.24)$$

$$C'_2(t) = \Pi\left(\frac{t - t'_2}{T'_2}\right) W'_2(t) \cos\left\{\omega_2 t + \frac{1}{2} \mu t^2 + \varphi_2\right\}. \quad (3.25)$$

The time-window for the input signal is $T'_2 = T'_0 - T'_1$ and the maximum input signal bandwidth is given by the bandwidth of the first convolution filter $C'_1(t)$. This implies that the bandwidth which can be analysed is given by

$$B_1 T_1 = \mu T_1'^2 \quad (3.26a)$$

where

$$\begin{aligned} B_1 &= \text{bandwidth of the first convolution filter} \\ &= \mu T_1'. \end{aligned} \quad (3.26b)$$

In the C-M-C arrangement the windowing function is implemented in the second convolution filter as $W'_2(t)$ so once again $W'_1(t) = W'_0(t) = 1$ over the duration of $C'_1(t)$ and $H'_0(t)$ respectively. Incorporating the weighting into the impulse response of the first SAW device would effectively reduce the resolvable bandwidth of the processor. Thus

implementing the weighting in the last (second convolution) filter is always a preferable approach. This has some advantages for the joint FSK/DPSK demodulator which was illustrated by Figure 2.2 of Chapter 2. It turns out that by implementing the window in this filter only one additional device is required to realize separate windowing functions for DPSK and FSK users.

The C-M-C arrangement of the CFT offers some implementation advantages over the M-C-M approach for group demodulation of DPSK. Because the longest duration, that is the largest TB product, chirp is used as a multiplying waveform, two chirp filters, each of one half the required time duration and bandwidth, and thus one fourth the required TB product, can be used to implement an effective single chirp waveform with the required characteristics. This arrangement also allows for 100% duty cycle operation, although in this case two, effectively large TB product, chirps must be used in a "ping-pong" or alternating chirp arrangement to provide the multiplier chirps.

To clarify this point, and illustrate the performance of this arrangement, consider the example given in [6] of processing a series of FSK tones by the C-M-C arrangement shown in Figure 3.3. This example also illustrates the relationship between corresponding input and output signal durations. The first convolution filter, sometimes referred to as a differential delay line, has the effect of delaying

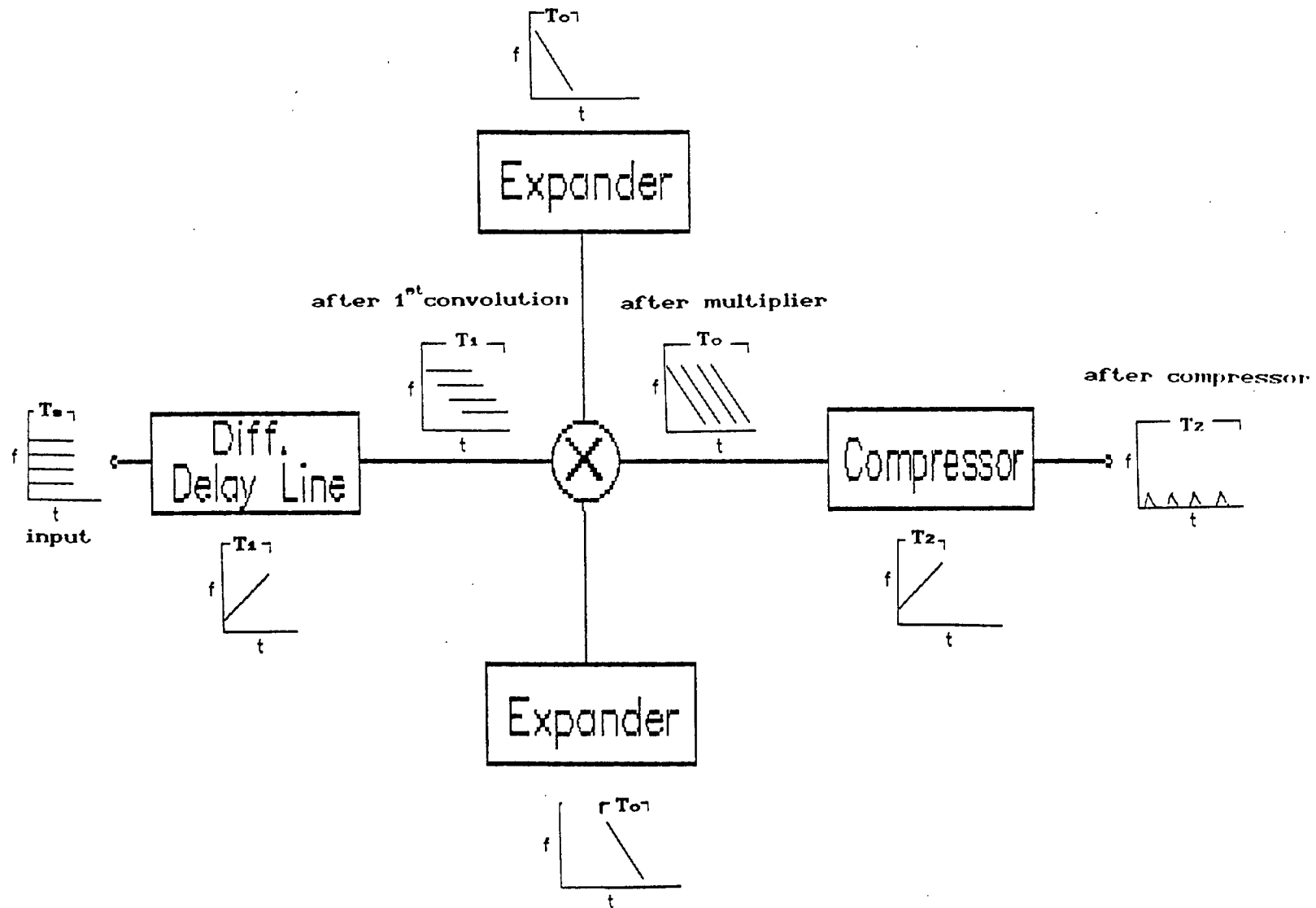


Figure 3.3 Processing FSK tones in the C-M-C arrangement with "ping-pong" multipliers

each input tone according to its frequency. Lower frequencies are delayed longest. These tones are then mixed with the down chirp of the multiplier, or expander. This produces a series of down chirps which, because of the effect of the first convolver, are delayed in proportion to their input frequency. These chirps then pass through the second convolution filter, or compressor, to produce a series of pulses corresponding to each of the original input tones. Note, however, that the analysis time of the compressor is of shorter time duration than the expander so two expanders are used in an alternating arrangement; thus the term "ping-pong" arrangement is used.

On input to the processor, each tone is of time duration T_s . The first convolution filter has an impulse response of duration T_1 , so after passing through this filter the signal will be of duration $T_s + T_1$. The multiplication chirp is of equal time duration to this signal, so $T_0 = T_1 + T_s$. The impulse response of the second convolution filter is only of duration $T_2 = T_1$, producing output signals of duration $T_0 + T_2$, however, only the middle T_2 portion of this output is considered the valid Fourier transform. By using the "ping-pong" technique illustrated, the two branches of the processor produce the valid transform output in alternating time segments, resulting in a 100% duty cycle capability.

The frequency resolution of the processor is determined

by the time-duration of the observation interval. A processing interval of T_s will produce frequency peaks of nominal separation $1/T_s$. Thus to analyse a bandwidth B_{IF} , the first convolution filter of the processor must have a time bandwidth product of

$$TB = B_{IF}/(1/T_s) = T_s B_{IF}. \quad (3.27)$$

To summarize these characteristics, Table 3.2 lists the critical parameters of the chirp filters required to perform a C-M-C CFT with a processor TB product of 128 and an analysed bandwidth of 2.56 MHz. In this table, the center frequency of the delay line, 100 MHz, corresponds to the assumed center of the analysed bandwidth and was chosen to meet the lowest attenuation range of LiNbO_3 , the assumed piezoelectric of the SAW device. When the delay line output is mixed with the expander output, sum and difference frequency components are created. The center frequency of the expander is chosen such that the resulting low frequency components match the bandwidth of the compressor filter. In this case the assumed IF_1 frequency is 100 Mz , so an expander center frequency of 250 MHz will create the desired low frequency components around 150 MHz, the center frequency of the compressor. The analysis period of the FT processor is assumed to be $T_H = 50 \mu\text{sec}$. Using the fact that $T_H = T_s = T_1 = T_2$, the compressor bandwidth is given as T_H

as well. Since, as noted in Table 3.1, $T_2 = T_0 + T_1$, a dispersion of 100 μsec is determined for the expander. The bandwidths listed are determined using the fact that $B = \mu T$, with $\mu = B_{\text{IF}}/T_H$ as dictated by equation (2.14b). The TB products listed are the result of multiplying bandwidth and dispersion. Notice that the TB=256 product of the expander can be realized with two SAW devices, each of TB=128.

Table 3.2 Critical Processor Parameters
For a Processor with 128 resolvable frequencies
and an Analysed Bandwidth of 2.56 MHz

SAW Device	center frequency	bandwidth	Dispersion	TB product
	MHz	MHz	μsec	
delay line	100	2.56	50	128
expander	250	5.12	100	256
compressor	150	2.56	50	128

3.4 The Inverse Fourier Transform Processor

The inverse Fourier transform (IFT) processor is constructed on the same principles as the forward transforms described in the previous section. Consider the generalized chirp Fourier transform relationship, similar to the definition given by Otto [11], and derived from equation 3.3 by substituting the relation $\Omega = \mu\tau$

$$F_{\mu}^{\tau} \left(f(t) \right) = \int_{-\infty}^{\infty} f(t) e^{-j2\pi\mu\tau t} dt \quad (3.28)$$

From this expression, the inverse transform relationship can be determined from the forward transformation as

$$F_{\mu}^{-\tau} \left(f(t) \right) = F_{\mu}^{\tau} \left(f(t) \right) \quad (3.29)$$

where the superscript $-\tau$ represents an inverse transform process, and the subscript $-\mu$ and μ represent chirps of opposite dispersion. Thus the inverse transformation is derived from the forward case simply by changing the direction (in frequency) of each SAW dispersive slope.

In the Inverse transform processor, the bandwidth which must be analysed corresponds to the allocated user bandwidth defined in section 2.1 as Δf_u . As indicated by

Table 3.1, this bandwidth corresponds to the bandwidth of the delay line and compressor, and is one half the bandwidth required in the expander. These values are indicated in Table 3.3. Since the magnitude of the dispersive slope of the IFT processor must be the same as that of the FT processor, the dispersion of each device can be calculated simply by dividing each bandwidth by this slope. The center frequencies and TB products given in Table 3.3 are calculated in the same manner as those of Table 3.2

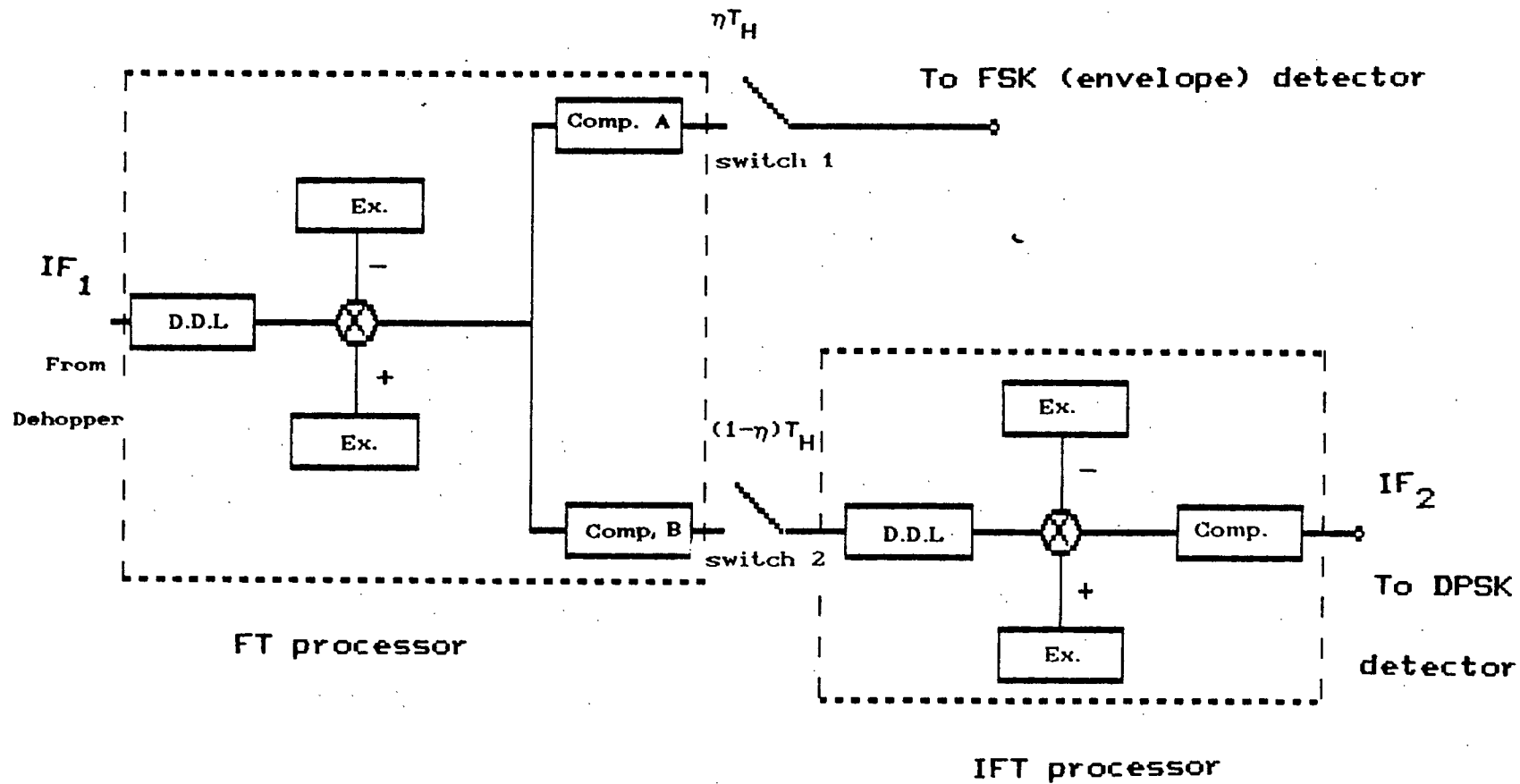
Table 3.3 Generalized SAW Device Characteristics for the IFT Processor

SAW Device	center frequency	bandwidth	Dispersion	TB product
	MHz	MHz	μsec	
delay line	100	Δf_u	$\Delta f_u / \mu$	$\Delta f_u^2 / \mu$
expander	250	$2\Delta f_u$	$2\Delta f_u / \mu$	$4\Delta f_u^2 / \mu$
compressor	150	Δf_u	$\Delta f_u / \mu$	$\Delta f_u^2 / \mu$

3.5 The Joint Group Demodulator

The complete demodulator is illustrated in Figure 3.4. In this illustration, the FT and IFT processors represent the same processors given in Felstead's demodulator, which was presented in Figure 2.2. Two compressor filters are used in the FT processor to implement independent FSK and DPSK windows. As described in Chapter two, the first ηT_H of each cycle corresponds to FSK processing, the output over this interval is N pulses corresponding to one tone per FSK user. During this interval switch one is closed and switch two is open. At $t = \eta T_H$ switch two closes, switch one opens and DPSK processing begins. Time gating to separate user spectrums is achieved by momentarily opening switch two at time intervals of $\Delta f_u / \mu$. This gated output is processed by the IFT to produce a TDMA formatted estimate of the ξ DPSK symbols.

As a numerical implementation example, Tables 3.4 and 3.5 list the critical SAW device parameters for the implementation shown in Figure 3.4. In this example, it is again assumed that $T_H = 50 \mu\text{sec}$. The IF bandwidth processed in the FT transform accommodates both the FSK and DPSK users; a value of 20.48 MHz is assumed. The resulting parameters shown in Table 3.4 are derived using the same techniques applied to Table 3.2. It should be noted



- , + = first and second half of "ping-pong" multiplier

D.D.L. = Differential Delay Line

Ex. = Expander

Comp. = Compressor

Figure 3.4 The Group demodulator based on the 100% duty cycle C-M-C configuration.

that the only difference in the impulse responses of compressors A and B in the FT processor is the window implemented. Following the conclusions of Ma [7], compressor A, the FSK branch of the detector, should use a Kaiser-Bessel windowing function. The DPSK windowing function is implemented in compressor B; this function is determined in Chapter 5.

Table 3.4 Critical Processor Parameters
For the FT Processor with
an Analysed Bandwidth of 20.48 MHz

SAW Device	center frequency	bandwidth	Dispersion	TB product
	MHz	MHz	μsec	
delay line	100	20.48	50	1024
expander	250	40.96	100	2048
comp. A	150	20.48	50	1024
comp. B	150	20.48	50	1024

For the IFT processor, a user bandwidth of $\Delta f_u = 5$ MHz is assumed, and μ is calculated using (2.14b). The tabulated results are determined following the procedures used for Table 3.3.

Table 3.5 Critical Processor Parameters
 For the IFT Processor with
 an Analysed Bandwidth of 5 MHz

SAW Device	center frequency	bandwidth	Dispersion	TB product
	MHz	MHz	μ sec	
delay line	150	5.00	12.21	61
expander	250	10.00	24.42	122
compressor	100	5.00	12.21	61

Some theoretical descriptions and implementation considerations for achieving SAW device impulse responses are given in appendix A. The simulations performed in this study are based on the use of a digital Fourier transform (DFT) to approximate the operation of a CFT processor. The analytical techniques used, results of these simulations, and the performance analyses are provided in Chapters four and five.

Chapter 4

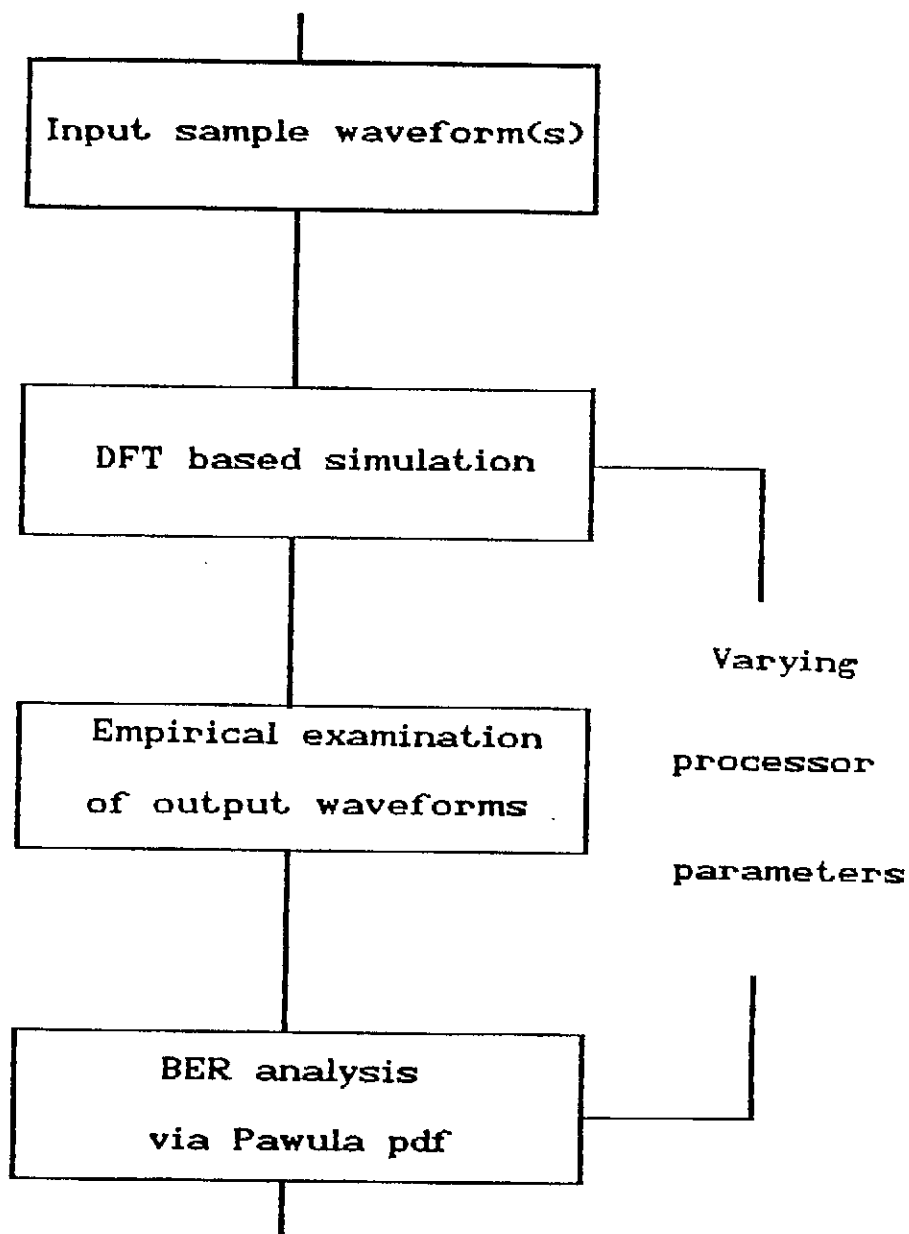
4.1 Analytical Method

In the simulations performed here, the SAW based FFT processor is modelled using standard digital Fourier transform algorithms on a VAX cluster with a MicroVax 2000 host computer. The methodology used is based on the quasi-analytical technique presented in [21]. It is based on simulating the performance of the processor in a noiseless environment, and using analytical techniques to estimate bit error rate (BER) performance.

In this thesis, the following methodology is applied in a two stage analysis. The first stage consists of using the DFT model to produce simulated output waveforms. Specifically, sample waveforms are input to the simulator, and an empirical analysis is made of the resulting (noiseless) output waveform. From these waveforms it is possible to determine the extent of waveform distortion caused by the FT/IFT processing. In some cases, such as the windowing study of section 5.2, some definite conclusions may be drawn after this examination, precluding the use of further (BER) analysis. More generally, however, a second stage analysis is performed. The second stage of the analysis is a BER calculation using the analytical

techniques presented by Boudreau [22]. As will be shown in the next section, this analytical technique is based on evaluation of the probability density function (pdf) defined by Pawula in [16] to yield symbol and bit error rates for DPSK. This two stage methodology is summarized by the flowchart in Figure 4.1.

Figure 4.1
Methodology of Analysis



4.2 Probability of Error Calculations

For the k^{th} baud interval, the DPSK symbol transmitted by user j can be expressed as

$$D_{jk}(t) = A \cos \left(\omega_c t + \phi_k \right) \quad \text{for } (k-1)T \leq t \leq kT \quad (4.1)$$

where

ω_c is the radian carrier frequency

A is the symbol amplitude

and

ϕ_k is the symbol phase.

Due to distortions caused by the FT/IFT processor, and the presence of narrow-band white Gaussian noise, the received signal input to the detector structure shown in Figure 4.2 becomes

$$s_k(t) = A_k(t) \cos \left(\omega_c t + \phi_o + \phi_k \right) + n_k(t) \quad (4.2)$$

where

$A_k(t)$ is the processor distorted estimate of A

ϕ_o is a random carrier phase offset

and

$n_k(t)$ is narrow-band white Gaussian noise.

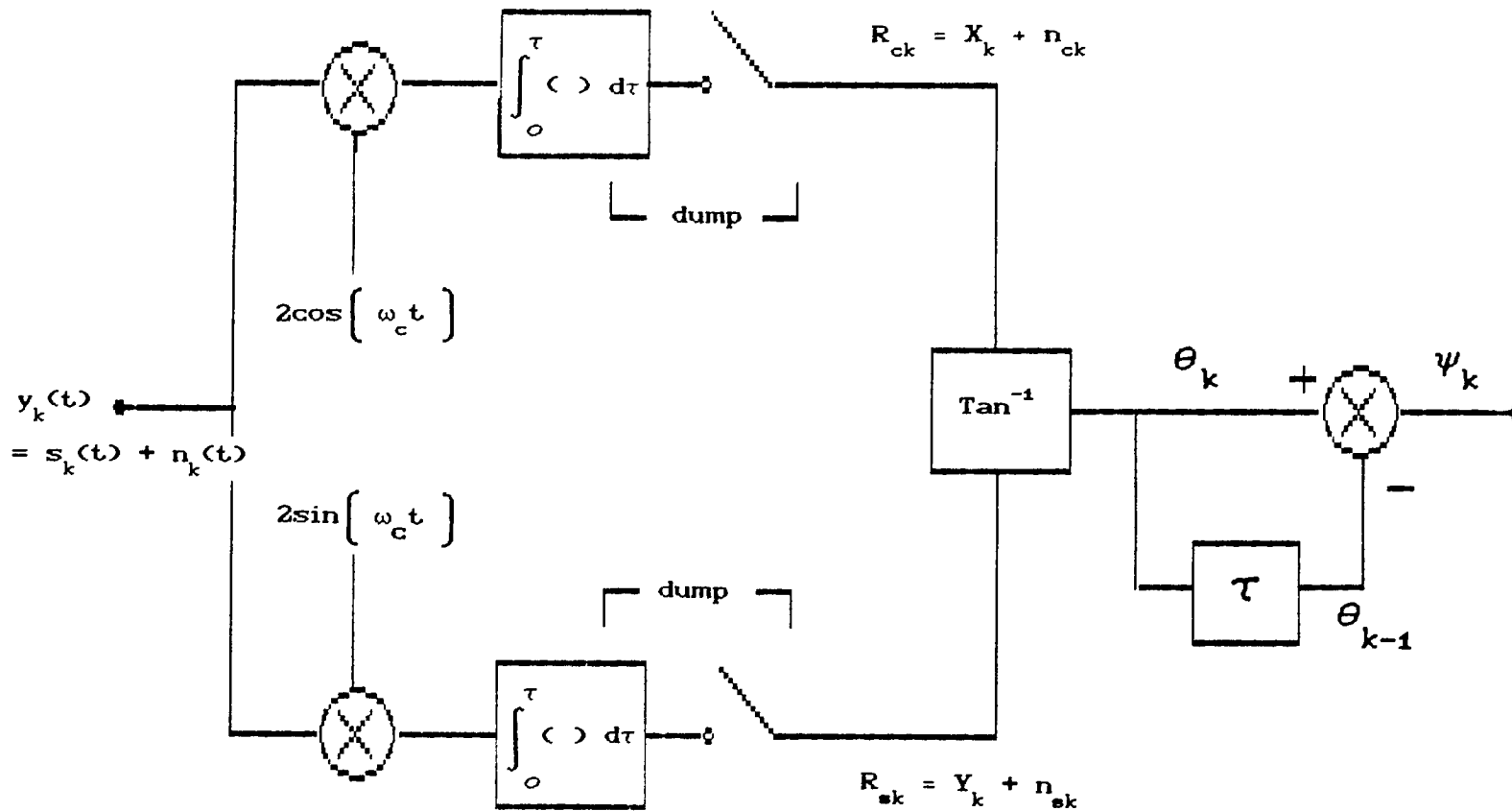


Figure 4.2 Detector Structure for Quaternary DPSK

Notice that in (4.2) and subsequent expressions, the subscript j has been dropped for notational convenience. As is shown in Proakis [27], equation (4.2) can be expanded and rewritten in the form of two carrier components in quadrature. Performing this expansion results in

$$s_k(t) = a_k A_k(t) \cos(\omega_c t + \phi_o) + b_k A_k(t) \sin(\omega_c t + \phi_o) + n_k(t) \quad (4.3)$$

where a_k and b_k are zero-mean random variables, which for quaternary signalling, can take on the values $\pm(2)^{-1/2}$.

Multiplication by $2\cos(\omega_c t)$ and $2\sin(\omega_c t)$ separates the received signal into, respectively, in-phase and quadrature components. On the in-phase arm of the receiver, the output of the integrate and dump filter is given by

$$R_{ck} = X_k + n_{ck} \quad (4.4a)$$

where

$$X_k = \int_0^T a_k A_k(t) \cos(\phi_o) dt \quad (4.4b)$$

and

$$n_{ck} = 2 \int_0^T n_k(t) \cos(\omega_c t) dt \quad (4.4c)$$

The corresponding quadrature-arm output is given by

$$R_{sk} = Y_k + n_{sk} \quad (4.5a)$$

where

$$Y_k = \int_0^T b_k A_k(t) \sin(\phi_o) dt \quad (4.5b)$$

and

$$n_{sk} = 2 \int_0^T n_k(t) \sin(\omega_c t) dt . \quad (4.5c)$$

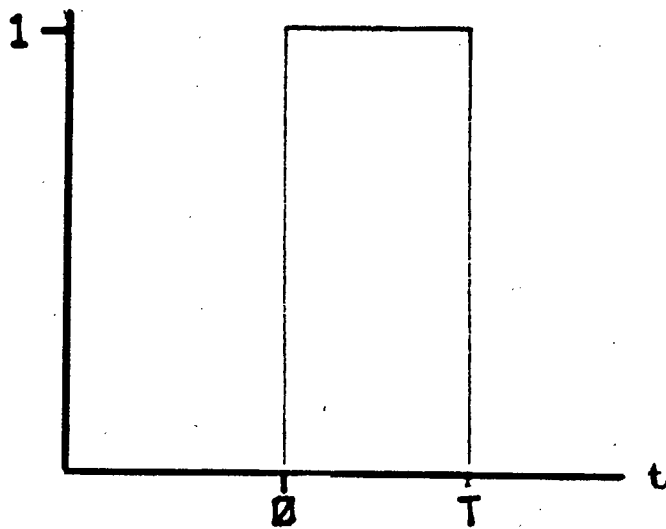
To account for symbol distortion, the time-varying symbol amplitude is defined as

$$A_k(t) = AP_k(t) \quad (4.6)$$

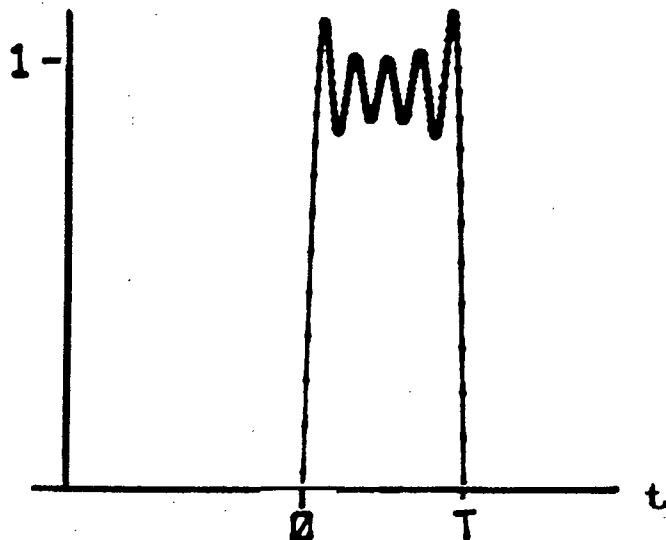
where, for an undistorted pulse, $P_k(t) = P_{rect}(t)$. $P_{rect}(t)$ is a rectangular pulse of unity amplitude and duration T , as shown in Figure 4.3a. In the general case, $P_k(t)$ is non-rectangular and non-linear and must be determined by numerically computing each symbol waveform. An example of a typical form for $P_k(t)$ is given in Figure 4.3b. To measure the extent of this distortion on the detector output, define λ_k as

Figure 4.3 Undistorted and Distorted Pulse Shapes

a) $P_{\text{rect}}(t)$



b) $P_k(t)$ where non-linear distortion is present



$$\lambda_k = \frac{\int_0^T P_k(t) dt}{\int_0^T P_{\text{rect}}(t) dt} \quad (4.7a)$$

$$= \frac{1}{T} \int_0^T P_k(t) dt . \quad (4.7b)$$

Substituting (4.7b) into (4.4b) and (4.5b) results in

$$X_k(t) = a_k AT \cos(\phi_o) \lambda_k \quad (4.8a)$$

and

$$Y_k(t) = b_k AT \sin(\phi_o) \lambda_k . \quad (4.8b)$$

Following the procedure used by Pawula in [15], the received signal can be expressed in vector notation. In this notation, the symbol vector becomes

$$\underline{A}_k = X_k + jY_k . \quad (4.9a)$$

$$= A_k e^{j\phi_k} \quad (4.9b)$$

where

$$A_k = |\underline{A}_k| = \sqrt{X_k^2 + Y_k^2} \quad (4.10a)$$

$$= AT\lambda_k \quad (4.10b)$$

The corresponding noise vector is

$$\underline{n}_k = n_{ck} + jn_{sk} \quad (4.11)$$

Thus, the vector representing the distorted and noise corrupted signal becomes

$$\underline{R}_k = \left(X_k + n_{ck} \right) + j \left(Y_k + n_{sk} \right) \quad (4.12a)$$

$$= R_{ck} + jR_{sk} \quad (4.12b)$$

$$= R_k e^{j\theta_k} \quad (4.12c)$$

where

$$R_k = |\underline{R}_k| = \sqrt{R_{ck}^2 + R_{sk}^2} \quad (4.13)$$

and

$$\theta_k = \arctan \left\{ \frac{R_s}{R_c} \right\} \quad (4.14a)$$

$$= \arctan \left\{ \frac{Y_k + n_{sk}}{X_k + n_{ck}} \right\} \quad (4.14b)$$

The decision variable for this detector is then given by the modulo 2π phase difference between baud intervals k and $(k-1)$. This phase difference is defined as ψ_k , where

$$\psi_k = \left(\theta_k - \theta_{k-1} \right) \text{mod}(2\pi) \quad (4.15)$$

The transmitted phase difference between vectors \underline{A}_k and \underline{A}_{k-1} is given for M-ary DPSK as

$$\Delta\phi_k = \phi_k - \phi_{k-1} \quad (4.16a)$$

$$= \frac{2(r-1)\pi}{M}, \quad (4.16b)$$

where

$$r = 1, 2, \dots, M. \quad (4.16c)$$

Figure 4.4 illustrates the relationship between these significant vector parameters. For quaternary DPSK, the possible transmitted phase differences, derived using (4.16b), are

$$\Delta\phi_k = \pm \pi/2, \pi, 0. \quad (4.17)$$

The corresponding decision regions for the detector are

$$\psi = \pm \pi/4, \pm 3\pi/4. \quad (4.18)$$

These decision regions are illustrated by Figure 4.5 where the vectors \underline{A}_k and \underline{A}_{k-1} have been normalized and plotted in polar form.

The probability that the phase difference between two vectors perturbed by narrow-band Gaussian noise lies in the range $\psi_1 \leq \psi_k \leq \psi_2$ is given by Pawula in [15] as

Figure 4.4 Phase Angle Between Two Vectors
 Perturbed by Gaussian Noise

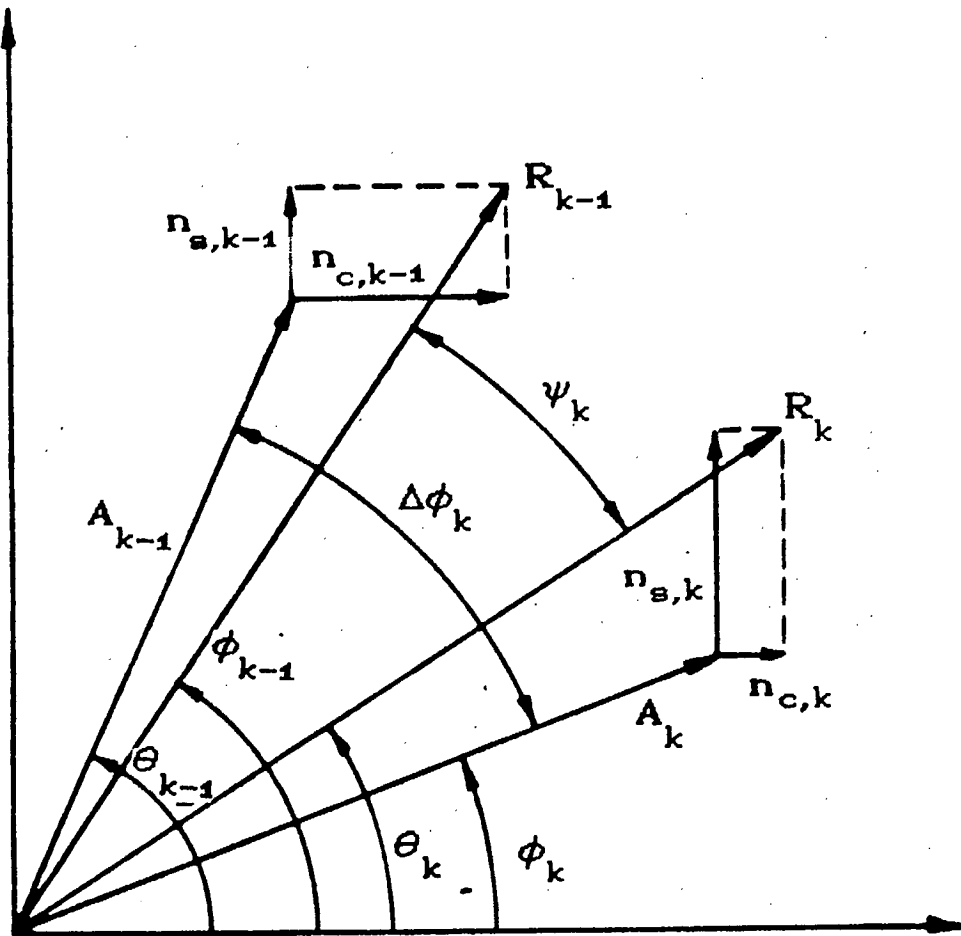
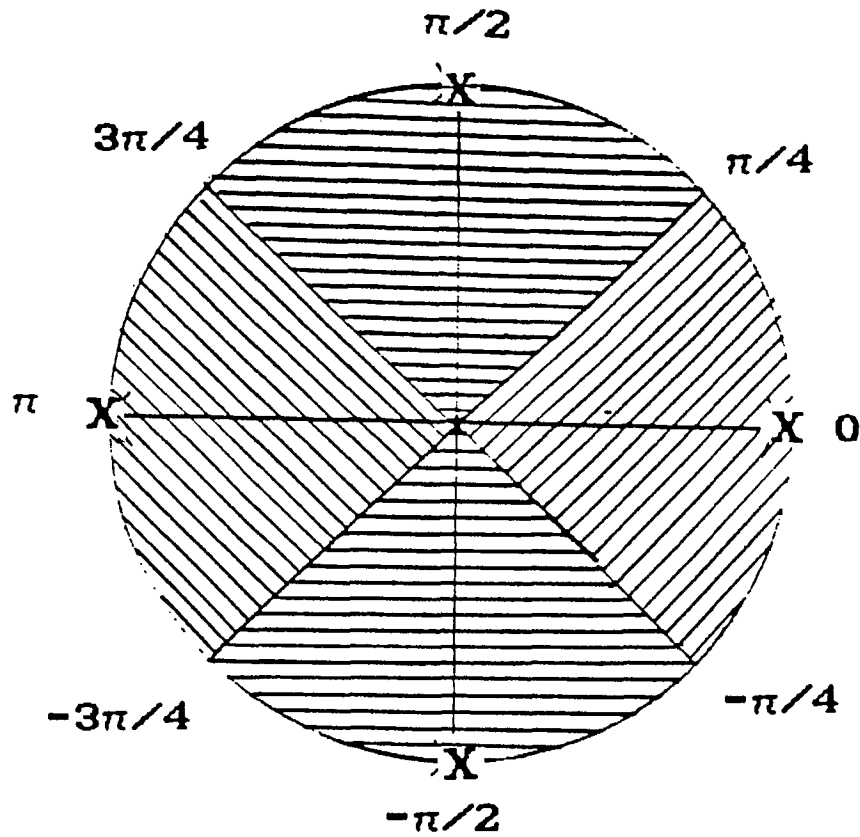


Figure 4.5

Decision Boundaries for DQPSK



x = possible transmitted vectors

decision boundaries

$$P\{\psi_1 \leq \psi \leq \psi_2\} = \begin{cases} F(\psi_2 | \Delta\phi_k, \rho_k, \rho_{k-1}) - F(\psi_1 | \Delta\phi_k, \rho_k, \rho_{k-1}) + 1 & \text{for } \psi_1 \leq \Delta\phi_k \leq \psi_2 \\ F(\psi_2 | \Delta\phi_k, \rho_k, \rho_{k-1}) - F(\psi_1 | \Delta\phi_k, \rho_k, \rho_{k-1}) & \text{otherwise} \end{cases} \quad (4.19)$$

where $F(\psi | \Delta\phi_k, \rho_k, \rho_{k-1})$ is the distribution function of ψ , conditioned on the transmitted phase difference and the received instantaneous signal to noise ratios ρ_k and ρ_{k-1} . $F(\psi)$ is defined in [15] as

$$F(\psi) = \int_{-\pi/2}^{\pi/2} dt \frac{e^{-E}}{4\pi} \left[\frac{W \sin(\Delta\phi - \psi)}{U - V \sin(t) - W \cos(\Delta\phi - \psi) \cos(t)} \frac{r_c \sin(\psi) - r_s \cos(\psi)}{1 - [r_c \cos(\psi) + r_s \sin(\psi)] \cos(t)} \right] \quad (4.20a)$$

where

$$E = \frac{U - V \sin(t) - W \cos(\Delta\phi - \psi) \cos(t)}{1 - [r_c \cos(\psi) + r_s \sin(\psi)] \cos(t)} \quad (4.20a)$$

$$U = \frac{1}{2} \left(\rho_k + \rho_{k-1} \right) \left[\log_2(M) \right]^{-1} \quad (4.20c)$$

$$V = \frac{1}{2} \left(\rho_k - \rho_{k-1} \right) \quad (4.20d)$$

and

$$W = \frac{1}{2} \sqrt{\rho_{k-1} \rho_k} \quad (4.20e)$$

The quantity ρ_k is defined as the instantaneous signal to noise ratio (SNR), and given by Boudreau [22] as

$$\rho_k = \frac{|\underline{A}_k|^2}{2\sigma^2} \quad (4.21)$$

The quantities r_c and r_s in (4.20) represent the autocorrelation and cross correlation between the in-phase and quadrature components of the narrowband noise. Proakis [27] shows that for narrow band white Gaussian noise

$$E [n_{ck} n_{sk}] = E [n_{c,k-1} n_{s,k-1}] = 0. \quad (4.22)$$

Furthermore, since the values n_{ck} and $n_{c,k-1}$ are formed by non-overlapping intervals

$$E [n_{ck} n_{c,k-1}] = E [n_{sk} n_{s,k-1}] = 0. \quad (4.23)$$

From (4.22) and (4.23) it is concluded that $r_c = r_s = 0$.

In [27], it is also shown that

$$\sigma^2 = E [n_c^2] = E [n_s^2] = N_0 T \quad (4.24)$$

where the power spectral density for white Gaussian noise is taken as $N_0/2$.

The quantity $|\underline{A}_k|^2$, calculated using (4.10b), is

$$|\underline{A}_k|^2 = A_k^2 = A^2 T^2 \lambda_k^2 \quad (4.25)$$

Substitution of (4.24) and (4.25) into (4.21) results in

$$\rho_k = \frac{A^2 T}{2N_0} \lambda_k^2 \quad (4.26)$$

Since the symbol energy for an undistorted symbol is given as

$$E_s = \int_0^T A^2 \cos^2(\omega_c t + \phi_o + \phi_k) dt \quad (4.27a)$$

$$= A^2 T / 2 \quad (4.27b)$$

The instantaneous SNR can be written as

$$\rho_k = \frac{E_s}{N_0} \lambda_k^2 \quad (4.28)$$

This result implies that the only effect the distorting pulse $P_k(t)$ has on DPSK detection performance is a scaling of the effective SNR by the value λ_k^2 .

Using the probability expression defined by (4.19), Pawula shows in [16] that the probability of symbol error on the k^{th} baud interval for M-ary DPSK can be expressed as

$$P_{\text{Se}}^k(M) = \frac{1}{M} \sum_{d=1}^M P(E|\Delta\phi_d, \rho_k, \rho_{k-1}) \quad (4.29)$$

where $P(E|\Delta\phi_d, \rho_k, \rho_{k-1})$ is the conditional symbol error probability given that $\Delta\phi_d$ was transmitted and ρ_k and ρ_{k-1} are, respectively, the signal to noise ratios of the received vectors over the k^{th} and $(k-1)^{\text{st}}$ baud intervals. Using equation (4.19), $P(E|\Delta\phi_d, \rho_k, \rho_{k-1})$ can be expressed as

$$P(E|\Delta\phi_d, \rho_k, \rho_{k-1}) = F\left(\Delta\phi_d - \frac{\pi}{M} \mid \Delta\phi_d, \rho_k, \rho_{k-1}\right) - F\left(\Delta\phi_d + \frac{\pi}{M} \mid \Delta\phi_d, \rho_k, \rho_{k-1}\right) \quad (4.30)$$

where

$\Delta\phi_d$ is a possible transmitted phase difference.

Using the decision regions defined in Figure 4.5, and equation (4.29), the probability of symbol error for $M=4$, assuming equiprobable symbols, is given by

$$P_{\text{Se}}^k(4) = \frac{1}{4} \left[P(E|\Delta\phi = 0, \rho_k, \rho_{k-1}) + \frac{1}{2} P(E|\Delta\phi = -\frac{\pi}{2}, \rho_k, \rho_{k-1}) + P(E|\Delta\phi = \frac{\pi}{2}, \rho_k, \rho_{k-1}) + \frac{1}{2} P(E|\Delta\phi = \pi, \rho_k, \rho_{k-1}) \right]. \quad (4.31)$$

Making use of equation (4.30) and noting from [16] that $F(\psi|\Delta\phi) = -F(-\psi|-\Delta\phi)$, this expression becomes

$$P_{se}^k(4) = 2 \left[F\left(-\frac{\pi}{4} | \Delta\phi = \frac{\pi}{2}, \rho_k, \rho_{k-1}\right) - F\left(\frac{\pi}{4} | \Delta\phi = 0, \rho_k, \rho_{k-1}\right) \right. \\ \left. + F\left(\frac{3\pi}{4} | \Delta\phi = \pi, \rho_k, \rho_{k-1}\right) - F\left(\frac{3\pi}{4} | \Delta\phi = \frac{\pi}{2}, \rho_k, \rho_{k-1}\right) \right]. \quad (4.32)$$

This symbol error probability can be converted to a probability of bit error using the relation given in [15] for the case $M=4$. Thus the probability of bit error for quaternary DPSK can be expressed as

$$P_{be}^k(4) = \frac{1}{2} P_{se}^k(4) + P\left(\frac{3\pi}{4} \leq \psi \leq \pi\right). \quad (4.33)$$

Using (4.19) to evaluate $P\left(\frac{3\pi}{4} \leq \psi \leq \pi\right)$, this expression becomes

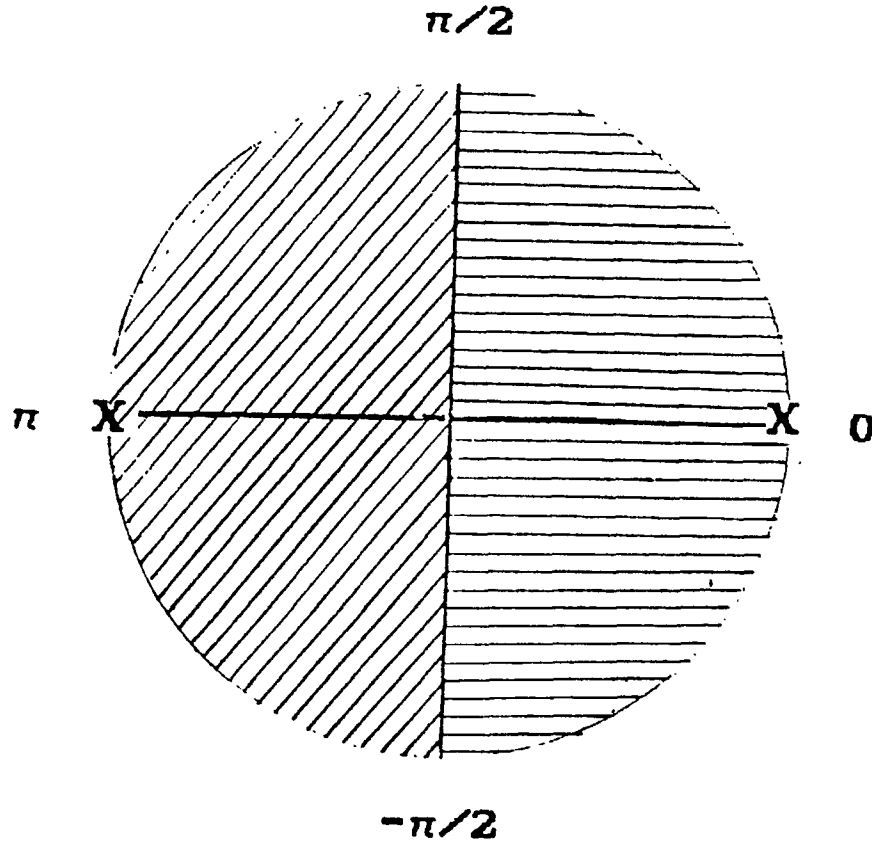
$$P_{be}^k(4) = \frac{1}{2} P_{se}^k(4) + F(\pi | \Delta\phi = 0, \rho_k, \rho_{k-1}) \\ - F\left(\frac{3\pi}{4} | \Delta\phi = 0, \rho_k, \rho_{k-1}\right). \quad (4.34)$$

The corresponding error probabilities for binary DPSK can be computed using the same technique. For the binary case ($M=2$), the possible transmitted phase differences become $\Delta\phi_k = \pm \pi$, resulting in the decision boundaries $\psi = \pm \pi/2$. The decision regions for DBPSK are shown in Figure 4.6. The probability of symbol error, again calculated assuming equiprobable symbols and using (4.29) becomes

$$P_{se}^k(2) = \frac{1}{2} P(E | \Delta\phi = 0, \rho_k, \rho_{k-1}) + \frac{1}{2} P(E | \Delta\phi = \pi, \rho_k, \rho_{k-1}). \quad (4.35)$$

Figure 4.6

Decision Boundaries for DBPSK



x = possible transmitted vectors

decision boundaries

Using equation (4.30) to express this in terms of $F(\psi)$ results in

$$P_{se}^k(2) = \frac{1}{2} \left[F\left(-\frac{\pi}{2} \mid \Delta\phi = 0, \rho_k, \rho_{k-1}\right) - F\left(\frac{\pi}{2} \mid \Delta\phi = 0, \rho_k, \rho_{k-1}\right) \right. \\ \left. + F\left(\frac{\pi}{2} \mid \Delta\phi = \pi, \rho_k, \rho_{k-1}\right) - F\left(-\frac{\pi}{2} \mid \Delta\phi = \pi, \rho_k, \rho_{k-1}\right) \right]. \quad (4.36)$$

Since this is a binary signalling case,

$$P_{be}^k(2) = P_{se}^k(2). \quad (4.37)$$

With these bit error expressions, it is possible to determine average bit error probabilities over the hop interval. The conditional probability of bit error, given that the j^{th} sequence of ξ symbols has been transmitted, denoted $P_{be}(M|D_j)$, can be expressed as the average of the probability of bit error for each of the baud intervals, so

$$P_{be}(M|D_j) = \frac{1}{\xi - 1} \sum_{i=2}^{\xi} P_{be}^k(M). \quad (4.38)$$

The bit error rate (BER) is then the average of $P_{be}(M|D_j)$ over all possible sequences. This is calculated as

$$P_{be}(M) = \frac{1}{M^\xi} \sum_{j=1}^{M^\xi} P_{be}(M|D_j) \quad (4.39a)$$

$$= P_{be}(M|D_0). \quad (4.39b)$$

In (4.39) it is assumed that each sequence is equally likely, and the particular sequence $D_j = D_0$ is sent.

When a multi-user environment is considered, the same technique can still be applied. Since $P_k(t)$, the distortion in each pulse, is calculated numerically via a waveform simulation, the effect of any interfering users on the reference user is incorporated into the calculation of λ_k . The interference condition which exists when the reference user sends the j^{th} sequence is the net effect of one or more interfering users. This interference condition is denoted I_j . If there are $L-1$ interfering users of M -ary DPSK, each transmitting ξ symbols per hop, the average BER is calculated as

$$P_{be}(M) = ((L-1)M^\xi)^{-1} \sum_{j=1}^{(L-1)M^\xi} P_{be}(M|D_0, I_j). \quad (4.40)$$

As indicated, equation (4.40) requires $(L-1)M^\xi$ iterations. In this study the average BER is approximated by computing $P_{be}(M)$ over S iterations, so

$$P_{be}(M) \cong \frac{1}{S} \sum_{l=1}^S P_{be}(M|D_o, I_j) \quad (4.41)$$

where the value of S is determined empirically and given explicitly in the following section.

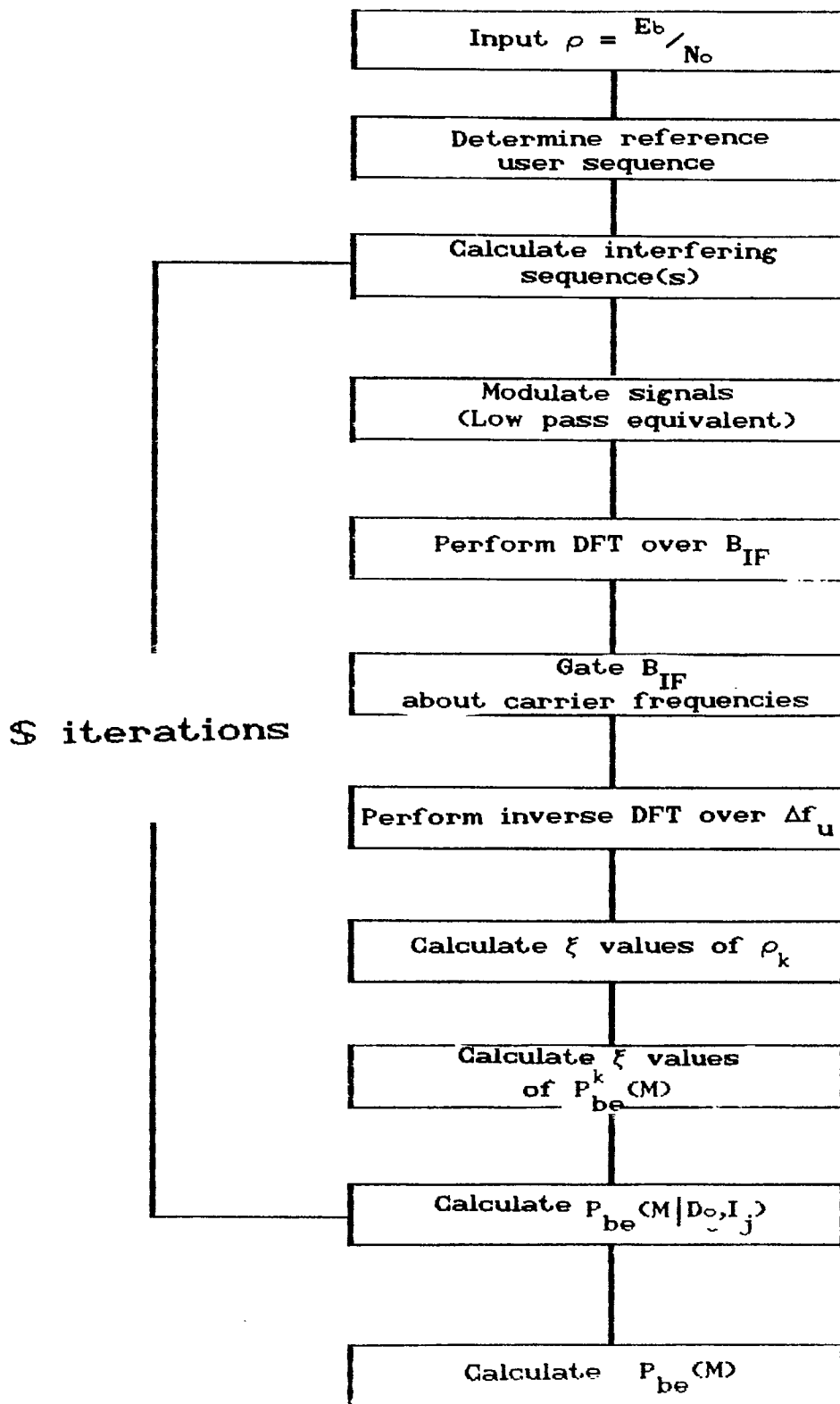
4.3 Computational Considerations

Figure 4.7 is a flowchart of the computational algorithm implemented for the waveform and BER analysis. For the first stage of the quasi-analytical method, the waveform analysis, BER calculations are not performed so the algorithm is run only up to the point where an inverse DFT is performed. The waveforms illustrated in the following chapter are extracted at this point in the algorithm. When BER calculations are performed, S iterations are run to determine the error rate value at each input SNR. In this routine the DFT is implemented using a standard FFT; the number of points used is a parameter under study but at this point it is set at 2048.

Because the effects of noise are accounted for analytically, relatively few iterations of the hop sequence are required, compared to a Monte Carlo simulation, to provide a good degree of accuracy. It was empirically determined that varying the number of hop iterations from

Figure 4.7

Generalized BFF waveform algorithm



250 to 500 resulted in an average variation of less than 5%. It should be noted though, that 250 iterations of the hop sequence corresponds to 250x probability of bit error calculations.

The distribution of the phase difference $F(\psi)$ is calculated numerically using a simple trapezoidal rule integration routine supplied by Mason [23]. Again, the accuracy of this routine was confirmed empirically to be better than 2%.

Some discrepancies between the computer based DFT and SAW based CFT should be discussed at this point. The primary difference is that the CFT is a continuous transform algorithm. For the simulations performed subsequently, the DFT is assumed to be a sampled version of this continuous output. Because the duration of the sampling interval is finite, each spectral component of the CFT will be spread over a nominal frequency range. It is implicitly assumed that this spreading is equivalent to the frequency resolution of the DFT. This resolution, in the Fourier domain, is $\frac{1}{T_H}$.

Chapter 5: Computational Results

5.1 Outline of Simulation Results:

In earlier Chapters the operation of SAW devices for the demodulation of differential phase shift keyed modulation has been explained. In Chapter 4 it was shown how a BER analysis of the Felstead receiver can be conducted. Recall from Chapter 4 that the analysis technique consists of two stages. First, an analysis of the baseband, noiseless waveforms for data symbol detection are examined to see if they are distorted relative to the ideal case. When distortion is large or small, further analysis is not needed. For the former case, the BER results will be poor. For the latter they will agree with the ideal case. In other cases a BER analysis must be conducted in order to determine the SNR loss relative to the ideal case.

In this Chapter the following possible performance degradations for the Felstead receiver of Figure 2.2 are examined: (1) receiver windowing; (2) transform truncation; (3) receiver TB product; and (4) receiver phase and amplitude non-linearities. As will be indicated, these effects are either related to the double Fourier transform structure of Felstead's receiver or to the fact that it is realized using practical SAW devices.

5.2 Windowing Considerations:

It has been demonstrated elsewhere [7],[24] that for practical FSK demodulation, windowing of the transform is required. In those cases, the effect of tapering the amplitude of the signal at the beginning and end of the symbol period makes the transform demodulator significantly more robust in practical cases where frequency offsets occur at reception. Windowing has also proven beneficial in DPSK detection when performed over a symbol duration [2]. One of the potential advantages offered by the receiver studied here is the lack of symbol level timing for the DPSK transform. To maintain this simplicity, the windowing must be performed over the hop period T_H , corresponding to ξ DPSK symbols.

For the initial simulations, a standard 2048 pt. DFT algorithm is used for the FT/IFT processor. It is assumed that $T_H = 50 \mu\text{sec}$, thus the frequency resolution of the processor is 20 KHz. At this point it is sufficient to consider only DBPSK. For convenience in implementation, $\xi=50$. Although this corresponds to a data rate of only 1 Mbps, frequency scaling is used to generalize these results. The windows considered here are the rectangular (no amplitude tapers), and a sample window from the Kaiser-Bessel (KB) windowing family. The Kaiser-Bessel

window is described analytically , in discrete form, by

$$W(n) = \frac{I_0 \left\{ \beta \sqrt{1 - (2n - N_w - 1 / N_w - 1)^2} \right\}}{I_0 \{ \beta \}} \quad (5.1)$$

where

I_0 is the zero order modified Bessel function

N_w is the number of points in the window

and

β is the bandwidth expansion factor.

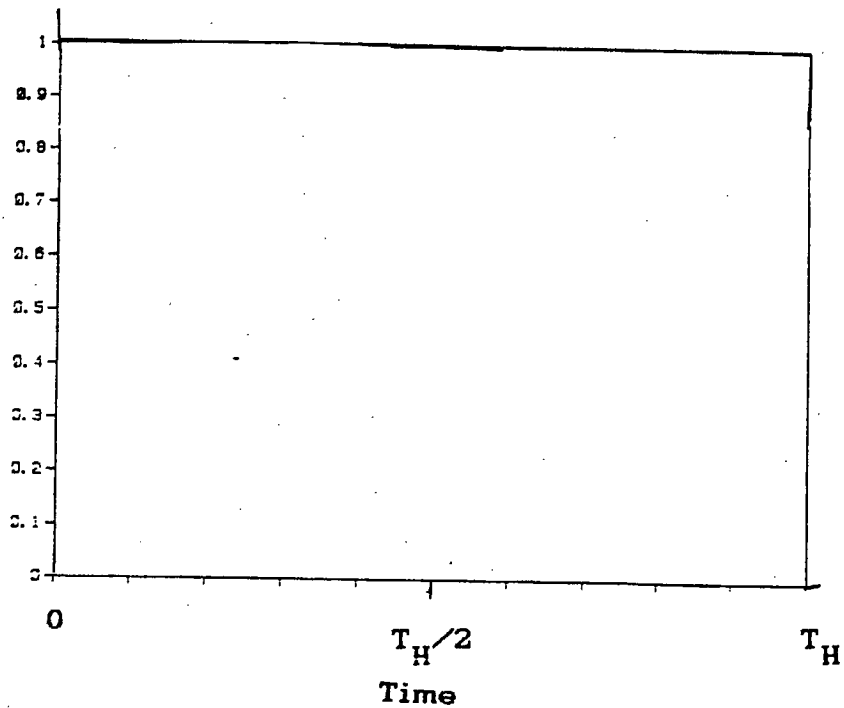
In this study $\beta = \pi$. These windows are plotted in Figures 5.1a, and 5.1b. Figure 5.2 illustrates the sample input binary sequence of the reference user.

Figures 5.3 shows the FFT output when only the reference user is active and rectangular windowing of the transform is performed. For the corresponding inverse Fourier transform, a user bandwidth of $\Delta f_u = 2/T$ is assumed. The bandwidth allocated to the reference user is termed channel one. The neighbouring $2/T$ bandwidth is termed channel two.

Figure 5.4 illustrates sample waveform output over (a) channel one, and (b) channel two when only the reference user is active and rectangular windowing of the transform has been performed. From 5.4a, the distortion caused by the FT/IFT processor is evident. The ripple present over this

Figure 5.1 Windows Examined

a) Rectangular



b) Kaiser-Bessel Window with $\beta = \pi$

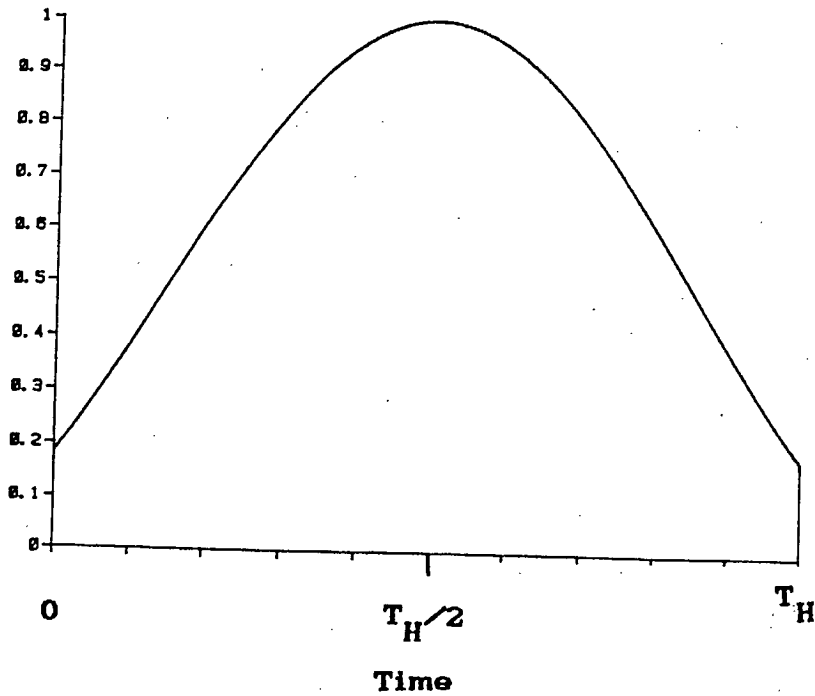


Figure 5.2 Input Binary Sequence

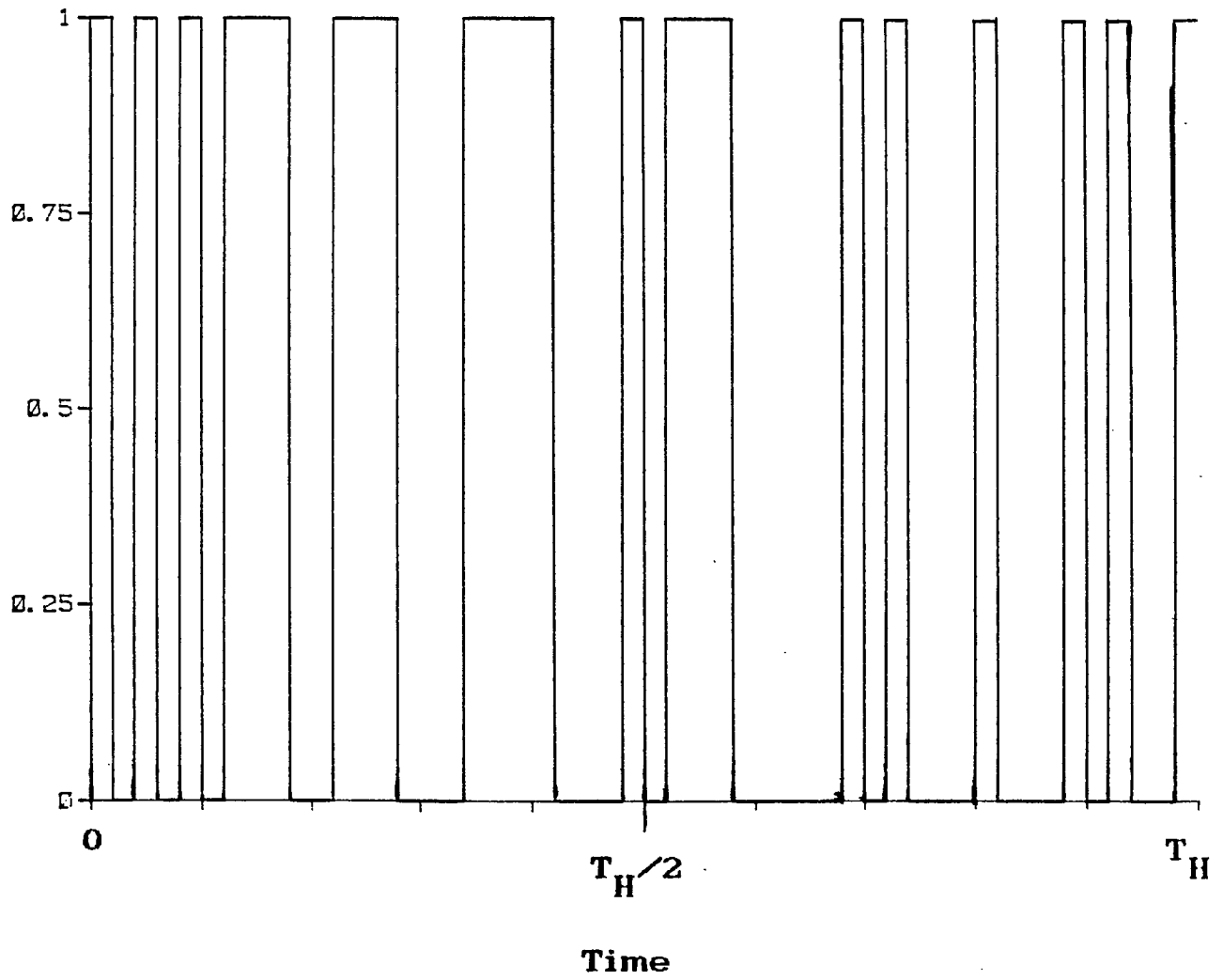


Figure 5.3

FFT Output with One Active User

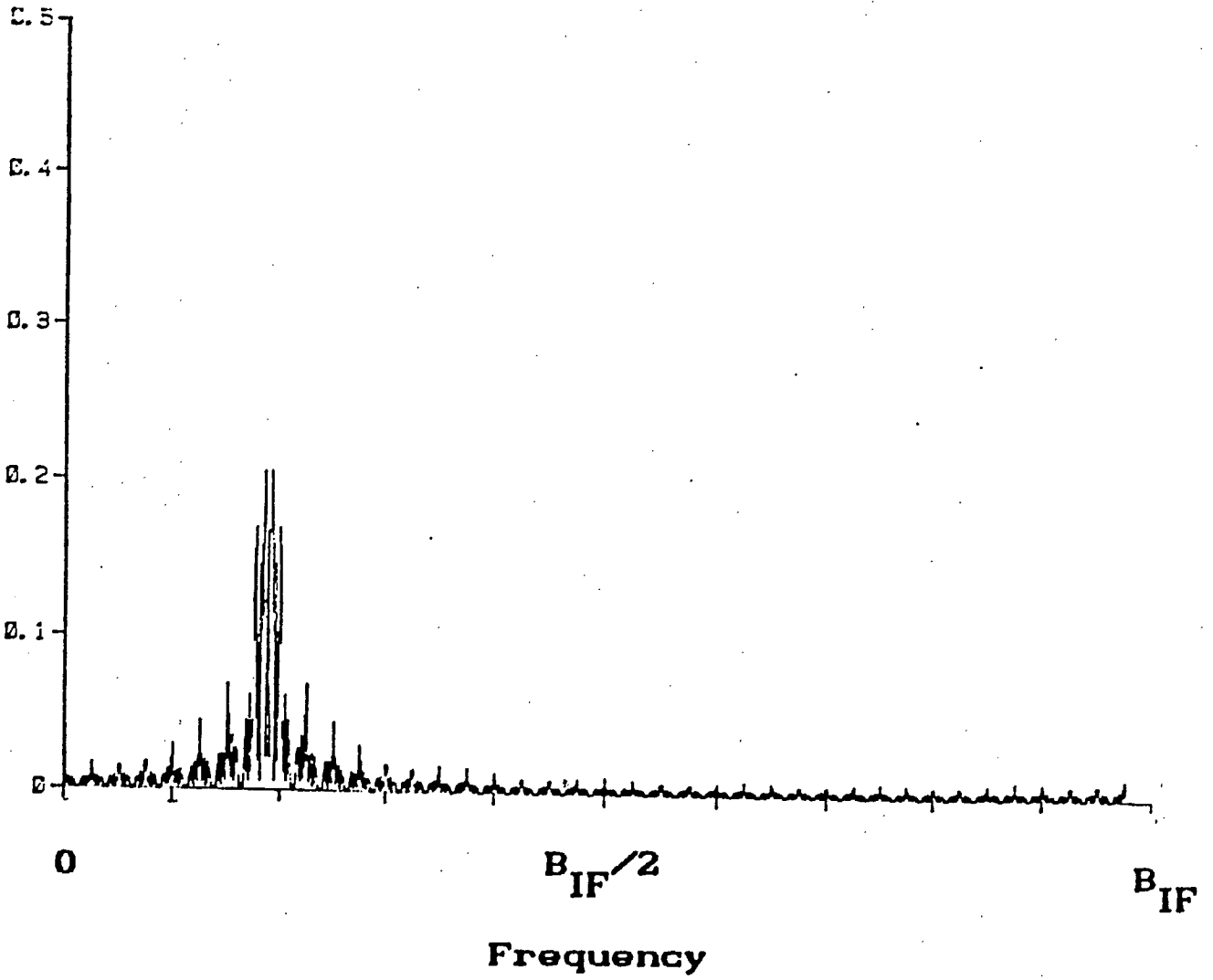
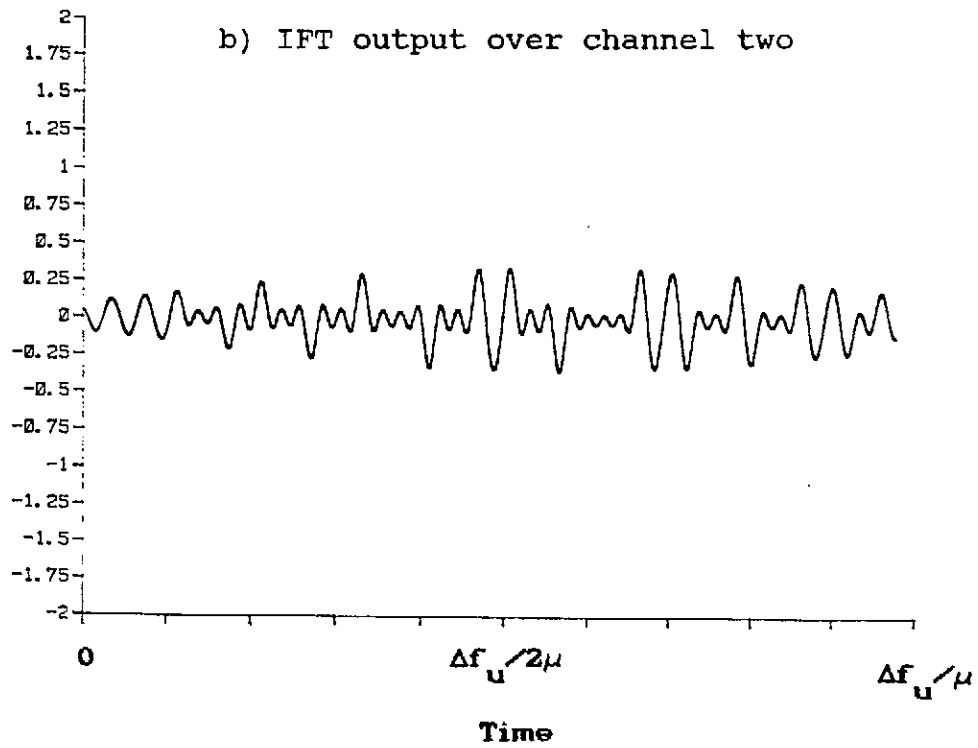
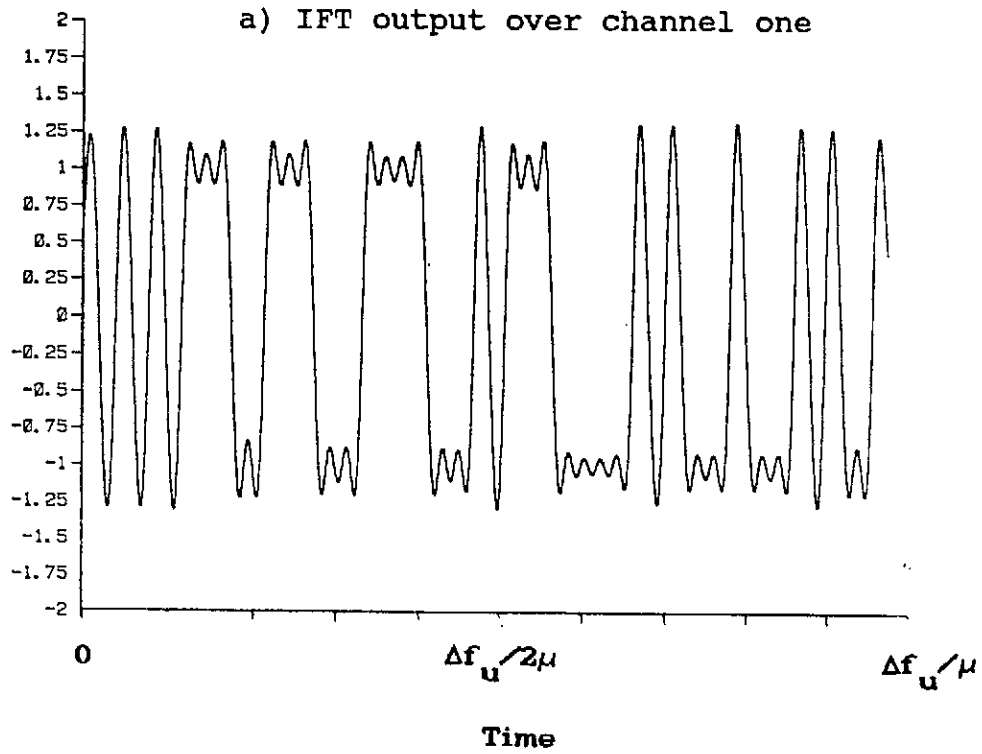


Figure 5.4

One Active User with Rectangular Windowing of the Transform



output is the well known Gibbs phenomena and is due to truncation of the spectrum, an effect unaccounted for in Felstead's presentation [3].

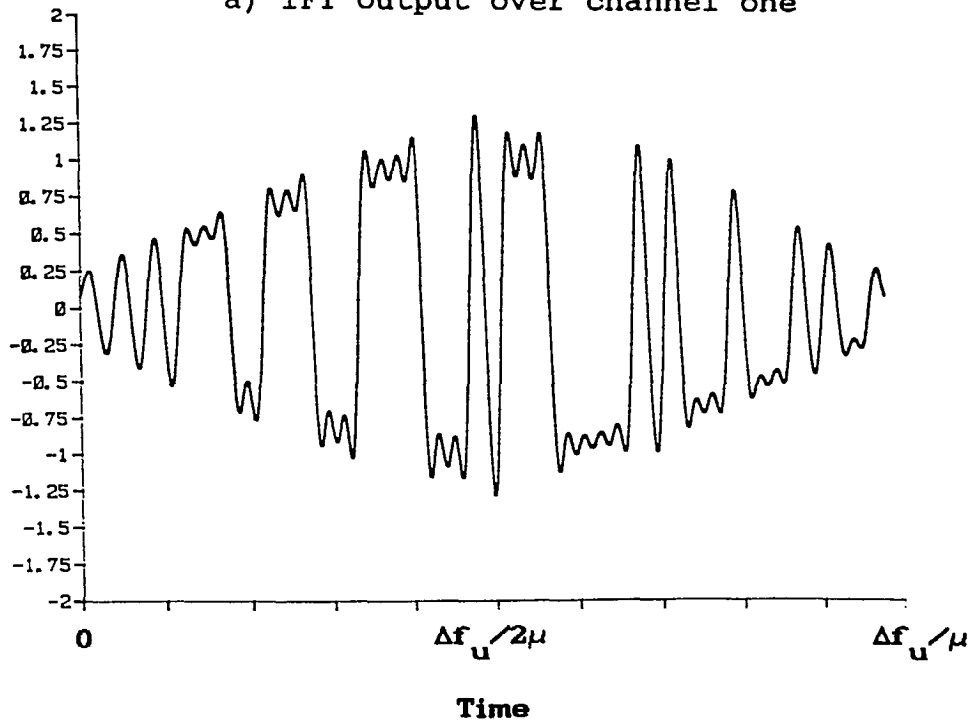
The arbitrary time/frequency scales of Figures 5.3, 5.4 and subsequent waveforms outputs should be noted at this point. To maintain generality of the SAW processor parameters, the frequency scale representing the spectrum (Fourier domain) of the input waveform is demarked as a fraction of $B_{\text{dpsk}} = \mu(1-\eta)T_H$. The output of the IFT processors is given as a fraction of the TMD time slot allotted to each user. Each of these time slots is of $\Delta f_u/\mu$ seconds in duration, as noted in Chapter 2.

Figure 5.5a and 5.5b represent the same situation as Figure 5.4, but in this case the Kaiser-Bessel window was used over the transform. Notice from 5.5a that the presence of this window creates severe distortion of the initial and final symbols of each hop. The output on channel two, shown in 5.5b also exhibits the envelope characteristic of the Kaiser-Bessel window. Comparing this output with Figure 5.4b, it seems the ACI on channel two is not significantly reduced by the tapered window.

Figure 5.6 illustrates the spectral result for two active users with a carrier separation of $2/T$ Hz. The user bandwidths corresponding to channels one and two, both equivalent to Δf_u , are also indicated on this figure.

Figure 5.5 One Active User with
a Kaiser-Bessel Window on the Transform

a) IFT output over channel one



b) IFT output over channel two

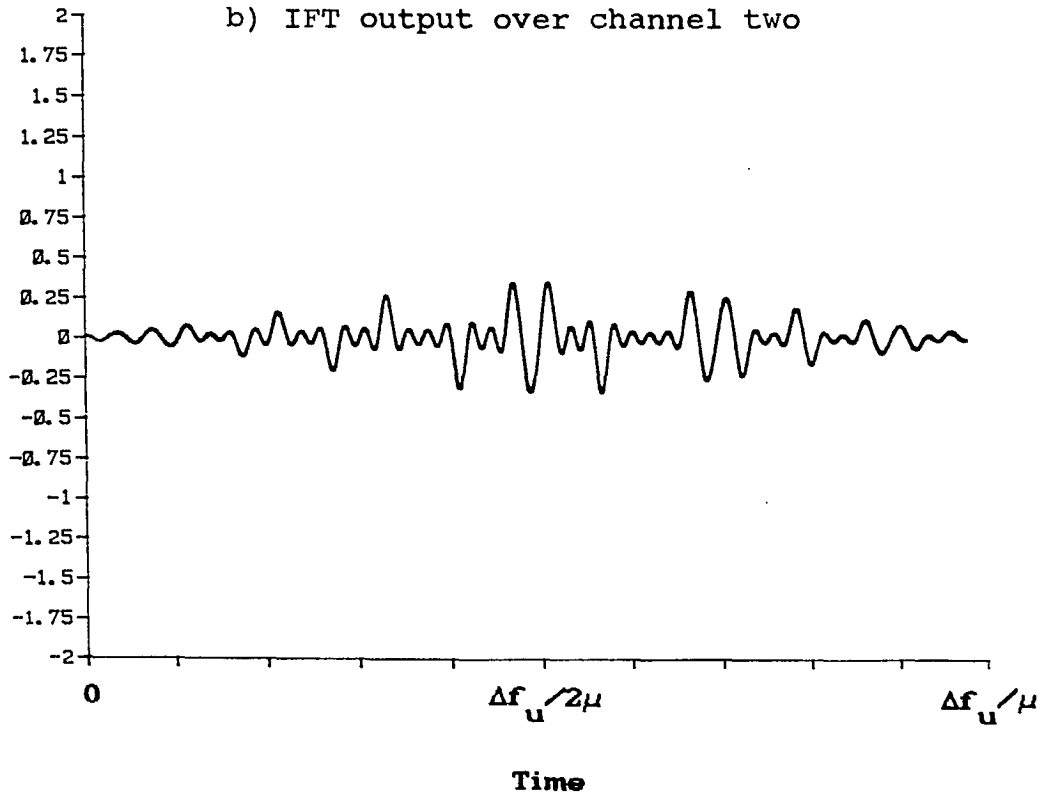


Figure 5.6

Simulated Spectral Output for Two Active Users
with a Carrier Separation of $\Delta f_u = \frac{2}{T}$.

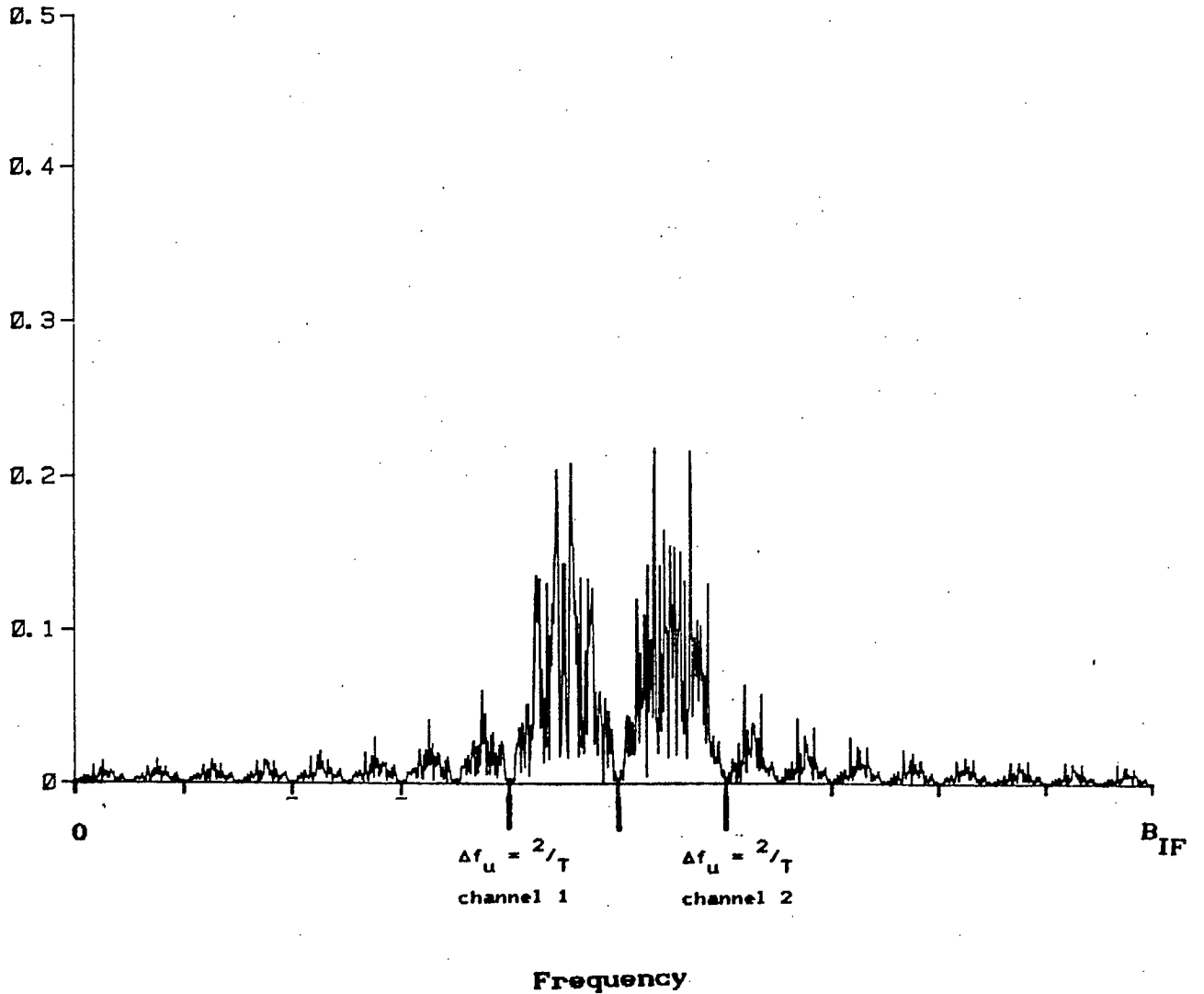


Figure 5.7a illustrates the IFT output on channel one when the interfering user is at equal power to the reference user and the Kaiser-Bessel window has been used on the transform. In Figure 5.7b the same window is used but the interfering user is at 9 dB greater power than the reference user. Note that even in this case the window provides negligible ACI reduction, especially when compared to the distortion it creates. This can be proven analytically as follows: The windowed Fourier transform output of the FFT can be expressed as

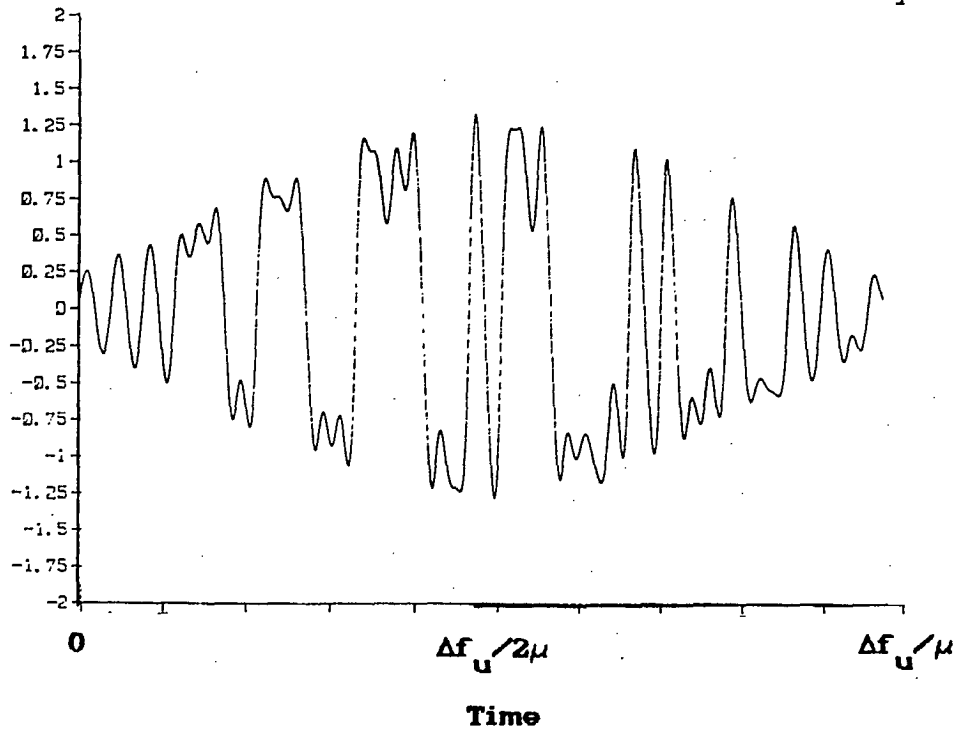
$$FT\{w(t)u_j(t)\} = FT\{w(t)\} * FT\{u_j(t)\} \quad (5.2a)$$

$$= W(f) * U_j(f) \quad (5.2b)$$

where $u_j(t)$ represents the baseband DPSK signal as in equation (2.6), and $w(t)$ represents the DPSK windowing function implemented in the processor. $W(f)$, the Fourier transform of $w(t)$, is given in Figure 5.8a for a rectangular window, and for the KB window with $\beta=\pi$ in Figure 5.8b. Compare this with the DBPSK spectrum $U_j(f)$ shown in 5.3. The spectrum $U_j(f)$ has, for the DBPSK case, nulls at frequency spacings of $1/T$ and a main lobe width of $2/T$. In contrast, $W(f)$ has nulls at frequency spacings of $1/\xi T$. As a result, $W(f)$ appears as an effective impulse relative to $U_j(t)$. Equation (5.2) can then be expressed as:

Figure 5.7 Two Active Users with
a Kaiser-Bessel Window on the Transform

a) Output over channel one with interferer at equal power.



b) Output over channel one with interferer at 9dB greater power than the reference user.

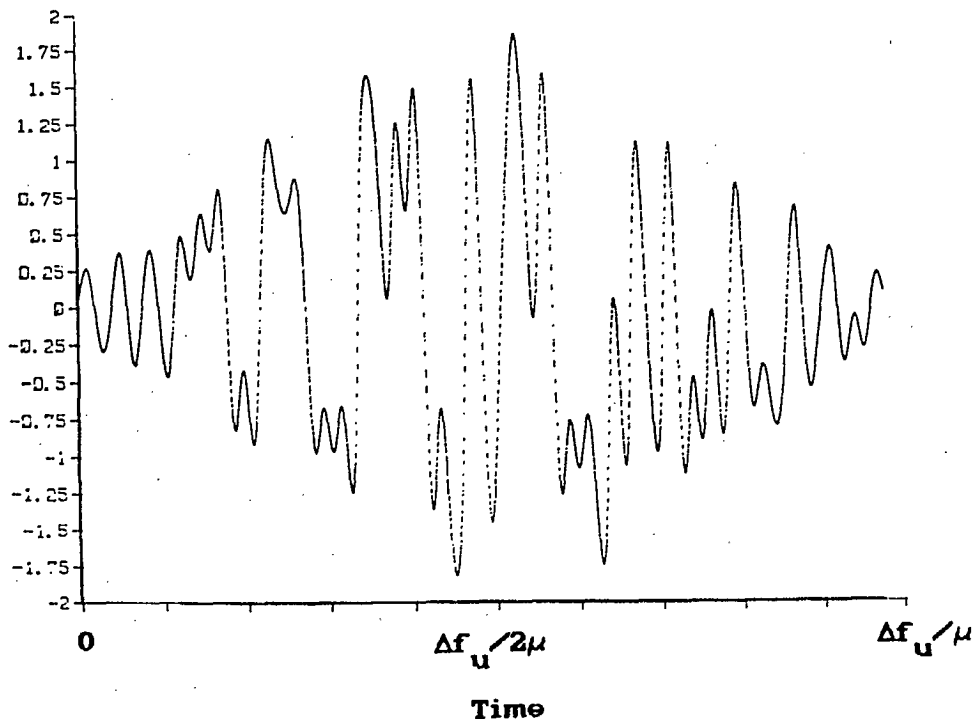
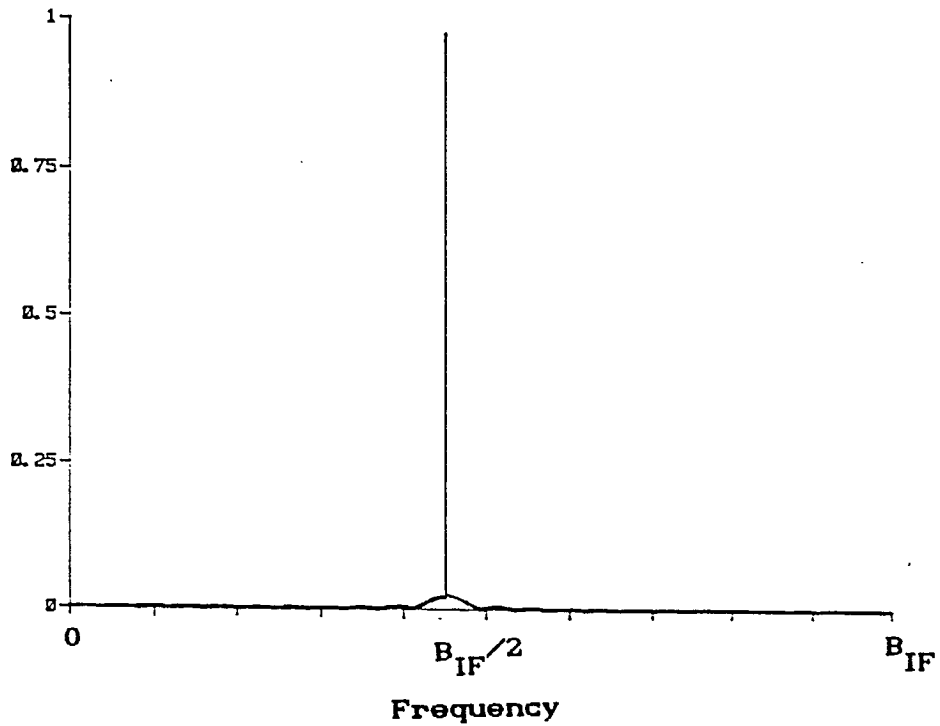


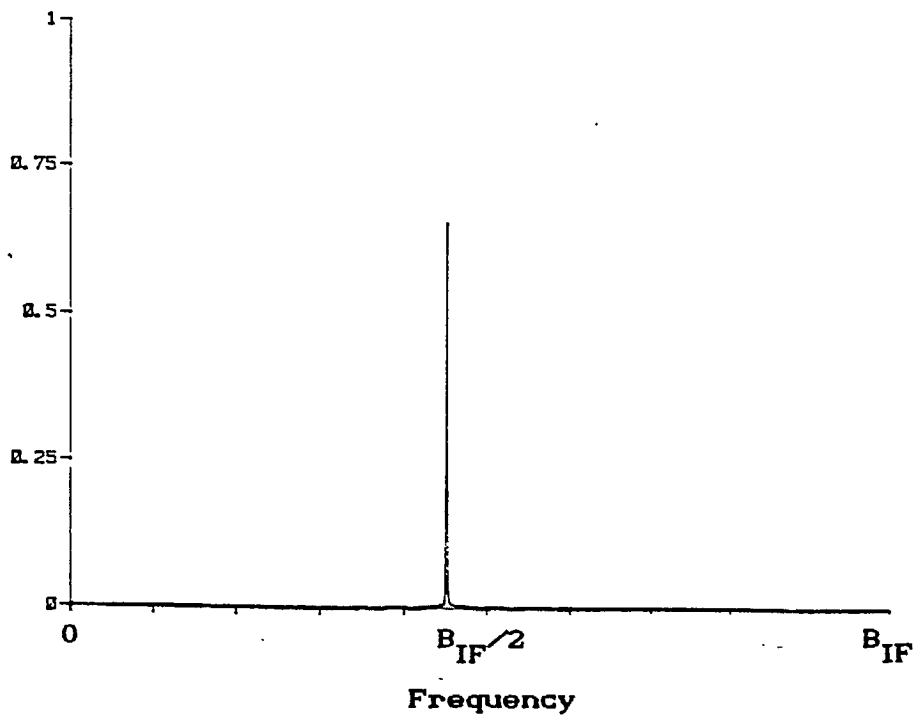
Figure 5.8 $FT\{w(t)\} = W(f)$

Fourier Transform of the Windowing Functions

a) Spectrum of a rectangular window



b) Spectrum of a KB window with $\beta = \pi$



$$W(f) * U_j(f) \cong \delta(f) * U_j(f) \quad (5.3a)$$

$$= U_j(f) \quad (5.3b)$$

This result indicates that rectangular windowing will provide the optimum DPSK performance for the Felstead receiver. All other windowing functions yield an SNR penalty with no ACI reduction. In subsequent studies only the rectangular window will be considered. Furthermore, this result implies that any form of windowing must be performed in the transmission of the data by use of spectrally efficient modulating techniques. In the next section binary and quaternary DPSK are compared in this respect. Since this result is conclusive, a BER analysis is not required.

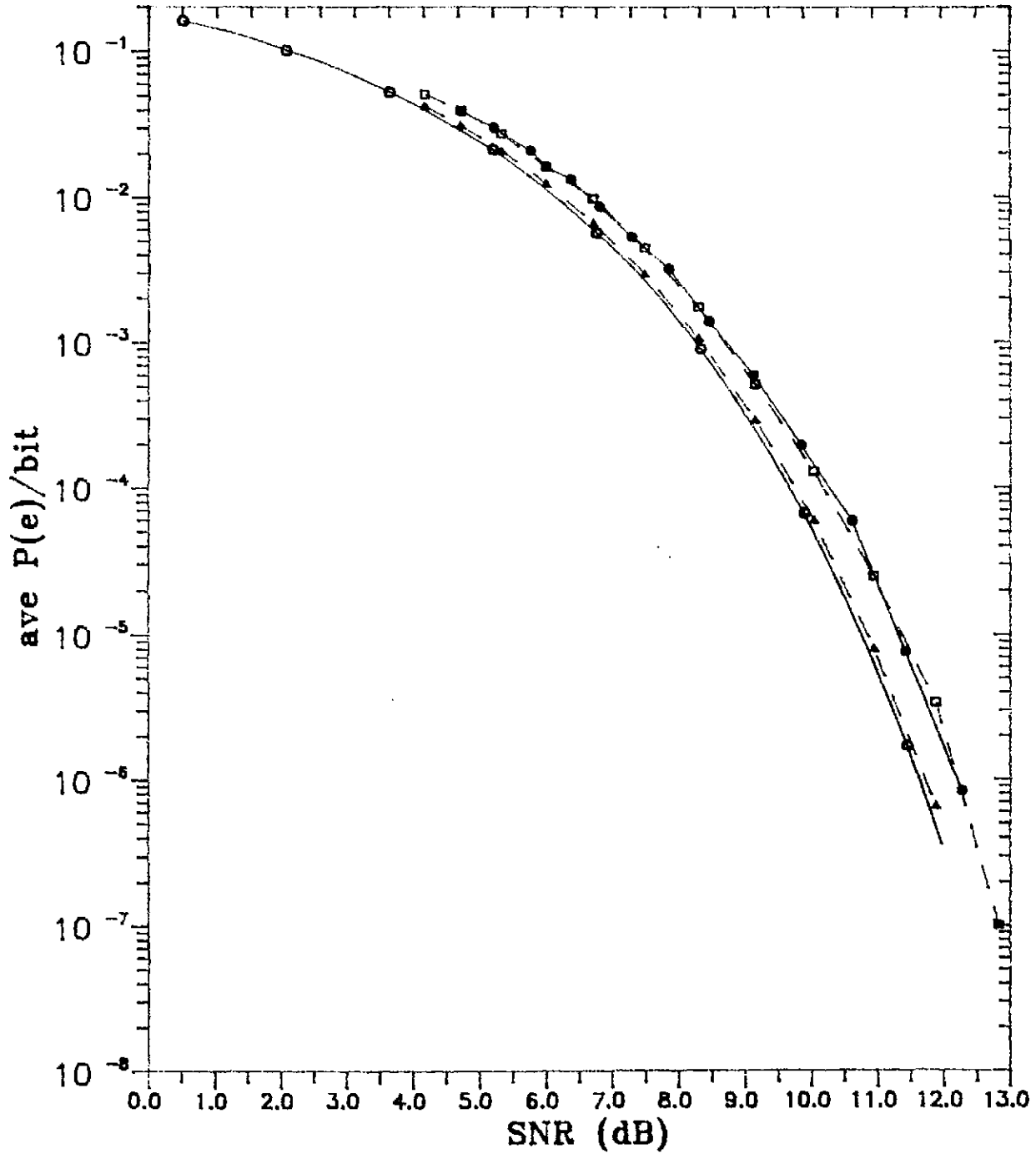
5.3 Transform Truncation Considerations

In the previous section it was assumed that both the FDMA carrier separation and the user bandwidths (Δf_u) are equal to $2/T$. In this section the effect of varying Δf_u on demodulator performance is considered.

Figure 5.9 shows average BER results, calculated as dictated in Chapter 4, for optimum detection of binary DPSK compared with the performance of the Felstead receiver having $\Delta f_u = 2/T, 2.5/T$ and $5/T$ where T in this and in subsequent studies is taken as the symbol duration in binary

Figure 5.9

BER Performance for DBPSK with Varying Δf_u .



Average P_e /bit for one user DBPSK with $\Delta f_u = 5/T, 2.5/T, 2/T$, and optimum detection.

oooo optimum detection
 ●●●● $\Delta f_u = 2/T$
 □□□□ $\Delta f_u = 2.5/T$
 ▲▲▲▲ $\Delta f_u = 5/T$

DPSK. As this figure indicates, truncation of the user bandwidth at $5/T$ results in Figure 5.9 slightly sub-optimal performance. When Δf_u is decreased to $2.5/T$, demodulator performance is degraded by about 0.75 dB. Decreasing Δf_u to $2/T$, the value assumed in the previous section, does not create any further performance degradation.

A user bandwidth of $\Delta f_u = 5/T$ would result in excessively large bandwidth requirements for the SAW devices used in the FT processor. In this case, for example, a group demodulator for four DPSK users would have to analyse a bandwidth of $B_{\text{dpsk}} = 4 \times 5 \times 1.54 \text{ MHz} = 30.80 \text{ MHz}$. Considering that the same bandwidth could be used to demodulate 10 users with $\Delta f_u = 2/T$ at a penalty of only about 0.75 dB, the merits of a smaller user bandwidth become evident.

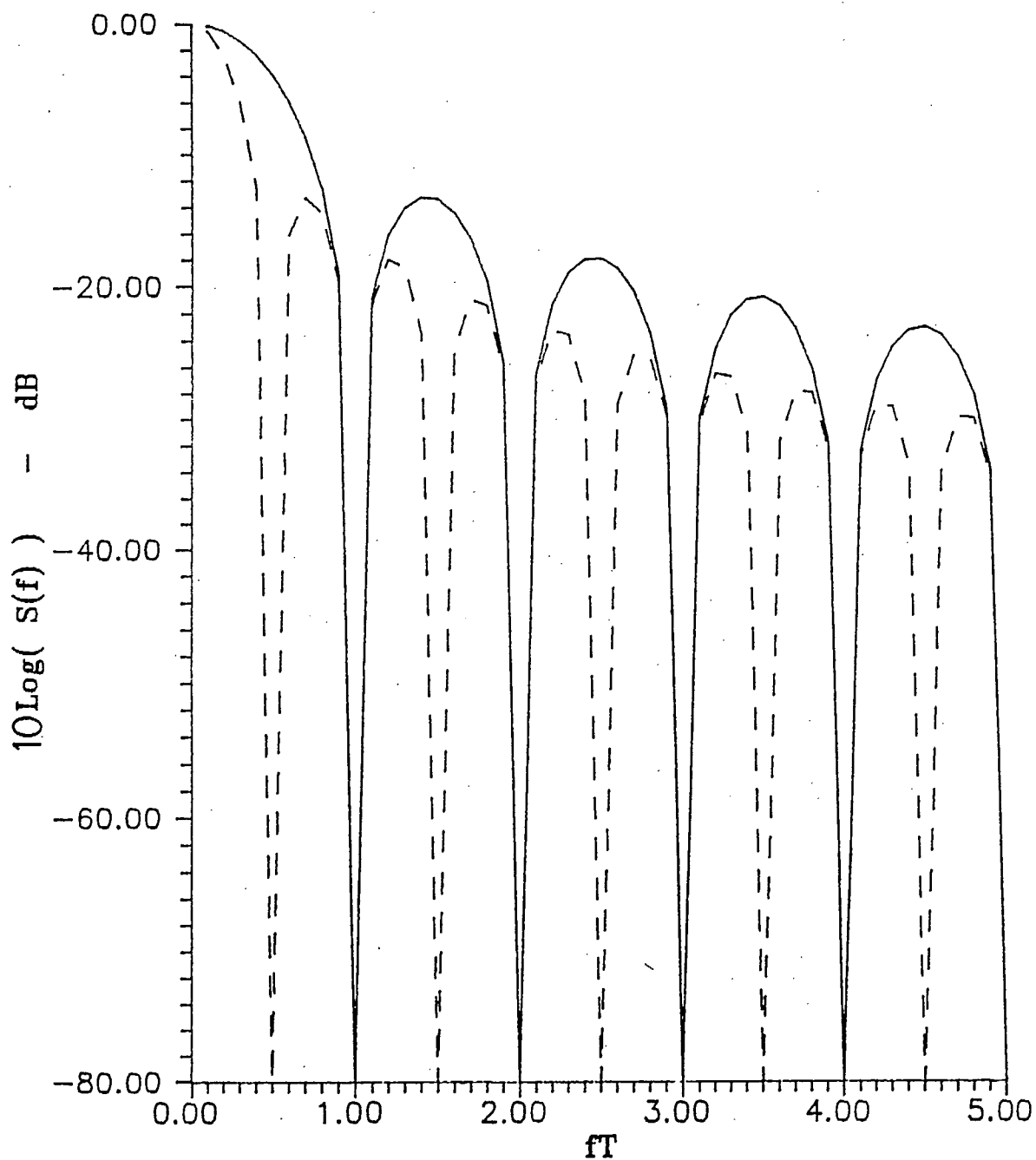
Savings in bandwidth can also be realized by using more spectrally efficient data modulation techniques. There are, in fact, two advantages to using signals with improved spectral concentrations of energy: for a given frequency separation between users there will be less ACI in a multi-user environment, and when the spectrum of each user is truncated, prior to the IFT process, less energy is discarded. In this context, binary and quaternary DPSK are considered. The power spectral densities of these modulating schemes are

$$S(f)_{\text{dbpsk}} = \frac{T \sin^2(\pi f T)}{(\pi f T)^2} \quad (5.3a)$$

$$S(f)_{\text{dqpsk}} = \frac{2T \sin^2(\pi f T)}{(\pi f T)^2} \quad (5.3b)$$

These spectra are illustrated in Figure 5.10 where the bit rate, $1/T_b$, has been fixed: thus T for DQPSK is twice that for DBPSK. By integrating (5.3a) and (5.3b) over the range Δf_u , the fractional in-band power can be calculated. This integration is performed numerically with a quadrature rule algorithm and the results are presented in Figure 5.11. Because DQPSK is more spectrally efficient, a higher fraction of the transmitted power will be contained in the same Δf_u bandwidth than is the case for DBPSK. Also, since the out-of-band power is effectively ACI, DQPSK promises to be less sensitive to interference. Examination of Figure 5.11 indicates that increasing the user bandwidth past $2/T_b$ in either the binary or quaternary case results in only a marginal increase in the fraction of in-band power retained after the spectrum is truncated. This agrees with the results presented in Figure 5.9. For these reasons, subsequent analysis, for both binary and quaternary DPSK, will continue to assume an FDMA user separation of $2/T_b$ and a user bandwidth of $\Delta f_u = 2/T_b$.

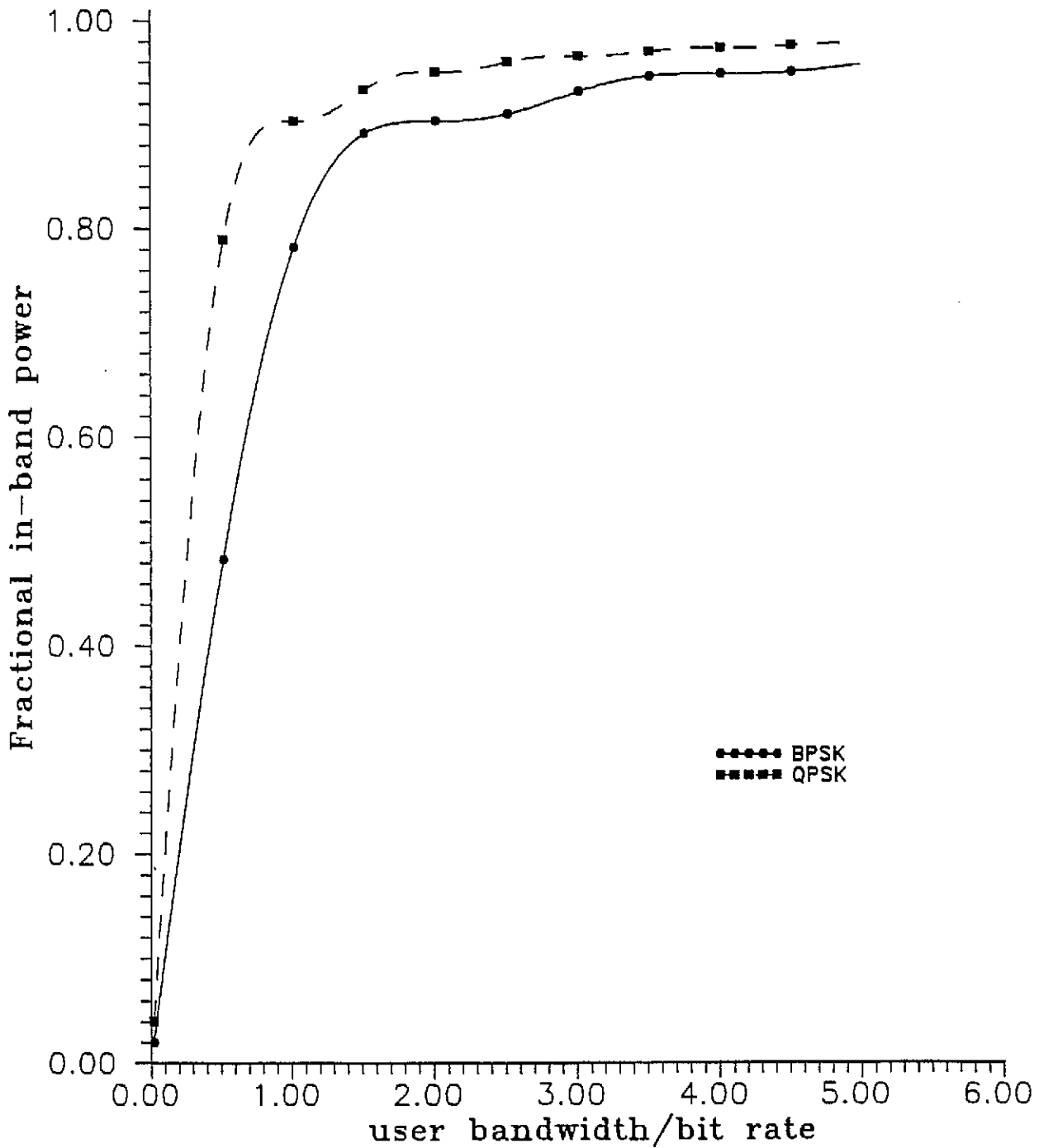
Figure 5.10 Power spectral densities of Quaternary and Binary DPSK



Spectral density of BPSK and QPSK.

— BPSK
- - QPSK

Figure 5.11 Fractional In-band Power of Quaternary and Binary DPSK



Fractional in-band power for BPSK and QPSK

5.4 Varying TB product SAW Device Considerations

Some published results ([10], [25]) indicate a direct correspondance between N_w , the number of points in a DFT and the TB product of SAW devices used in a SAW-based FFT processor of comparable resolution. This effect is due to the finite duration of the sampling interval. Because each frequency component is spread over a nominal frequency range of $\frac{1}{T_H}$, the number of resolvable frequencies becomes $BT_H = TB$. This result implies that, given a fixed hop period, an increased TB product will not increase the frequency resolution of the processor, but will increase the bandwidth that can be analysed. The FFT processor has a sampling interval of T_H while the IFT processor analyses a signal of time duration $\Delta f_u/\mu$. Thus the resolution of the demodulator is dictated by the TB product of the SAW devices used in the FFT processor. To account for this device parameter, the number of points used in the standard FFT algorithm is varied over a suitable range of values. Specifically, simulations are performed for cases where $N_w = 512, 1024, \text{ and } 2048$. Table 5.1 lists the relationships between N_w and the equivalent SAW processor parameters.

Table 5.1 DFT/SAW processor parameters

N_w	T_H μsec	B_{IF} MHz	Max. # of DPSK users
2048	50	40.96	12
1024	50	20.48	6
512	50	10.24	3

Having defined specific processor bandwidths, it is necessary to accurately reflect the fraction of this bandwidth allocated to each user, so it is necessary to modify the data rate used in the previous simulations. A symbol rate of 80 symbols/hop for DBPSK and 40 symbols/hop for DQPSK corresponds to a data rate of 1.6 Mbps. These symbol rates are convenient to implement in the DFT, and provide a close approximation to the T1 data rate desired. This implies that the allocated user bandwidth becomes $\Delta f_u = (2/T_b) = 3.2$ MHz. Immediately it can be concluded that the SAW processor with $T_b = 512$ is capable of handling only 3 DPSK users under these conditions (leaving 0.64 MHz of bandwidth for LDR processing). Note that the user bandwidth of 3.2 MHz is maintained in the quaternary case as well, so the DQPSK capacity is the same. Maintaining the same FSK/DPSK bandwidth allocations (η , as defined in section 2.1, is a constant), the user capacities given in Table 5.1 are the result.

Following the previously established procedures, a waveform analysis is performed. Figure 5.12 illustrates the

Figure 5.12
Modified Sample Input Sequence

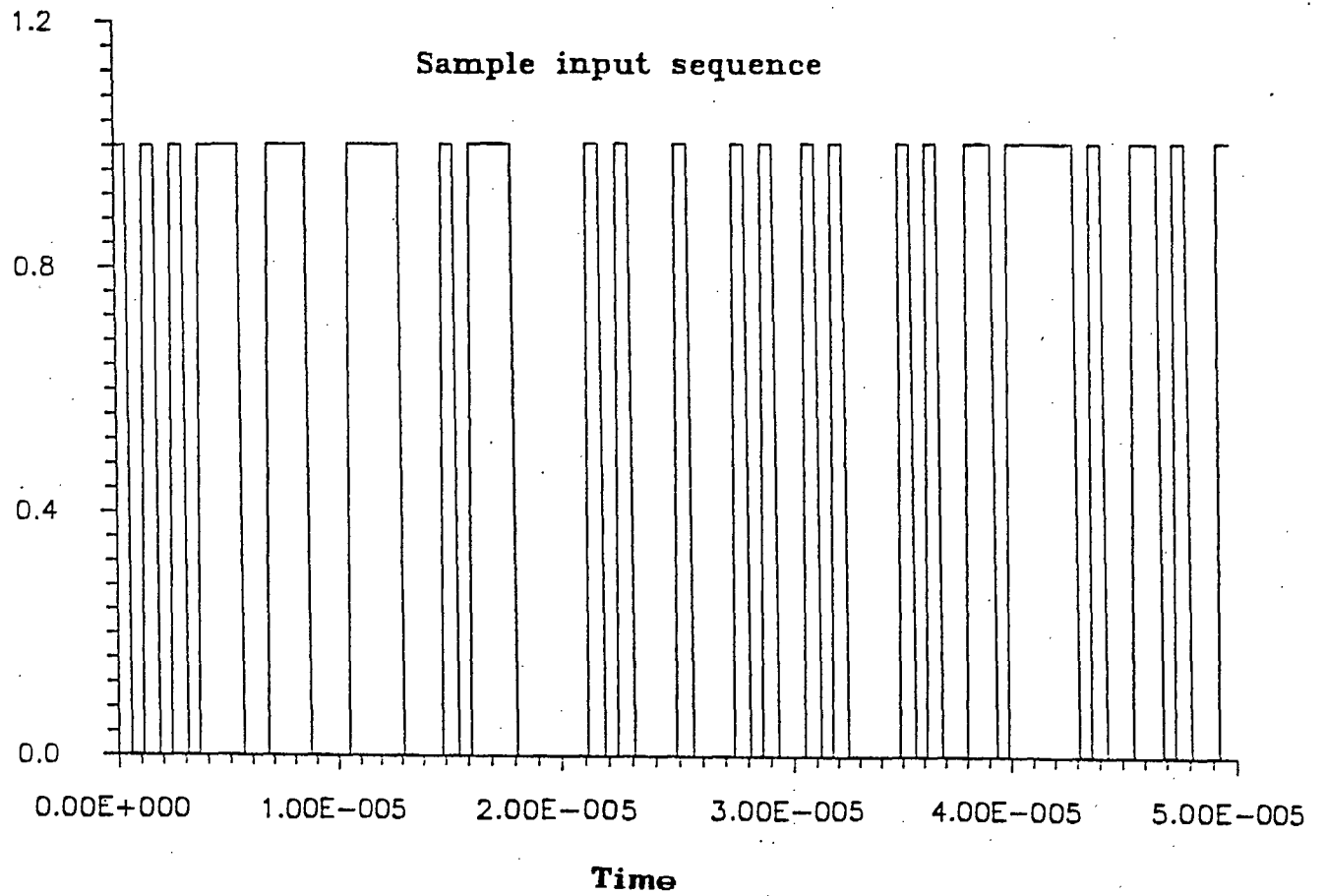
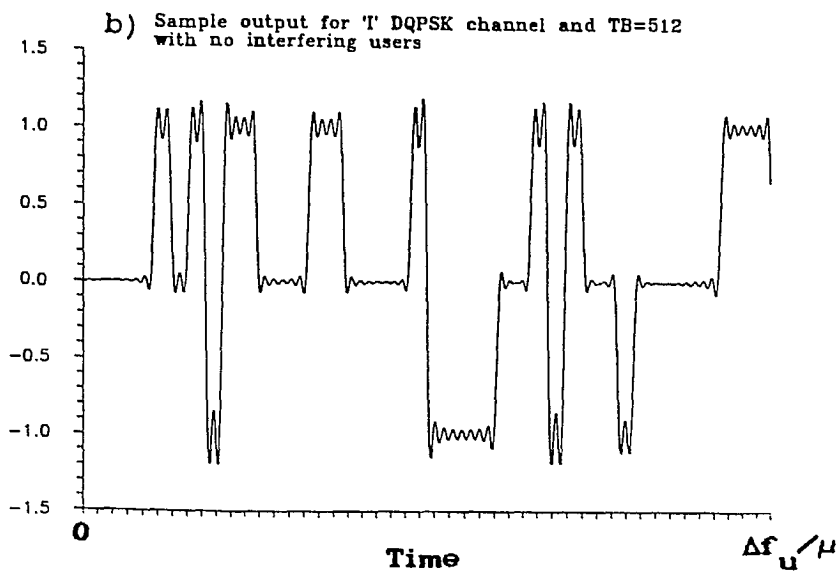
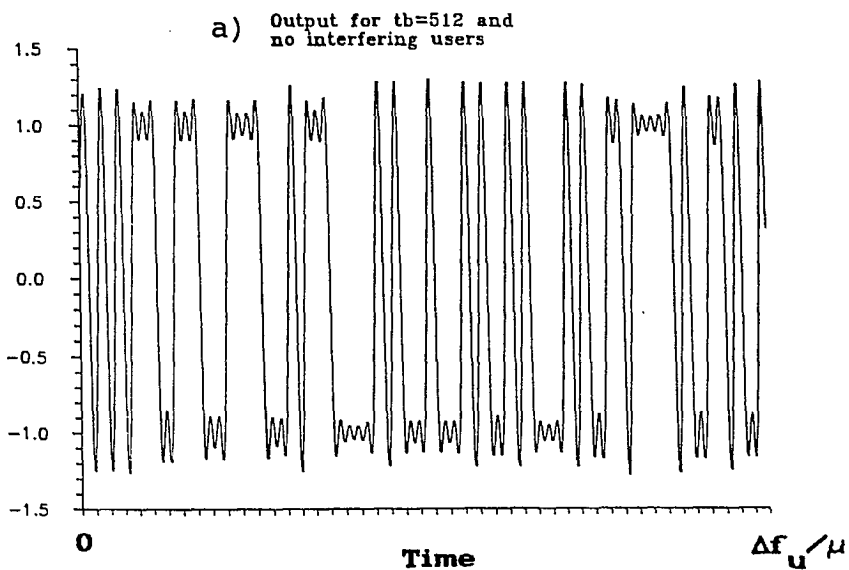


Figure 5.13

Sample output with TB = 512



modified sample input sequence used. The resulting baseband output is given in Figure 5.13 for $TB = 512$. Figure 5.13a illustrates the DBPSK output waveform and 5.13b gives the same output in the quaternary case. It should be noted in Figure 5.13b and in subsequent quaternary waveforms, that the illustrated output shows only the in phase or "I" arm output of the demodulator where the phase transitions can be $\pm\pi$. The quadrature or "Q" output, where transitions of $\pm\pi/2$ would appear, is not shown. Figures 5.14a,b and 5.15a,b give the corresponding results when $TB = 1024$ and $TB = 2048$ respectively. In all of these cases, only the reference user is active. These results do not provide significant insight to the effects of varying TB products for either the binary or quaternary case, except to note that all processors produce equivalent distortion of the waveform output. A BER analysis is performed as outlined in section 4.2 and the results of this analysis are given in Figures 5.16 and 5.17 for the binary and quaternary case, respectively, with comparison to optimum detection capability in each case.

In the binary case there is negligible difference in performance between the processors considered. In the quaternary case, however, the processor with $TB = 512$ performs about 0.8 dB (at a SNR of 10 dB) worse than the other two, which perform equally well. Furthermore, its performance seems to decrease relative to the other processors with increasing SNR.

Figure 5.14

Sample waveform output, TB = 1024

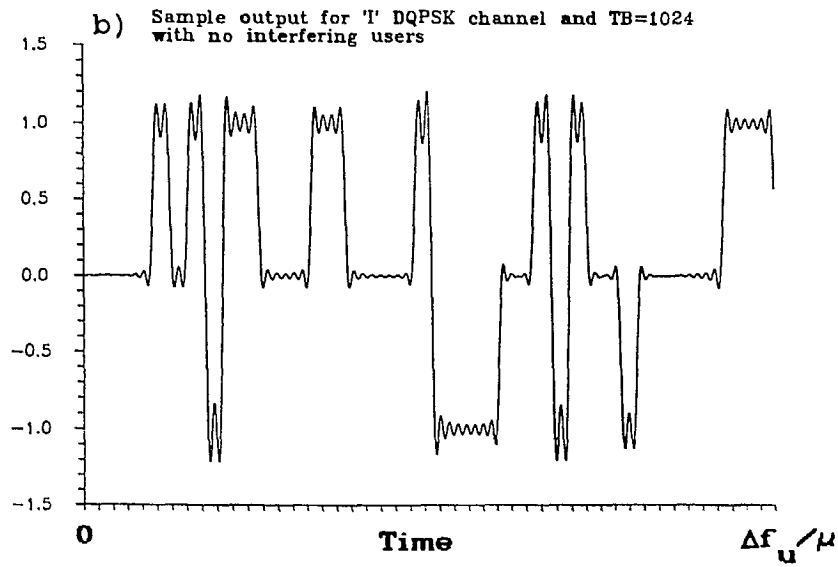
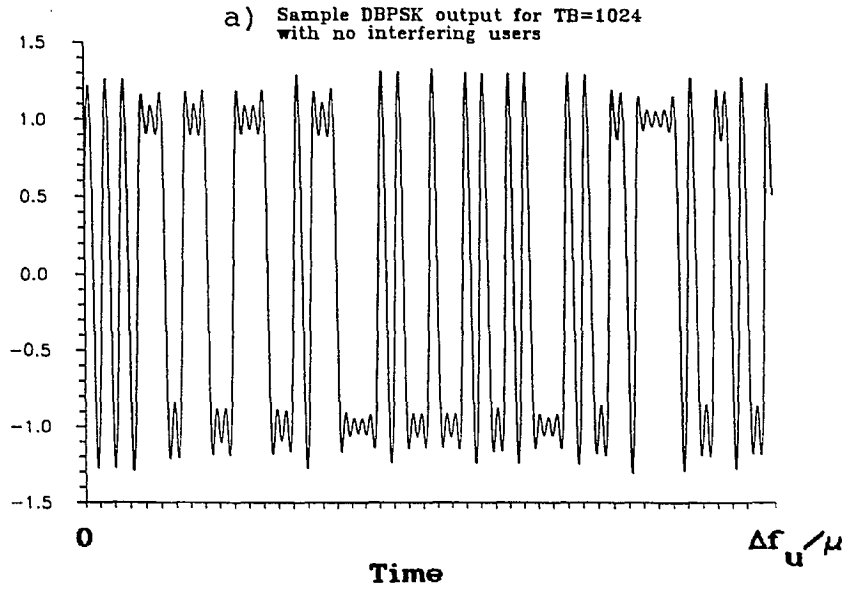


Figure 5.15

Sample waveform outputs, $T_B = 2048$

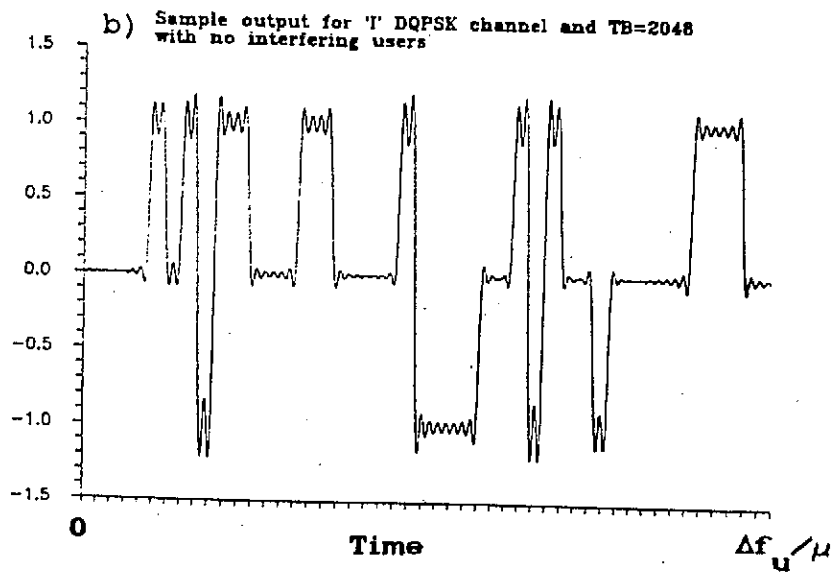
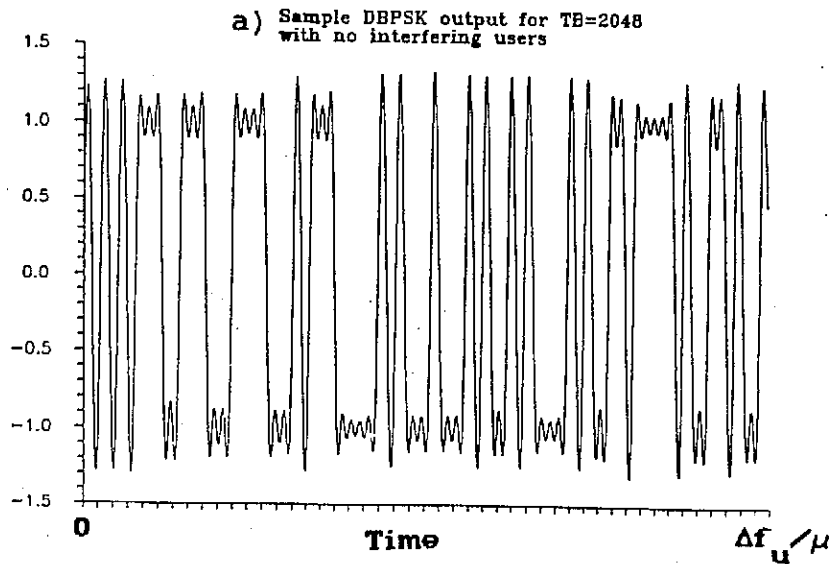
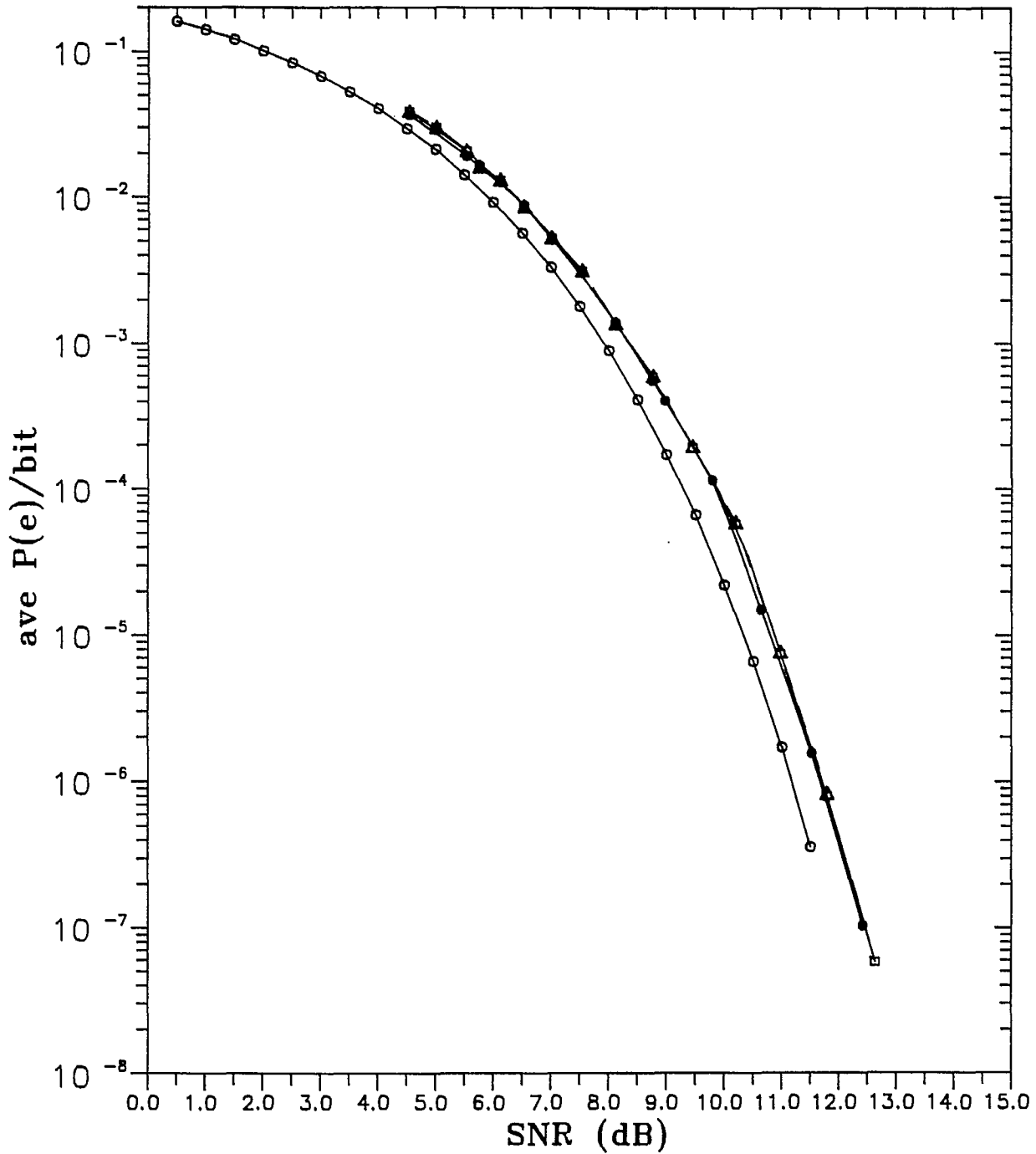


Figure 5.16
BER results for DBPSK

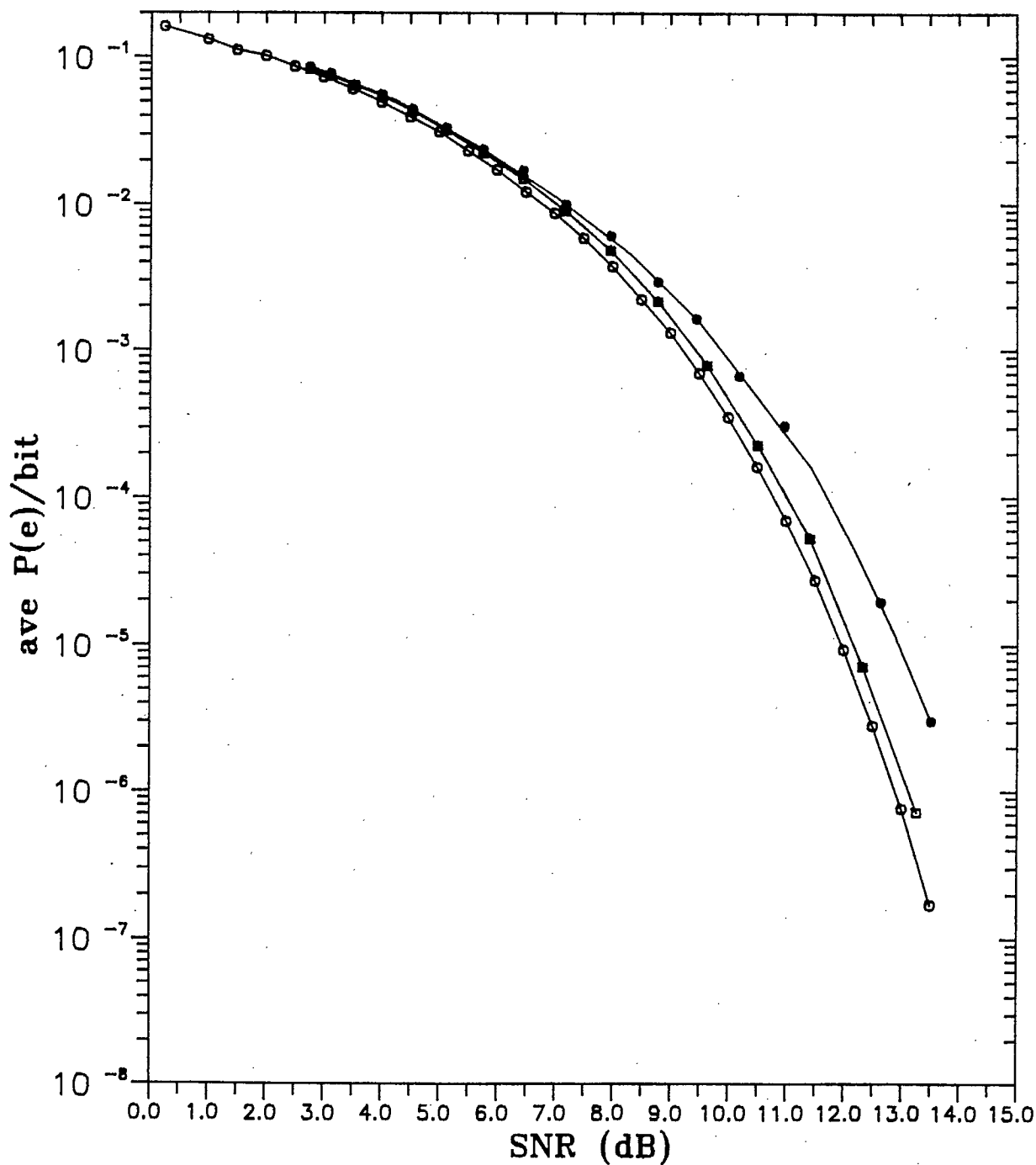


Average P_e /bit for detection of
of DBPSK with varying $N = TB$
and no interference

oooo optimum
●●●● TB = 512
□□□□ TB = 1024
△△△△ TB = 2048

Figure 5.17

BER results for DQPSK



Average P_e /bit for detection of DQPSK with varying $N = TB$ and no interference

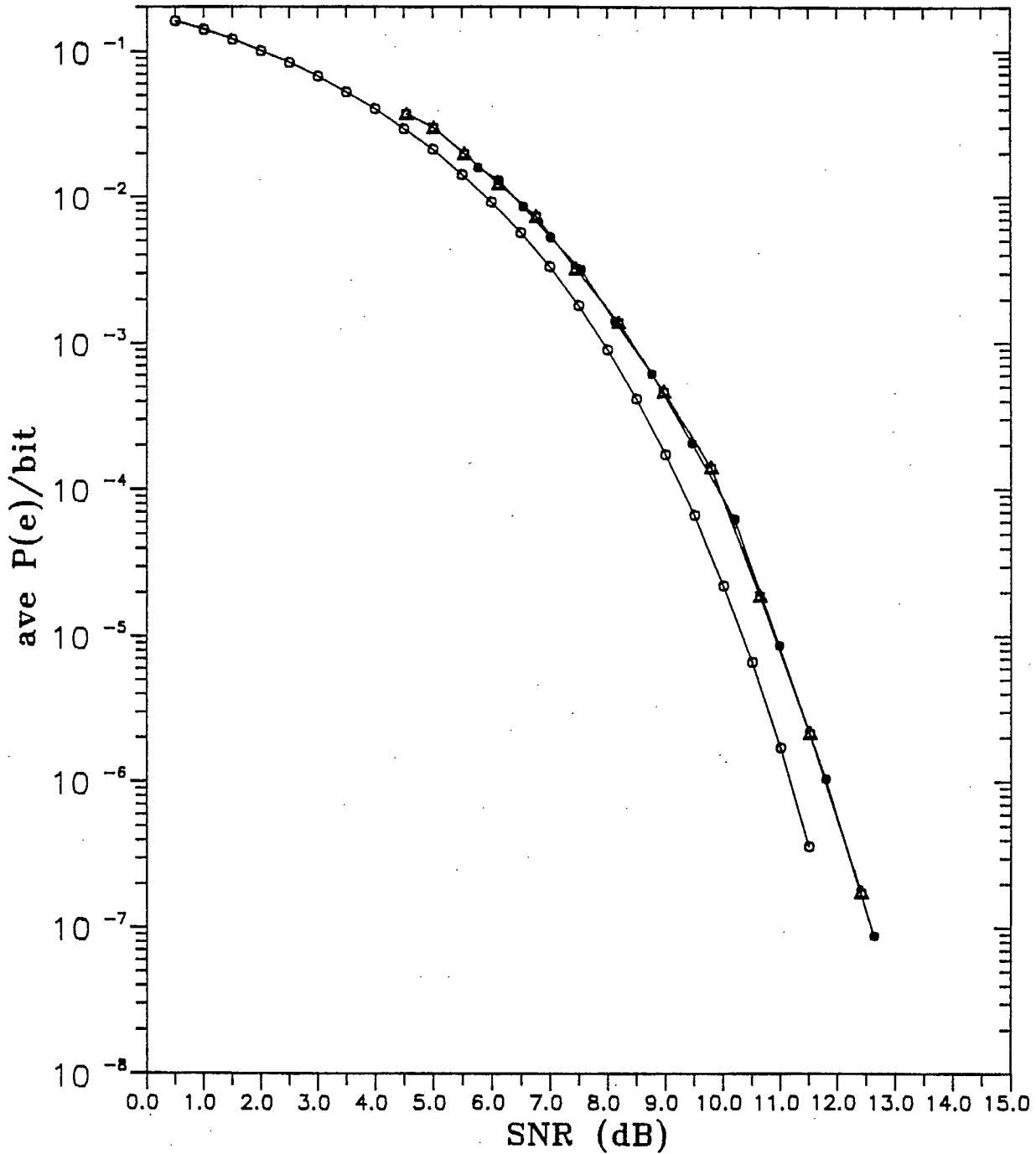
o-o-o-o optimum
●-●-●-●- TB = 512
□-□-□-□- TB = 1024
▲-▲-▲-▲- TB = 2048

BER performance is also considered in the presence of interfering users. Two interfering users are placed at a frequency separation of $2/T_b = 3.2$ MHz from the reference user, that is, the carrier frequency of the interfering users are $f_{cr} \pm 2/T_b$, where f_{cr} is the carrier of the reference user. Initially, both interfering users and the reference user are at equal power. BER results for this case are presented in Figures 5.18 and 5.19 for the binary and quaternary cases respectively. In the binary case, there is virtually no degradation in performance for any of the processors. For the quaternary case, the processor with $TB = 512$ undergoes further performance degradation; making it over 1 dB worse than the larger TB product processors at an SNR of 10 dB. The DQPSK performance of processors with $TB=1024$ and $TB=2048$ are unaffected by this level of interference.

The effect of increasing the interfering user power to 10 dB greater than the reference user is illustrated in Figures 5.20 and 5.21. Note that DBPSK still suffers no performance degradation with this level of interference. Performance is unaffected in the DQPSK case as well.

Figure 5.18

BER results for DBPSK with two interfering users at equal power to the reference user

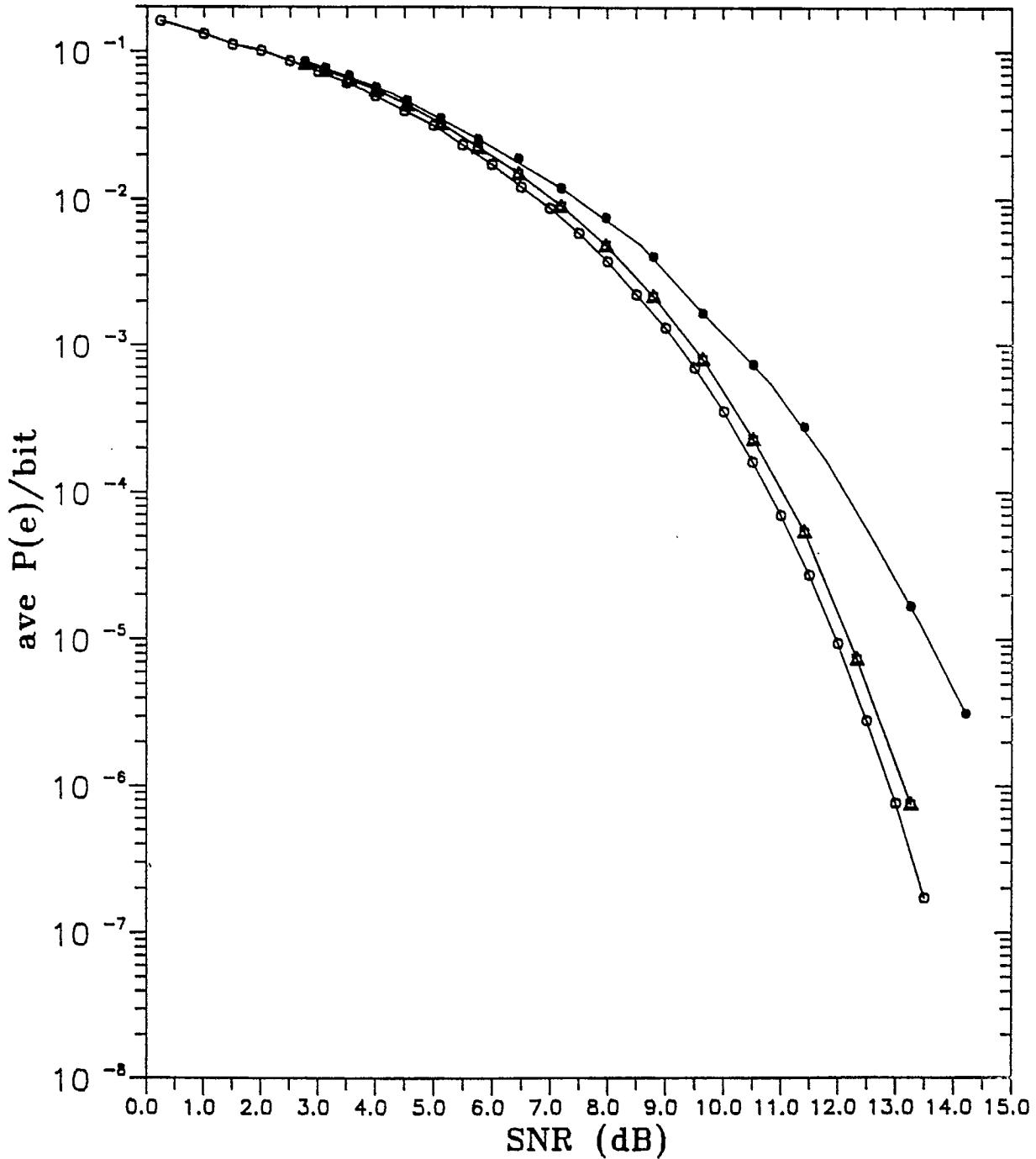


Average P./bit for detection of
of DBPSK with varying N = TB
and two interfering users
at equal power

oooo optimum
●●●● TB = 512
□□□□ TB = 1024
▲▲▲▲ TB = 2048

Figure 5.19

BER results for DQPSK with two interfering users at equal power to the reference user

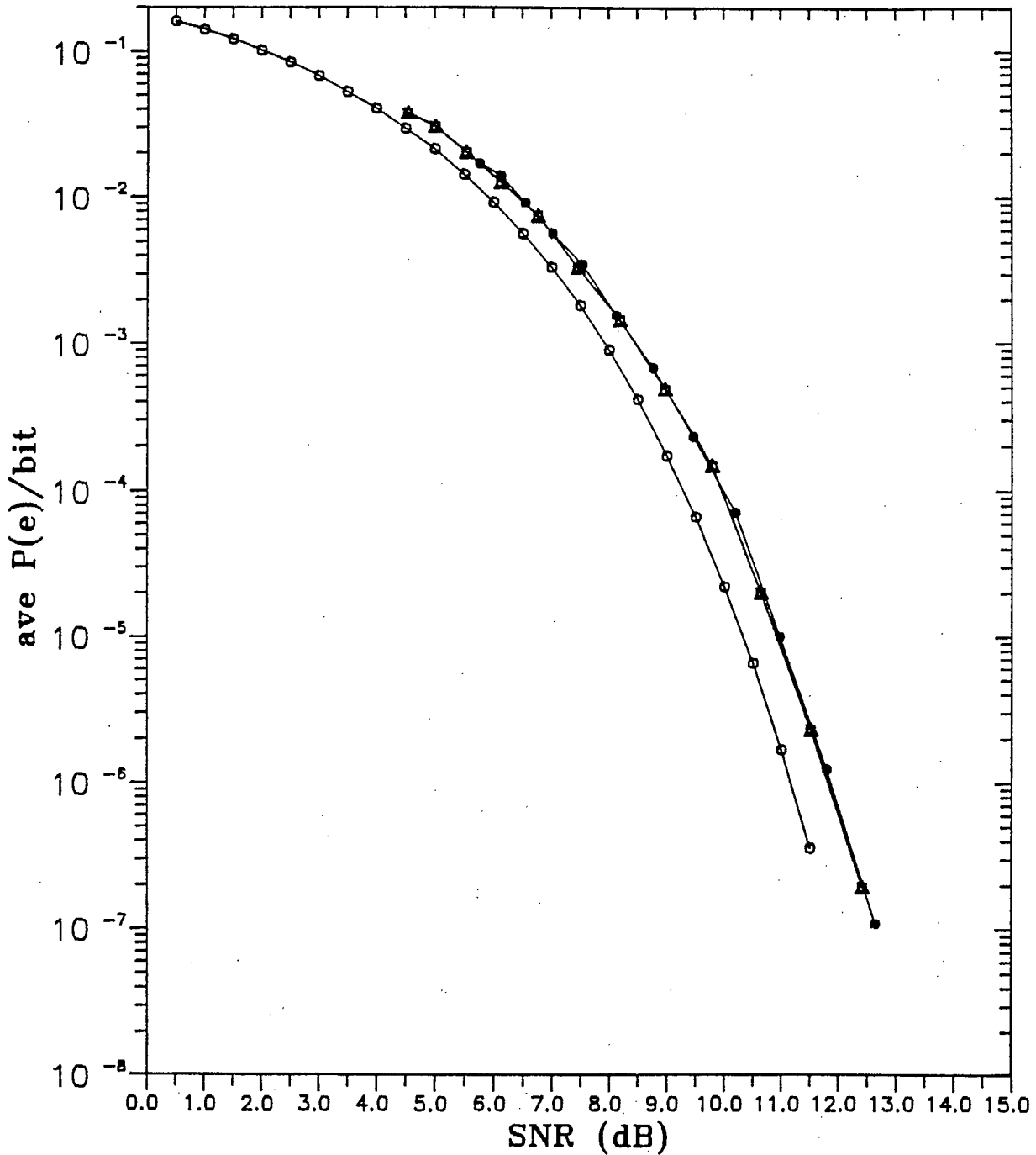


Average P_e /bit for detection of DQPSK with varying $N = TB$ and with two interfering users at equal power.

o-o-o-o optimum
●-●-●-● TB = 512
□-□-□-□ TB = 1024
△-△-△-△ TB = 2048

Figure 5.20

BER results for DBPSK with two interfering users at 10 dB greater power than the reference user

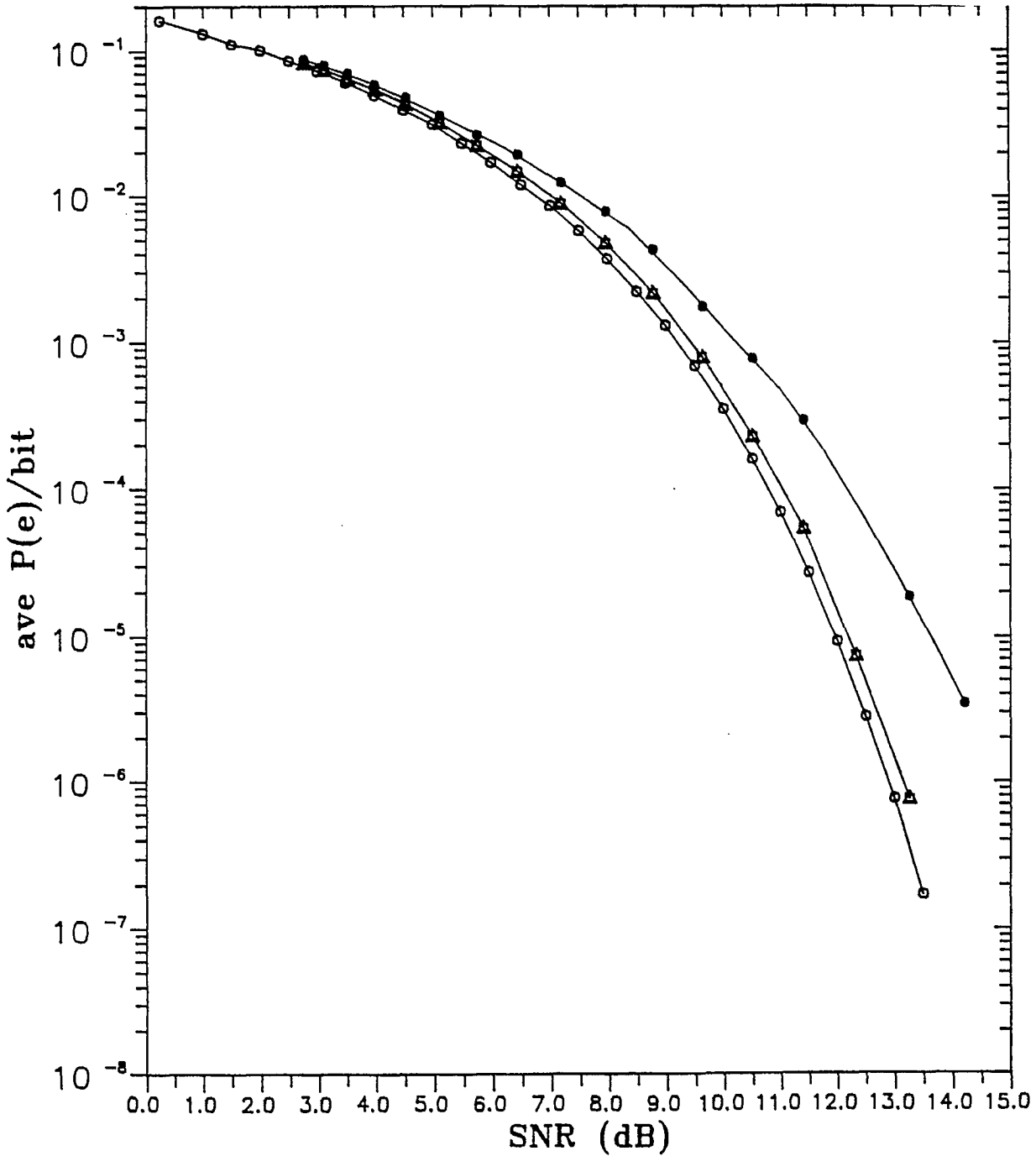


Average P_e /bit for detection of DBPSK with varying $N = TB$ and two interfering users each at 10 dB greater power than the reference user

o-o-o-o optimum
●-●-●-● TB = 512
□-□-□-□ TB = 1024
△-△-△-△ TB = 2048

Figure 5.21

BER results for DQPSK with two interfering users at
10 dB greater power than the reference user



Average P_e /bit for detection of
of DQPSK with varying $N = TB$
and with two interfering
each at 10 dB greater power
than the reference user

o-o-o-o optimum
●-●-●-●- TB = 512
□-□-□-□- TB = 1024
△-△-△-△- TB = 2048

The results in this section indicate that there are fundamentally two sources of performance degradation. The first is distortion of the pulses due to the processing and interference. The second is the limited resolution of the transform. In the binary case, all the processors considered seem to provide adequate transform resolution. The binary case also seems robust in the presence of interfering users. The quaternary case seem more sensitive to the resolution of the transform, resulting in a performance degradation for the TB=512 case. In cases where higher resolution of the transform is provided ,the quaternary case also seems rather insensitive to interference.

In summary, it can be stated that DBPSK consistently outperforms DQPSK by 1 to 2 dB at a data rate of 1.6 Mbps, and its performance is relatively invariant to ACI and the TB product of the SAW processor. When DQPSK modulation is used, processor performance is reduced for TB = 512 compared to larger TB values. This condition is slightly worsened in the presence of interfering users. As in the binary case, DQPSK processors with TB = 1024 and TB = 2048 perform equally well under the interference conditions presented.

5.5 Non-linear Phase and Amplitude Response

In the simulations performed, it has been implicitly assumed that the SAW processors studied are capable of maintaining a linear phase and flat amplitude response to the same degree of accuracy as the DFT algorithm. For practical SAW implementations, however, amplitude and phase non-linearities will be present, as are evident in the SAW device tests presented in [9].

Phase ripple in a SAW device is due to effects which influence the propagation velocity of the surface acoustic wave. Some of these effects are described in Appendix A; they include changes in SAW velocity resulting from deposition of metallized electrodes and imperfections in the piezoelectric crystal substrate. Other velocity altering effects include temperature variations across the device and strain forces resulting from mounting the crystal substrate.

It is assumed here that the net result of the phase non-linearities of each of the SAW devices used in the demodulator sum together randomly and the deviation from a linear response can be modelled as a uniformly distributed random function, a characteristic which agrees well with the device results presented in [8] and [9]. Two values of the peak to peak phase ripple are considered. As was illustrated in Figure 3.4, there are a total of 6 SAW-based operations

in the FT/IFT processing of DPSK symbols: a C-M-C processor followed by another C-M-C processor. A random peak to peak phase fluctuation of 2.5° on each device results in a net processor phase ripple of 15° p-p. If the SAW devices are manufactured to a tolerance of 5° p-p, the net processor phase fluxuation becomes 30° p-p. Both values of processor phase fluxuation are considered in the following analysis.

Amplitude ripple in each of the SAW devices can be caused by many of the same phenomena which result in phase non-linearities; however, two other sources must also be considered. Triple transit echo (TTE) is the result of a surface acoustic wave being internally reflected at the substrate boundaries and this echo contributing to the transducer output. Normally, this effect is minimized by bonding an acoustically absorbent material to the crystal edges, but for wide bandwidth devices it is difficult to remove completely. Another effect to consider is the amplitude ripple caused as a result of the time limited FM burst of the SAW device impulse response. Conventionally, this ripple is reduced by using amplitude tapers; however, in this case it has been demonstrated that these tapers should not be used in the DPSK transform. It is assumed, because of this, that the amplitude response of the demodulator is dominated by this effect. It is also assumed that this response is dominated by the amplitude characteristics of the SAW device which would otherwise

provide a windowing function, namely, the second convolution (compressor) filter in the C-M-C FT processor shown in Figure 3.4 . Thus, the net amplitude response of the demodulator is modeled strictly as the Fourier transform of the impulse response of the second convolution filter in the FT processor. These non-linear characteristics are incorporated into the DFT simulation by including an error filter with response

$$H_e(f) = A(f)e^{j\Phi(f)} \quad (5.4)$$

where $A(f)$ is the amplitude ripple of the IFT compressor.

and

$\Phi(f)$ is a uniformly distributed random phase fluctuation.

By incorporating this error filter response between the FT and IFT operations in the DFT simulation, frequency domain multiplication can be used. This modified processor model is shown in Figure 5.22. The phase ripple and amplitude ripple for the TB=512 and TB=1024 processor are illustrated in Figures 5.23 and 5.24 respectively. Since the performance of the TB=1024 and TB=2048 processors proved to be identical in the previous section, only the TB=1024 and TB=512 processors are considered in this analysis.

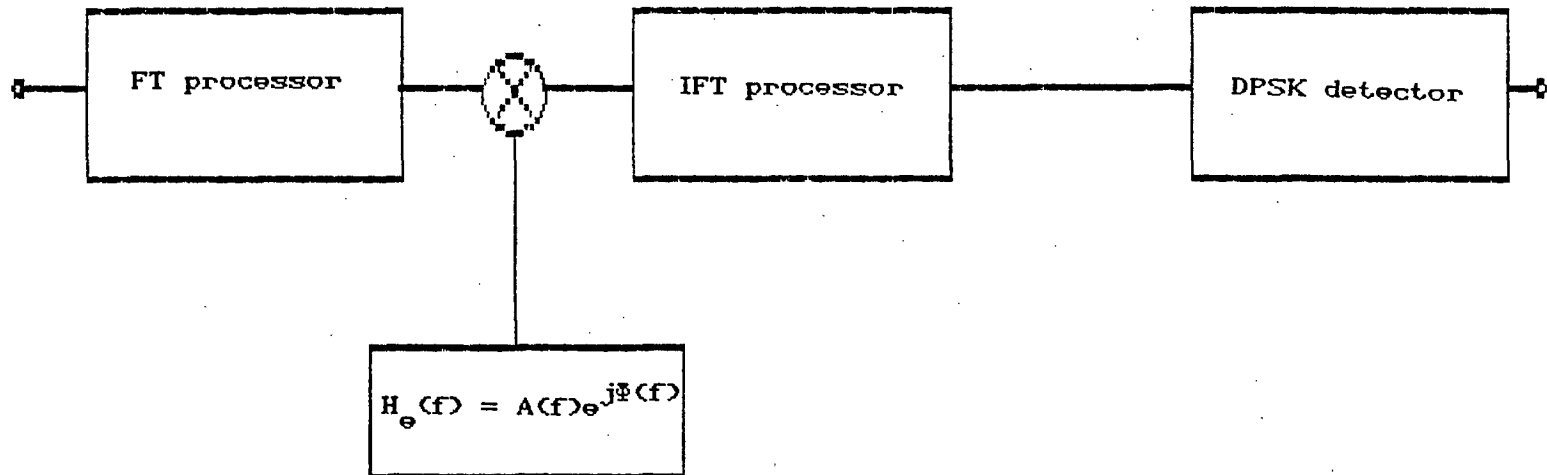


Figure 5.22 Modified Processor Model

The amplitude and phase characteristics (for a 30° p-p phase deviation) used in $H_e(f)$ are shown for the TB=512 and TB=1024 processors in Figures 5.23 and 5.24. Again, analysis starts with the examination of sample output waveforms. In this case, waveforms are presented only for the TB=512 processor, and the varying effect of the non-linearities is examined.

Figure 5.25 illustrates sample outputs for the binary and quaternary case where only the amplitude ripple is considered ($\phi(f) = 0$). Note that in this case neither waveform is significantly more distorted than in the ideal processor conditions. This is particularly significant since it is assumed that the reference user is situated at the center of the passband, where the amplitude ripple is most severe. Figure 5.26 shows the simulated waveforms when $\phi(f)$ has a maximum fluctuation of 15° p-p for both the binary and quaternary case, and Figure 5.27 shows similar results when $\phi(f)$ is 30° p-p. These waveforms indicate that neither phase ripple produces catastrophic distortion of the output waveforms. Because of this, it was decided to perform a BER analysis with the less restrictive phase tolerance of 30° p-p. The results of this analysis are presented in Figure 5.28 for the binary case.

From Figure 5.28, the phase and amplitude non-linearities degrade performance by about 1 dB for the TB=512 processor with SNRs greater than 6 dB. For the

Figure 5.23 Amplitude and Phase non-linearities for the demodulator with $TB = 512$

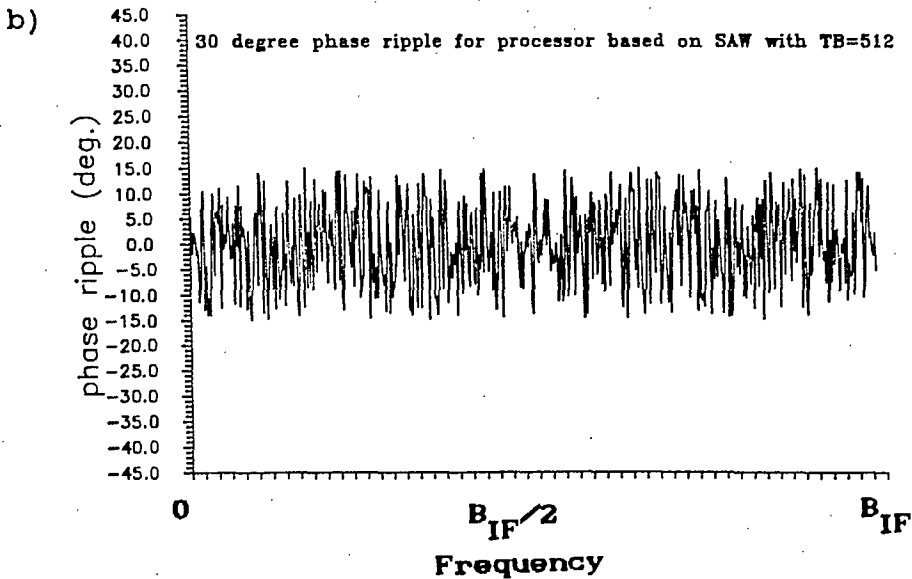
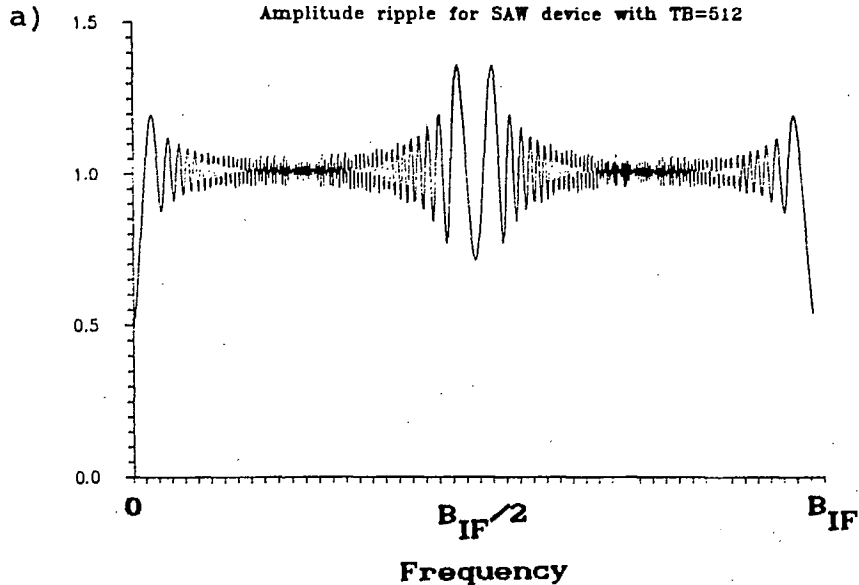


Figure 5.24 Amplitude and Phase non-linearities for the demodulator with TB = 1024

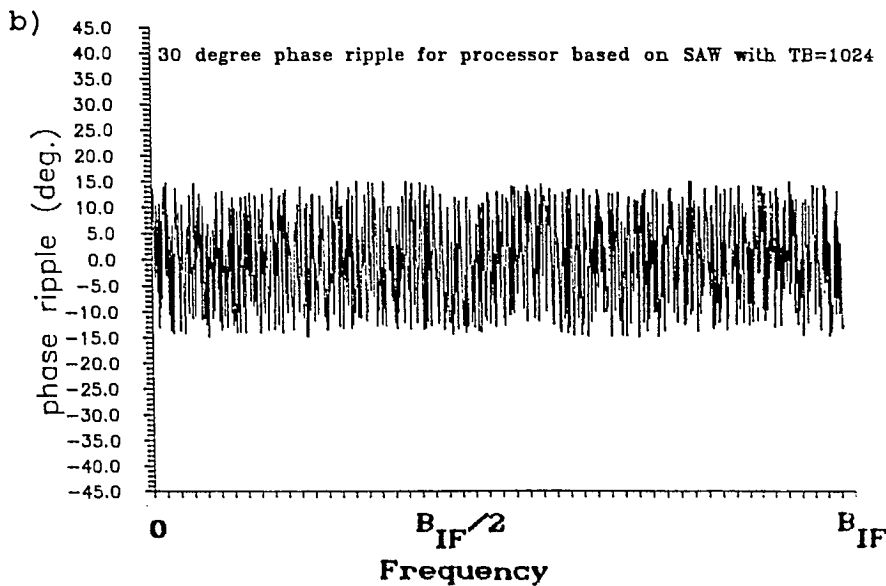
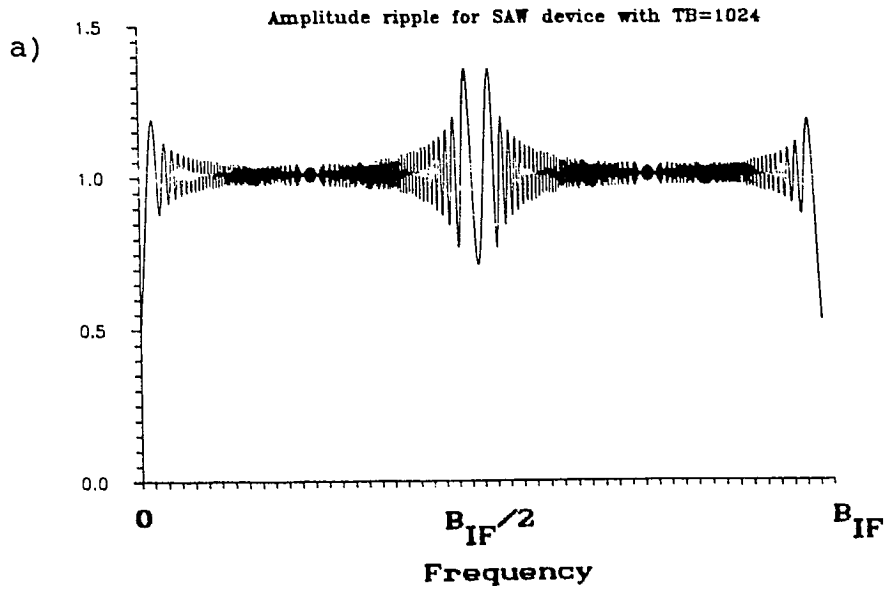


Figure 5.25 Sample Waveform Output with $\Phi(f) = 0$

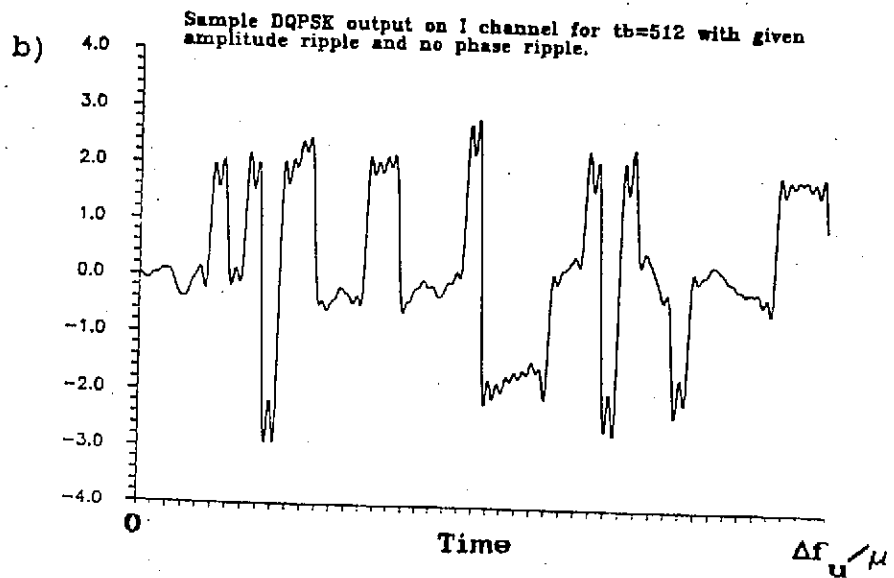
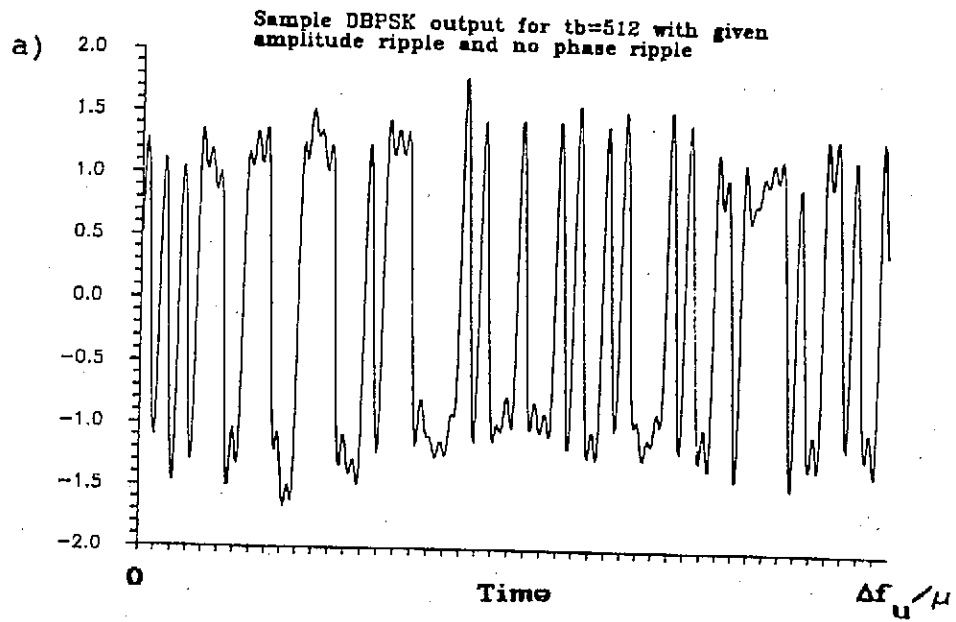


Figure 5.26 Sample Waveform Output with $\Phi(f) = 15$ p-p

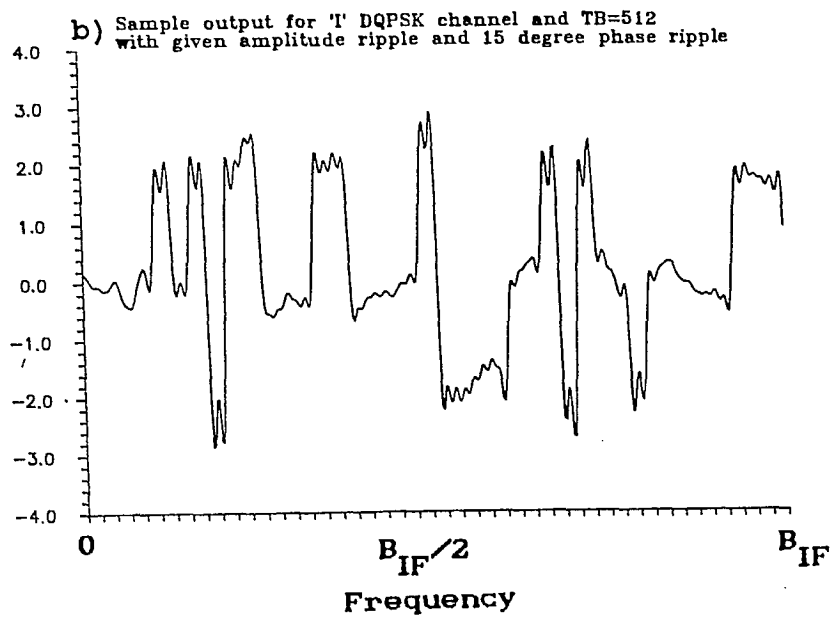
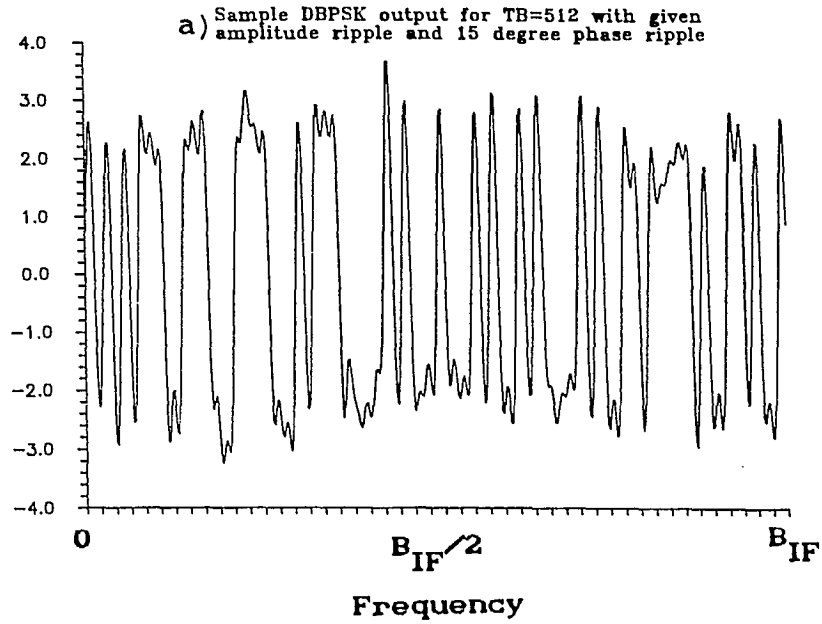


Figure 5.27 Sample Waveform Output with $\phi(f) = 30$ p-p

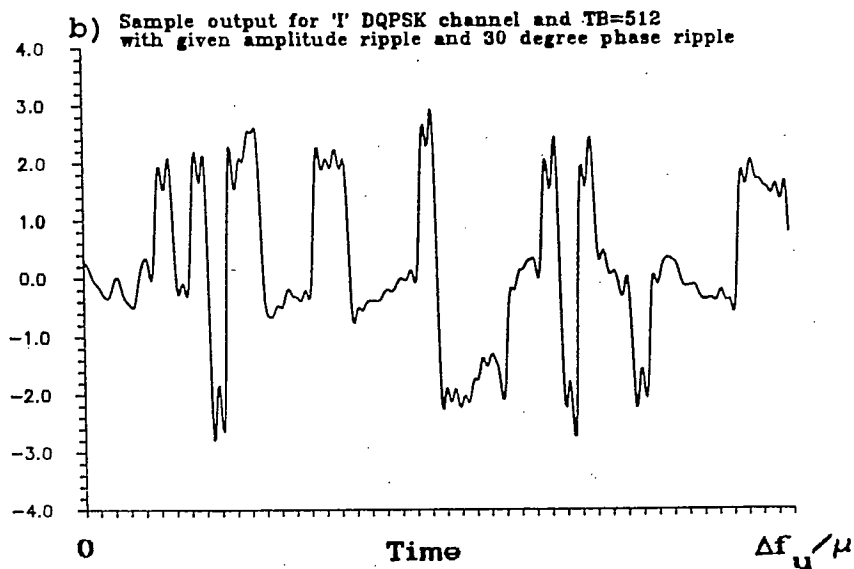
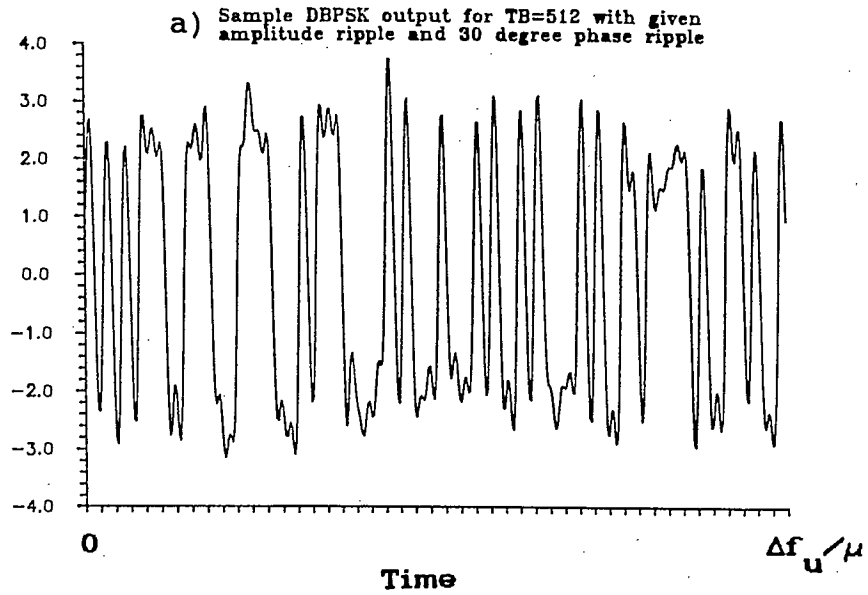
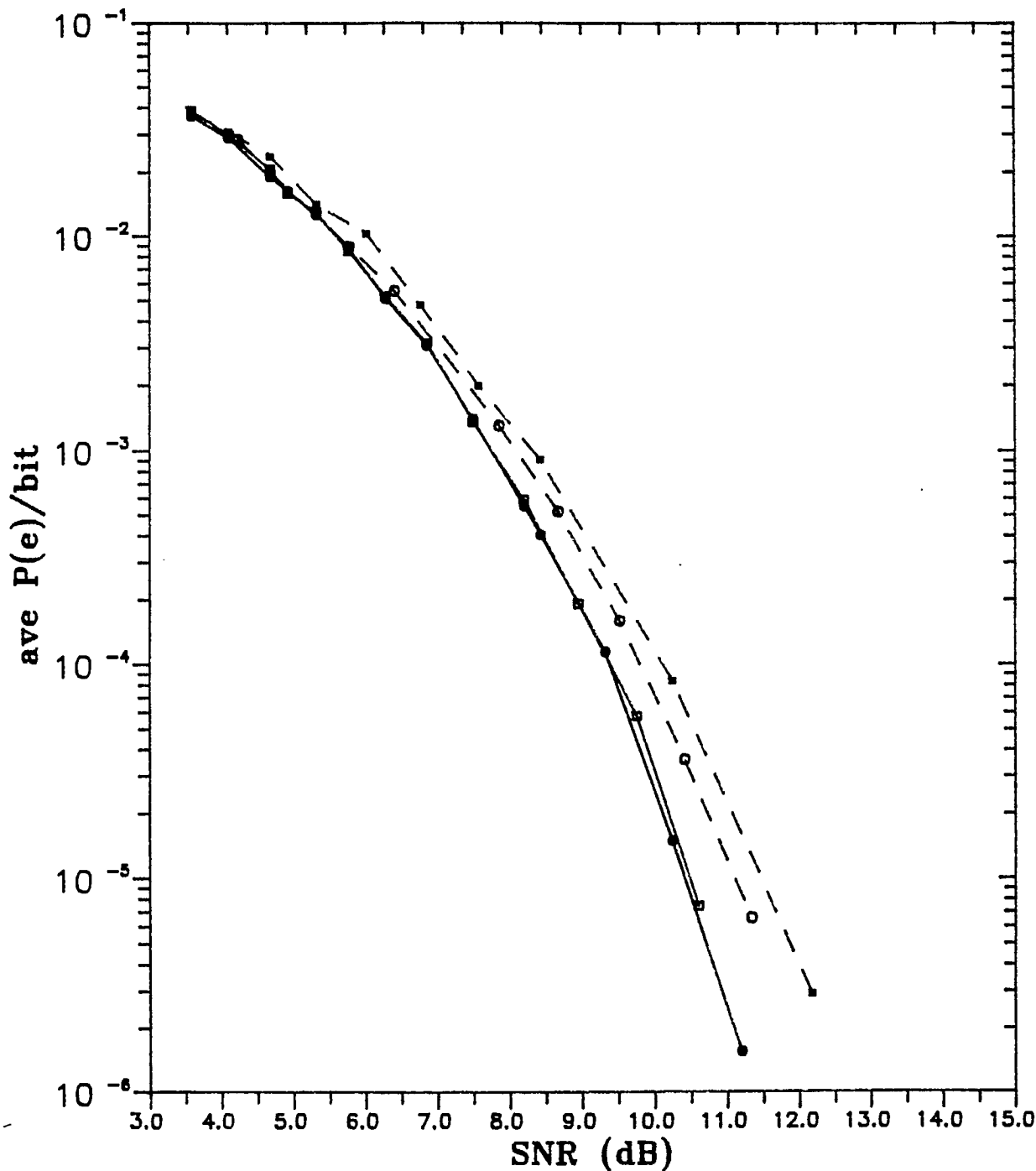


Figure 5.28 BER results for Binary DPSK

with processor incorporating phase and amplitude ripples



Average P_e/bit for processor with amplitude and phase ripple, using DBPSK signalling

○○○○ TB=512, with ripple
 ●●●● TB=512, without ripple
 □□□□ TB=1024, with ripple
 ■■■■ TB=1024, without ripple

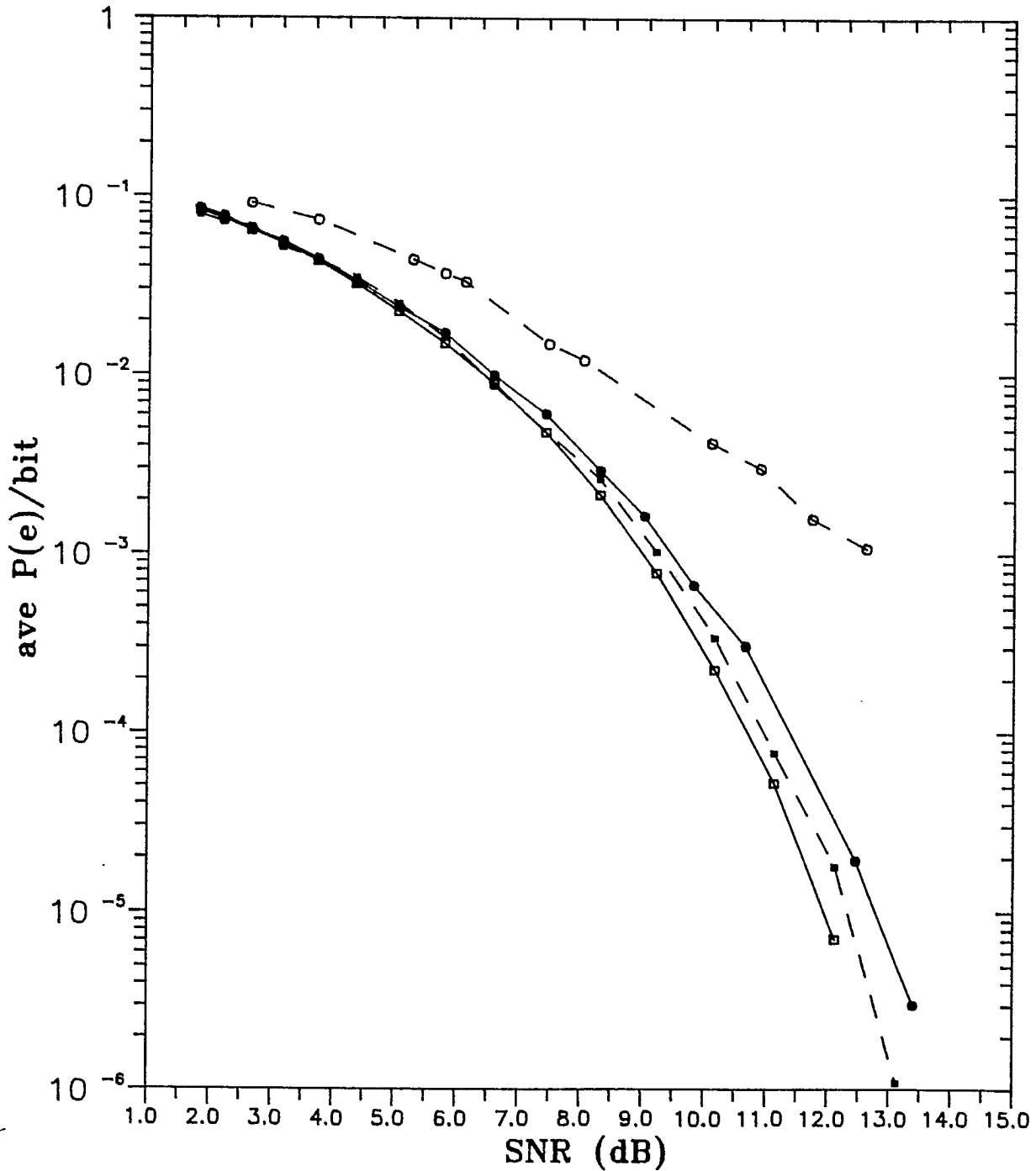
TB=1024 processor, performance is degraded by about 1.2 dB for similar SNRs. As indicated, this results in slightly superior performance from the TB=512 processor.

Figure 5.29 gives the BER results for the quaternary case where non-linear phase and amplitude effects are present. These results indicate a 0.5 dB degradation in performance for the TB=1024 processor. For the TB=512 processor, the presence of the non-linearities seems to exaggerate the relative loss that was noted in the previous section. In this case, the performance degradation is about 3 dB for a P_{be} of 10^{-2} and continues to worsen with larger SNR. These results indicate that the TB=1024 processor offers superior performance in this case.

The results in this section indicate that the effect of incorporating the non-linearities into the transform is a loss in transform accuracy. For the binary case, this loss is only noticeable when TB=512. In the quaternary case, both TB=512 and TB=1024 processors suffer noticeable performance degradation, which agrees with the higher transform sensitivity of DQPSK commented on in the previous section. For the TB=512 case, this loss in transform accuracy translates into a drastic degradation in performance.

To summarize the results of this section, the presence of the non-linear effects results in a performance degradation in all cases. For the binary case, this degradation is about 1 dB for TB=512 and 1.2 dB for TB=1024.

Figure 5.29 BER results for Quaternary DPSK
with processor incorporating phase and amplitude ripples



Average P_e /bit for processor with
amplitude and phase ripple using
DQPSK signalling

○-○-○-○ TB=512, with ripple
●-●-●-● TB=512, without ripple
- - - - - TB=1024, with ripple
□-□-□-□ TB=1024, without ripple

When quaternary signalling is considered, the TB=1024 processor suffers a degradation of about 0.5 dB. For the TB=512 processor, performance is significantly degraded. A condition which worsens with higher SNR values.

Chapter 6

6.1 Conclusions:

The results presented here indicate that group demodulation of DPSK at 1.6 Mbps can be performed using the Fourier transform/Inverse Fourier transform processor proposed, as part of a joint FSK/DPSK group demodulator, given by Felstead in [3]. The intended use of such an application is the Canadian EHF SatCom system.

It has been shown that the FT/IFT processor can be realized using the Chirp Fourier transform algorithm and implemented with surface acoustic wave devices. For this implementation, the convolve-multiply-convolve (CMC) arrangement of SAW devices provides 100% duty cycle operation and the necessary capability to implement separate windowing functions for the DPSK and FSK users.

Unlike FH-FSK, the optimum window for group demodulation of DPSK, as it is performed here, is the rectangular window. All other windows result in an SNR degradation with no reduction in adjacent channel interference.

Processor performance is considered for the cases where its time-bandwidth product is $TB=512$, $TB=1024$, and $TB=2048$ with no phase or amplitude non-linearities present from the

SAW devices. For this analysis it is assumed the signal is perturbed by narrow-band Gaussian noise. A user-bandwidth of $2/T_b$ is shown to provide satisfactory performance for both binary and quaternary DPSK users. This bandwidth allocation results in a maximum DPSK group demodulation capacity of 3 users for the TB=512 processor. Maintaining the same bandwidth parameters, the processor with TB=1024 has a maximum capacity of 6 users, and a processor with TB=2048 is capable of group demodulation of up to 12 DPSK users.

Under these conditions it is found that the three processors demodulate binary DPSK equally well, and this performance is relatively immune to interference from adjacent users. Under the same conditions, but using quaternary DPSK, the processor with TB=512 suffers a performance degradation of about 0.8 dB compared to the TB=1024 and TB=2048 processors, which perform equally well.

The performance with processors using time bandwidth products of TB=512 and TB=1024 is considered when non-linear amplitude and phase effects of SAW devices are incorporated into the simulation. For binary DPSK, the TB=512 processor suffers a performance degradation of about 1 dB due to these non-linearities; when TB=1024, the performance degradation is about 1.2 dB. In the quaternary DPSK case, the TB=512 processor suffers large performance degradation. This degradation, relative to the processor without non-linearities, is about 3 dB for an average bit error rate

of 10^{-2} , and worsens for larger SNR values. The TB=1024 processor loses about 0.5 dB under the same conditions.

6.2 Suggestions for Future Work

This report has focused on the performance of the DPSK processing of the joint demodulator. FSK detection should be incorporated into further studies to thoroughly investigate this joint demodulator concept.

It has been assumed that dehopping and transform timing is perfect. A complete analysis should also include effects such as imperfect synchronization of the dehopper and timing offsets in the FT/IFT processor.

Construction of a proto-type of this demodulator, based on commercially available SAW devices, would provide experimental confirmation of these results. Furthermore, a "mock up" demodulator would demonstrate the effects such as insertion loss and external loading in the SAW devices which have not been considered here.

References

- [1] DSS file 06ST.36001-4-1868. Com Dev Report "Spacecraft Signal Processor Breadboard Unit, Final Report". 1986
- [2] P.J. McLane, "Performance of Windowed Reception for D-QPSK in Multi-User Systems", Report, DSS Contract OST85-00190, April 2, 1986.
- [3] E.B. Felstead, "Synchronization and Processing of Uplink Higher Data Rate Signals for Canadian EHF Milsatcom Concept". Private Communication, 1987.
- [4] D.R. McElroy, C.W. Niessen, "Satellite Configuration for EHF Communications for Mobile Terminals", 1981 International Telemetry Conference, San Diego Cal, proceedings, October 1981.
- [5] D.R. McElroy, "EHF System Concepts for Serving Mobile Users", 9th AIAA ComSatSysCon, San Diego Cal., March, 1982; AIAA paper 82-0489.
- [6] R.R. Rhodes, "Use of Surface Acoustic Wave Reflective Array Compressors in Spectrum Analysis and Demodulation "; EASCON '79 record, October 1979; IEEE # CH1476-1/79/0000-0283
- [7] P. Ma, "On Frequency Offsets in Windowed Reception of Frequency Dehopped M-ary FSK Signals for Multi-user Systems". Proceedings MILCOM'84, Los Angeles, Ca., October 1984
- [8] DSS file no. W8477-7-TB06/01-SV. Com Dev Report "Design, Fabrication & Test of SAW Devices For A Low Data Rate (LDR) Demodulator Acceptance Test Procedure". April 26, 1989
- [9] DSS file no. W8477-7-TB06/01-SV. Com Dev Report "Design, Fabrication & Test of SAW Devices For A Low Data Rate (L.D.R.) Demodulator Final Device Design Report". April 26, 1989
- [10] M.A. Jack, P.M. Grant, J.H. Collins, "The Theory, Design, and Applications of Surface Acoustic Wave Fourier-Transform Processors", Proceedings of the IEEE, Vol. 68, No. 4, pp.450-468, April 1980.

- [11] O.W. Otto, "The Chirp Transform Signal Processor", 1976 Ultrasonics Symposium Proceedings, pp. 365-370; IEEE Cat. # 76CH1120-5SU.
- [12] R.H. Trancell, M.G. Holland, "Acoustic Surface Wave Filters", Proceedings of the IEEE, Vol. 59, No. 3, pp. 393-409, March 1971.
- [13] H. Matthews (Ed.), Surface Wave Filters Design, Construction, and Use, John Wiley & Sons, New York, 1977
- [14] V. Ristic, Principles of Acoustic Devices, John Wiley & Sons, New York, 1983
- [15] R.F. Pawula, S.O. Rice, J.H. Roberts, "Distribution of the Phase Angle Between Two Vectors Perturbed by Gaussian Noise", IEEE Transactions on Communications, Vol. Com-30, pp. 1828-1841, August 1982.
- [16] R.F. Pawula, "On the M-ary DPSK Transmission Over Terrestrial and Satellite Channels", IEEE Transactions on Communications, Vol. Com-32, pp.752-761, July 1984.
- [17] R.F. Pawula, "Offset DPSK and a Comparison of Conventional and Symmetric DPSK with Noise Correlation and Power Imbalance", IEEE Transactions on Communications, Vol. Com-32, pp.233-240, March 1984.
- [18] P.H. Wittke, P.J. McLane and P. Ma, " Study of the Reception of Frequency De-hopped M-ary FSK", Research Report No. 83-1, Dept. of Electrical Engineering, Queen's University, Kingston, Ontario.
- [19] P.H. Wittke, P.J. McLane and P. Ma, "On Phase Noise and Frequency Offsets in the Reception of Frequency Dehopped M-ary FSK" MILCOM '83, Washington, D.C., pp. 220-224, Oct., 1983.
- [20] R.C. Williamson, V.S. Dolat, R.R. Rhodes, D.M. Boroson, "A Satellite-Borne SAW Chirp-Transform System for Uplink Demodulation of FSK Communications Signals", Ultrasonics Symposium Proceedings, pp.741-747, September 1979.
- [21] M. Jeruchim, "Techniques for Estimating the Bit Error Rate in the Simulation of Digital Communications Systems", IEEE Journal on Selected Areas of Communications, Vol. sac-2 No. 1, January 1984

- [22] G. Boudreau, "Differential Detection of Doubinary Minimum Shift Keying", M.Sc. Thesis, Queen's University, Kingston, Ontario, August, 1984
- [23] L. Mason, "Computation of the Probability Distribution function (pseudo-distribution function) derived by Pawula, Rice, and Roberts" written in Vax Fortran, 1986.
- [24] L.S. Metzger, D.M. Boroson, J.J. Urhan, "Receiver Windowing for FDM MFSK Signals", IEEE Trans. Comm., Vol. COM-27, pp. 1519-1526, October 1979
- [25] M. Jack, J.H. Collins, "Fast Fourier Transform Processor Based on the SAW Chirp Transform Algorithm", Ultrasonics Symposium Proceedings, 1978; IEEE Cat. # 78CH 1344-1SU
- [26] L. B. Milstein, Pankaj K. Das, "Surface Acoustic Wave Devices", IEEE Communications Magazine, pp.25-33, September 1979.
- [27] J.G. Proakis, Digital Communications, McGraw-Hill, London, 1987.

Appendix A

A.1 SAW Propagation and SAW Devices

This Appendix provides a simplified technique to synthesize an arbitrary impulse response for a surface acoustic wave device. A brief physical description of SAW propagation is given, followed by an analytical impulse response model. Finally, some implementation considerations are outlined and a numerical example is given. The following material is intended to be tutorial in nature and follows the more detailed analyses provided in [12], [13], and [14].

In [14] it is shown that propagation of an acoustic wave through an isotropic media in an arbitrary direction (taken as the z direction) can be described as a combination of three propagating waves, governed by the wave equations

$$\frac{\partial^2 u_x}{\partial t^2} - v_s^2 \frac{\partial^2 u_x}{\partial z^2} = 0 \quad (\text{A.1a})$$

$$\frac{\partial^2 u_y}{\partial t^2} - v_s^2 \frac{\partial^2 u_y}{\partial z^2} = 0 \quad (\text{A.1b})$$

$$\frac{\partial^2 u_z}{\partial t^2} - v_L^2 \frac{\partial^2 u_z}{\partial z^2} = 0 \quad (\text{A.1c})$$

where

$u_i = u(i,t)$, the i -direction , time dependent displacement of an acoustic particle

v_s is the shear direction acoustic wave velocity

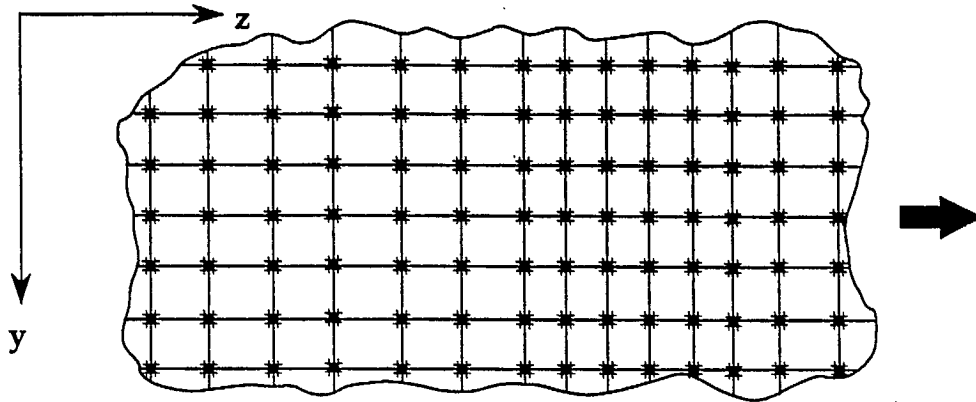
and

v_L is the longitudinal acoustic wave velocity.

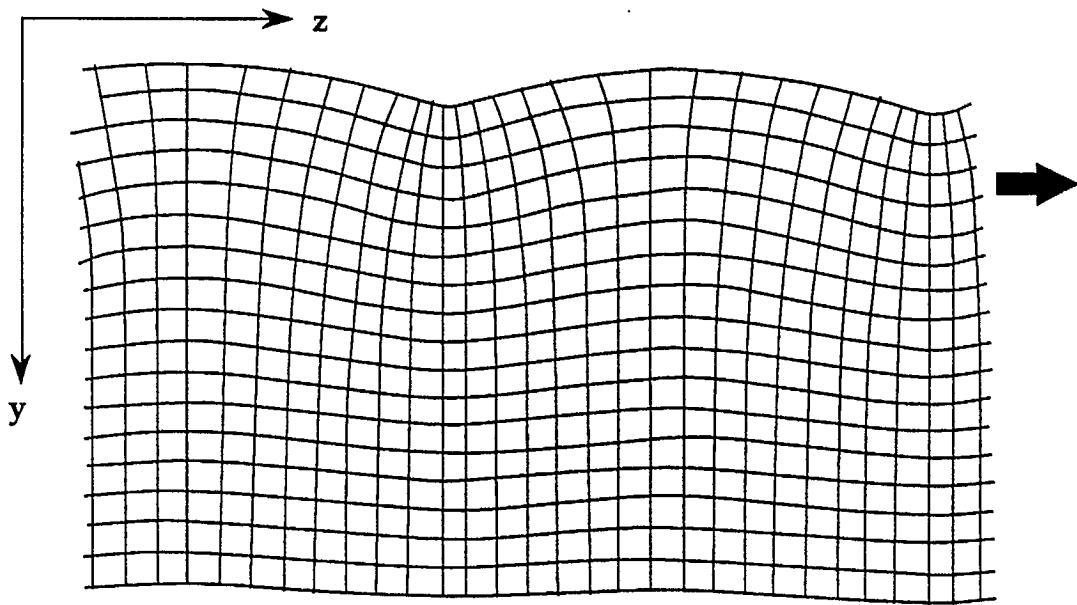
The first two equations represent shear (transverse) waves which are x and y polarized and propagate in the z -direction with velocity v_s . The third equation describes a longitudinal wave propagating in the z direction with velocity v_L .

In general, excitation of an acoustic material will result in generation of both bulk acoustic waves (BAW) and Rayleigh, or surface acoustic waves (SAW). Under certain boundary conditions the combined shear and longitudinal waves are coupled at the boundary surface of the acoustic media and mechanically free surface, and decay rapidly with depth into the acoustic media (y -direction). Thus, the acoustic energy is concentrated at or near this free surface in the form of SAWs and bulk wave generation is minimal. In anisotropic materials the analysis of SAWs is complicated by the directional dependence of some physical parameters but the results are similar. Figure A.1 illustrates a SAW propagating in the z -direction. Note that in the bulk regions of the crystal the wave barely exists.

Figure A.1 Propagation of an Acoustic Wave



a) propagation of a bulk acoustic wave in an isotropic solid represented as grid points



b) SAW propagation in an isotropic media

Figure redrawn from [26]

Analysis of SAW propagation is further complicated when the acoustic media has piezoelectric properties. Piezoelectricity is a linear property of certain materials that results in an electric polarization when the material is subjected to mechanical stress. The inverse piezoelectric effect is the reciprocal phenomena; an applied electric field produces a deformation in the material.

This electromechanical coupling is used in both the generation and detection of surface acoustic waves, and is usually achieved by deposition of a metallic electrode structure on the piezoelectric substrate. Thus a voltage applied across such an electrode will create distortions in the piezoelectric crystal which give rise to travelling (acoustic) waves. In the reciprocal arrangement, a SAW incident on an electrode will induce a voltage across it.

The presence of this conducting electrode will affect the velocity of the acoustic wave. When the surface of the crystal is metallized, the electromechanical coupling of the piezoelectric effect is removed and the SAW propagates at a reduced velocity. Strength of the piezoelectric effect can be measured relative to its effect on the acoustic wave velocity. The piezoelectric coupling factor, K^2 , sometimes referred to as the electromechanical coupling coefficient, is defined as

$$K^2 = 2 \frac{\Delta v}{v_r} \quad (\text{A.2a})$$

where

v_r is the SAW velocity with no conducting layer present

v_o is the velocity with a conducting layer present

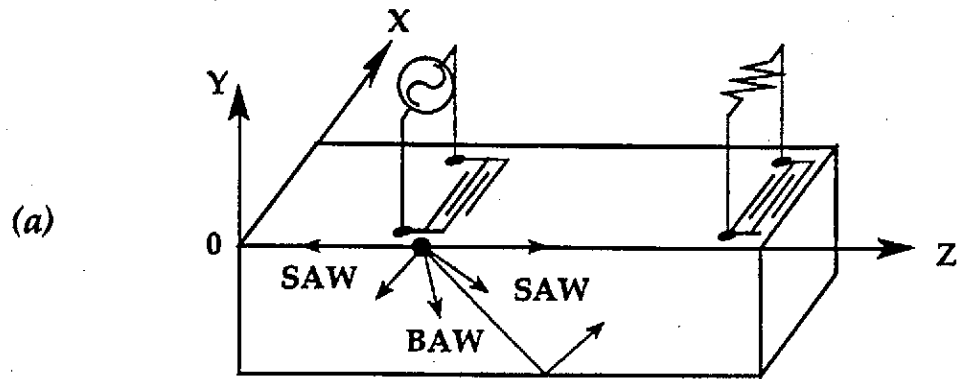
and

$\Delta v = v_r - v_o$ is the difference in velocity (A.2b)
produced by shorting the free surface.

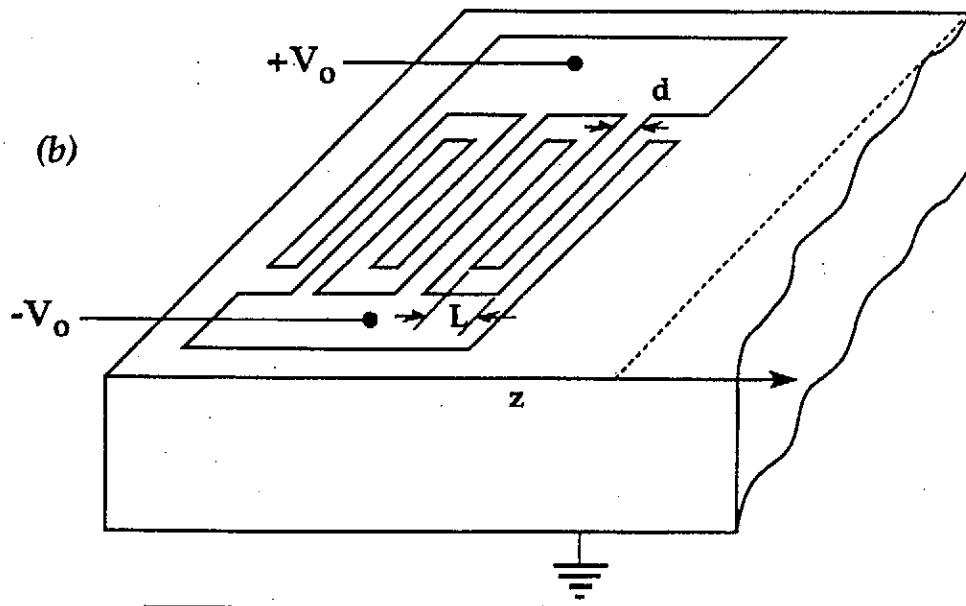
The most commonly used electrode structure is known as the interdigital transducer (IDT); an example is shown in Figure A.2. It consists of, in this case, a spatially periodic array of uniform conducting electrodes. Application of an a.c. electric potential across the electrodes results in generation of periodic mechanical strains on the crystal surface (SAW) and in the substrate (BAW). Acoustic waves incident on a similar transducer will generate electric potentials and RF currents in the output electrodes which can be connected to an external electrical load.

In the following analytical approximation it is assumed that the length of each finger in the transverse (x-direction) is much larger than the Rayleigh wavelength so diffraction effects can be neglected ($\partial/\partial x \approx 0$). It is also assumed that the only non-zero displacement component of the SAW corresponds to the longitudinal (z) direction.

Figure A.2 The Interdigital Transducer



a) A saw device with input and output IDT



b) A uniform IDT with electrode width d and spatial period L

Figure redrawn from [14]

Using these assumptions, with appropriate boundary conditions, Ristic [14] develops the following wave equation

$$\frac{\partial^2 u}{\partial z^2} - (1/v_r^2) \frac{\partial^2 u}{\partial t^2} = B\sigma(t, z) \quad (\text{A.3})$$

where

v_r is the SAW velocity

$\sigma(t, z)$ is the spatial and time dependent charge density

and

B is a constant.

In equation A.3, the time/space variables in $\sigma(t, z)$ can be separated so

$$\sigma(t, z) = \sigma_1(z)\sigma_2(t). \quad (\text{A.4})$$

The characteristics of the spatially dependent charge density, $\sigma_1(z)$, depend on the analytical model being used, which in turn depend on the device region considered.

In regions where the longitudinal electric field (E_z) is predominant, such as in the electroded region(s) of the transducer, the "in-line" model is used. In regions without metallization the transverse electric field (E_y) is predominant and the "cross field" model is used. Figure A.3 illustrates the electric field assumed in both

Figure A.3 The Crossed Field and In-line Electric Field Approximations

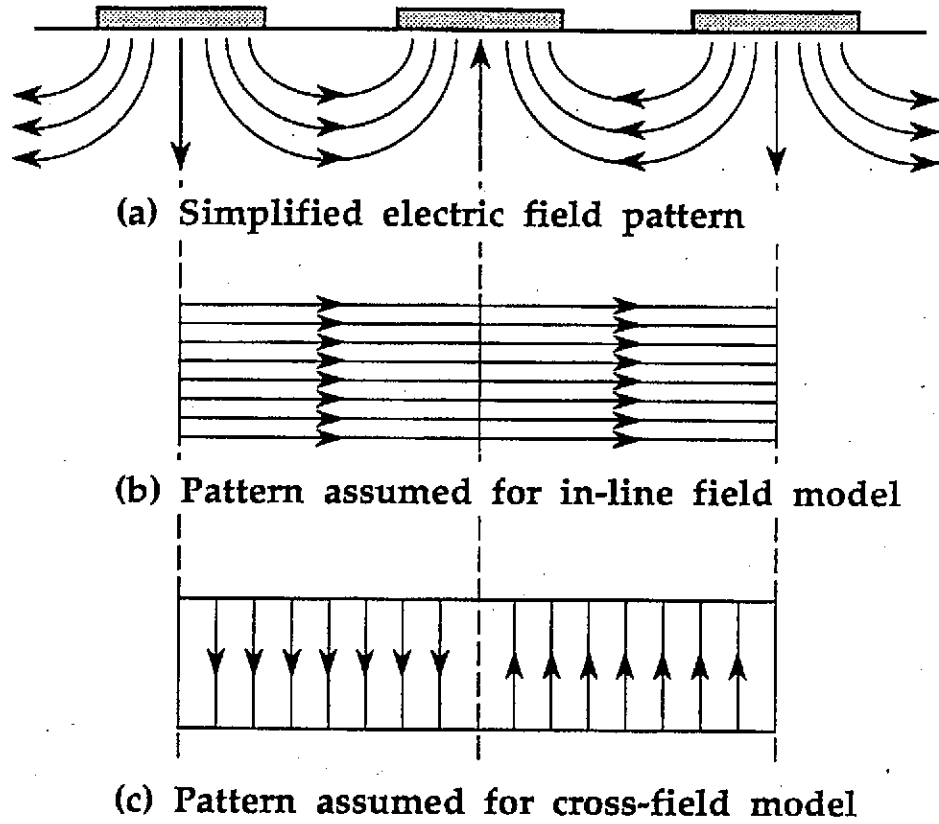


Figure redrawn from [13]

approximations. Thus $\sigma_1(z)$ is given by

$$\sigma_1(z) = \begin{cases} A_1 \partial E_z(z) / \partial z & \text{for the "in line" approximation} \\ A_2 E_y(z) & \text{for the "cross field" approximation} \end{cases} \quad (\text{A.5})$$

where A_1 and A_2 are constants.

Since the response outside the electroded regions determines the transducer response, the cross field approximation is used in this analysis. The resulting wave equation is then given by

$$\frac{\partial^2 u}{\partial z^2} - (1/v_r^2) \frac{\partial^2 u}{\partial t^2} = BA_2 \sigma_2(t) E_y(z). \quad (\text{A.6})$$

For impulse excitation, $\sigma_2(t) = \delta(t)$ and the solution to A.6 becomes

$$u_z(t, z) = A_0 \int_{-\infty}^{\infty} U\left(t - \frac{|z-\zeta|}{v_r}\right) E_y(\zeta) d\zeta \quad (\text{A.7a})$$

where

$$U(t) = \begin{cases} 1 & \text{for } t \geq 0 \\ 0 & \text{otherwise.} \end{cases} \quad (\text{A.7b})$$

and integration is performed over $0 < \zeta < Z$, where Z is the z -direction length of the transducer region.

The electric field, E_y , can be modelled in many ways, depending on the complexity required; [13] lists several. Figure A.4 illustrates the resulting electric field for a given IDT structure, and the corresponding double and single delta function models. In this study, the double delta function model will be used and analysis will be performed as in [12]. Following this presentation, the position of the m^{th} electrode edge can be expressed as

$$E_y(\zeta) = E_y^0 \delta(z - z_m) \quad (\text{A.8})$$

where E_y^0 is the value of the electric field at the electrode edge. Consequently, equation A.7 can be expressed (from [14]) as

$$u_z(t, z) = A_0 u(z - z_m) \quad (\text{A.9})$$

where A_0 is a constant proportional to E_y^0 .

According to this model, the edge of each finger radiates a wave travelling in both positive and negative z -directions. Only those waves travelling in the positive z direction are considered here.

Figure A.4 $E_y(z)$ for a uniform IDT

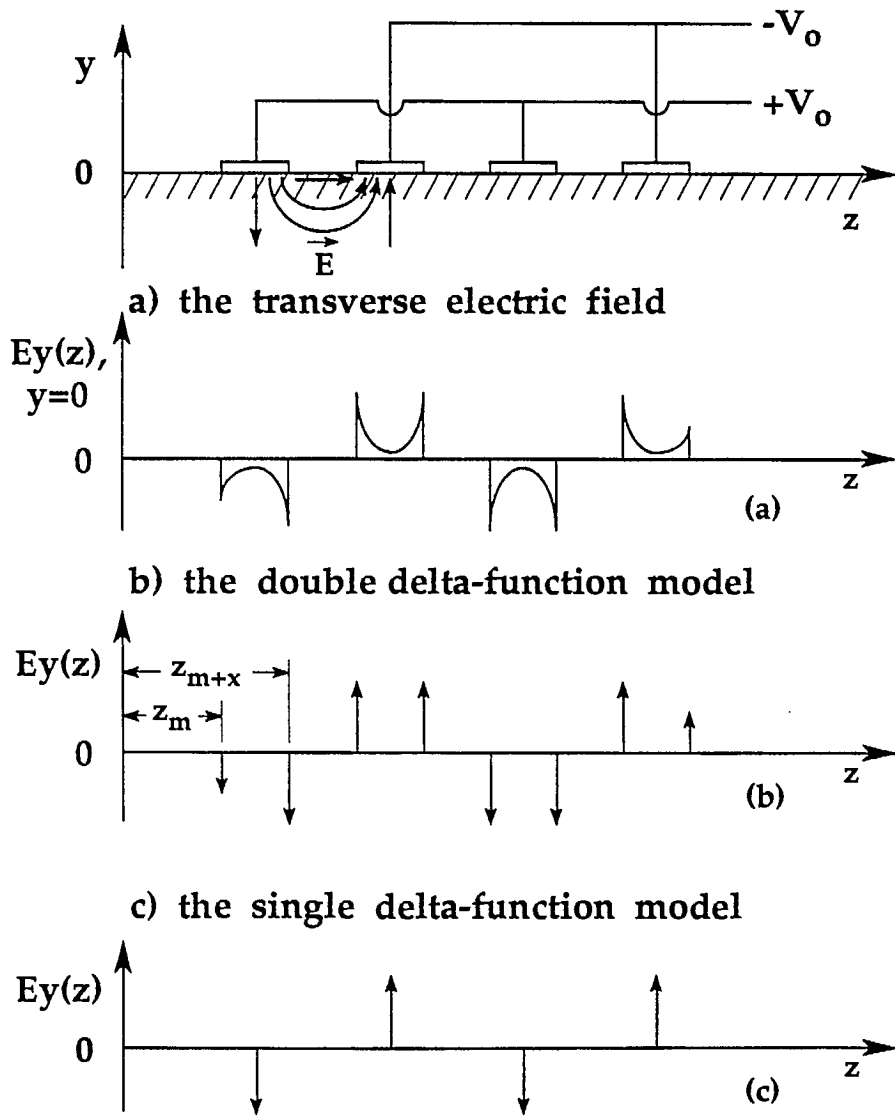


Figure redrawn from [14]

The impulse response of any IDT can be approximated using the double delta-function model as

$$h(t) = \sum_{m=1}^M I_m \delta(z - z_m). \quad (\text{A.10})$$

where

M = the number of electroded edges

z_m = the position of each electrode edge

and

I_m = an amplitude term proportional to the electric field gradient.

Making the substitution $z = tv_r$ in (A.10) results in

$$h(t) = \sum_{m=1}^M I_m \delta(t - z_m/v_r). \quad (\text{A.11})$$

The Fourier transform of $h(t)$ in (A.11) results in

$$H(f) = \sum_{m=1}^M I_m e^{-j2\pi f(z_m/v_r)}. \quad (\text{A.12})$$

This implies that the transfer function of a SAW device using an input/output IDT combination can be expressed as

$$H_T(f) = \frac{V_o(f)}{V_i(f)} = \sum_{m=1}^M \sum_{n=1}^N I_n I_m e^{-j2\pi f(z_m - \epsilon_n)/v} \quad (\text{A.13})$$

where

$V_o(f)/V_i(f)$ is the ratio of output to input voltage as a function of frequency f

ϵ_n is the distance (measured from $z=0$) to the n^{th} edge on the output transducer

and

$v = v_r$ is the SAW velocity.

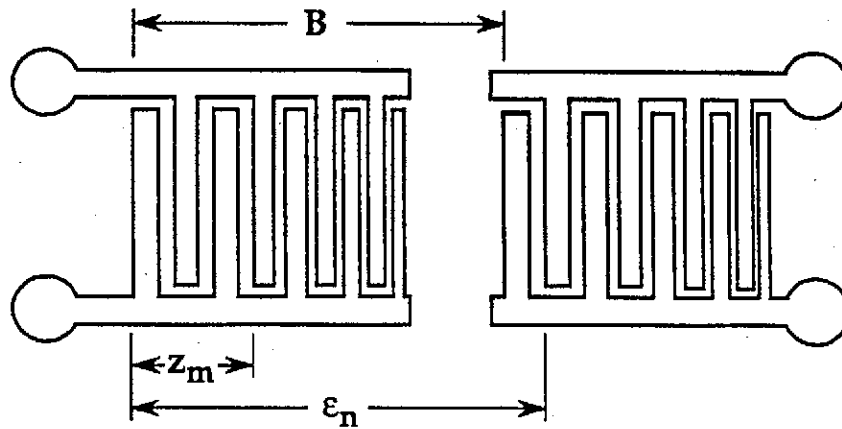
Figure A.5 illustrates two special cases of a transfer function given in the form of equation (A.13). In the first case (A.5a) the double sum of A.13 can be split into two single sums, so using $\epsilon_n = B + z_n$

$$H_T(f) = \left[\sum_{m=1}^M I_m e^{-j2\pi f z_m / v} \right] \left[\sum_{n=1}^N I_n e^{j2\pi f z_n / v} e^{j2\pi f B / v} \right] \quad (\text{A.14})$$

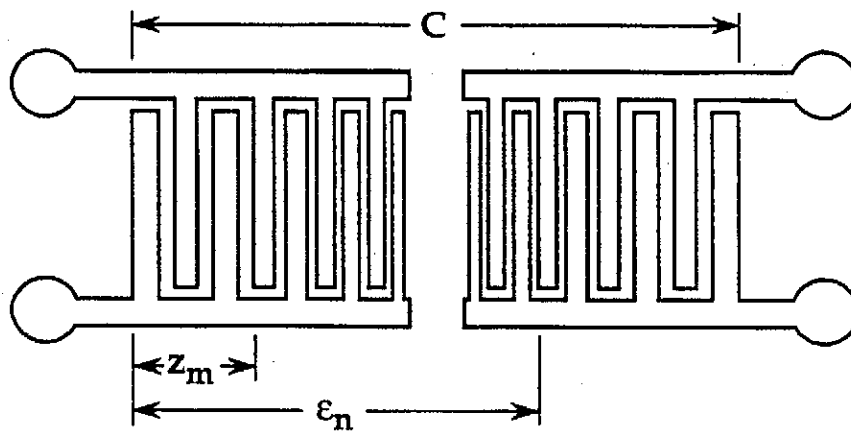
$$= \left| \sum_{m=1}^M I_m e^{-j2\pi f z_m / v} \right|^2 e^{j2\pi f B / v} \quad (\text{A.15})$$

Note that this response is a function of the square of the magnitude term, thus it is dispersionless regardless of the finger positioning. In Figure A.5b the transducers are mirror images, so using

Figure A.5 Input/Output IDT pairs



(a) Comb structure with no dispersion



(b) Comb structure with dispersive delay

Figure redrawn from [12]

$\epsilon_n = C - z_n$, the device transfer function in this case becomes

$$H_T(f) = \left[\sum_{m=1}^M I_m e^{-j2\pi f z_m / v} \right]^2 e^{-j2\pi f C / v} \quad (\text{A.16})$$

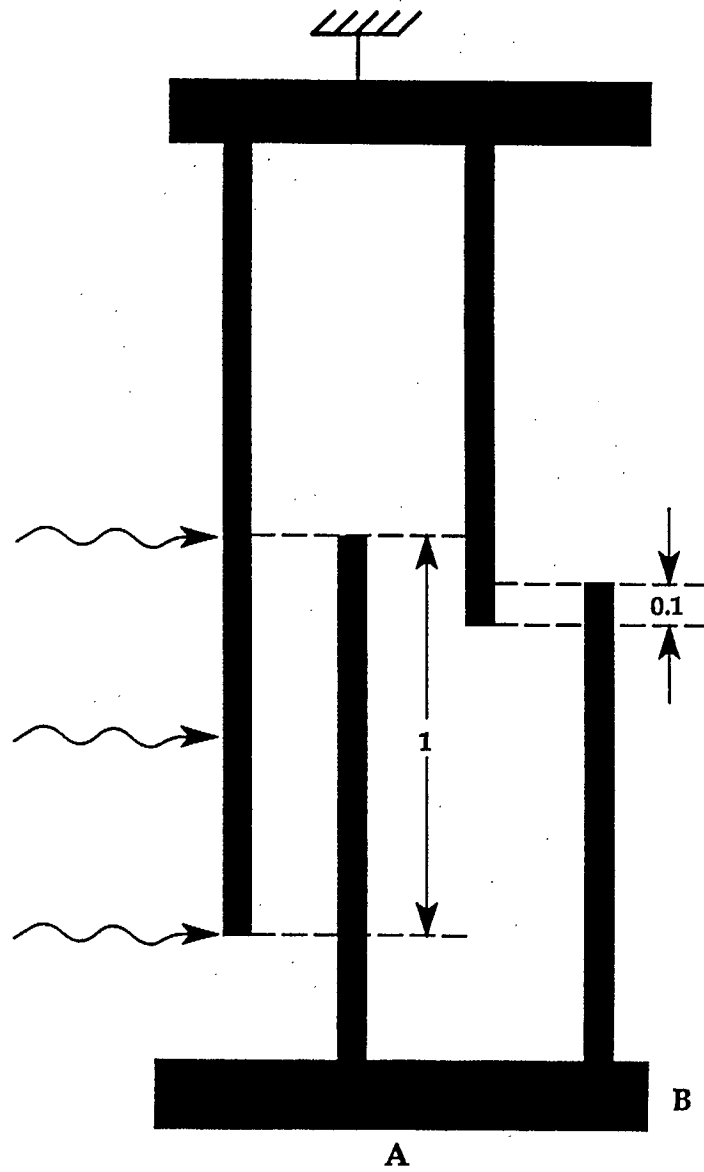
In equation A.16 the quantity in brackets is, in general, complex so the transfer function may be dispersive in frequency.

Consider the arbitrary device response given as

$$H_T(f) = \sum_{k=1}^K A_k e^{-j2\pi f z_k / v} \quad (\text{A.17})$$

To achieve this response, the phase and amplitude of each δ -function source must be adjustable. Phase is varied by changing the finger positions and polarity. To achieve an arbitrary amplitude a technique known as apodization is used. By varying the overlap of neighboring, opposite polarity electrodes, the acoustic energy generated is concentrated in the overlapping regions. An example of apodization is shown in the finger-pair overlap illustrated in Figure A.6. Here, an incident surface acoustic wave will induce ten times the voltage in "pair A" that it will in "pair B", where the SAW is assumed to have the same transverse dimensions as the overlap in finger-pair A .

Figure A.6 Finger-pair overlap (apodization) to achieve an arbitrary amplitude response



The voltage generated in "pair A" will be ten times the voltage generated in "pair B".

Figure redrawn from [26]

Figure A.7 illustrates an example of an apodized input/output IDT pair, or comb. If the overlap function of the transmitter comb is $w(z)$, and for the receiver comb is $g(\epsilon_n)$, then

$$H_T(f) = \sum_{m=1}^M \sum_{n=1}^N C_{n,m} B_n B_m e^{-j2\pi f(z_m - \epsilon_n)/v} \quad (\text{A.18})$$

where

$$C_{n,m} = \begin{cases} w(z_m) & \text{if } w(z_m) < g(\epsilon_n) \\ g(\epsilon_n) & \text{if } g(\epsilon_n) < w(z_m) \end{cases} \quad (\text{A.19})$$

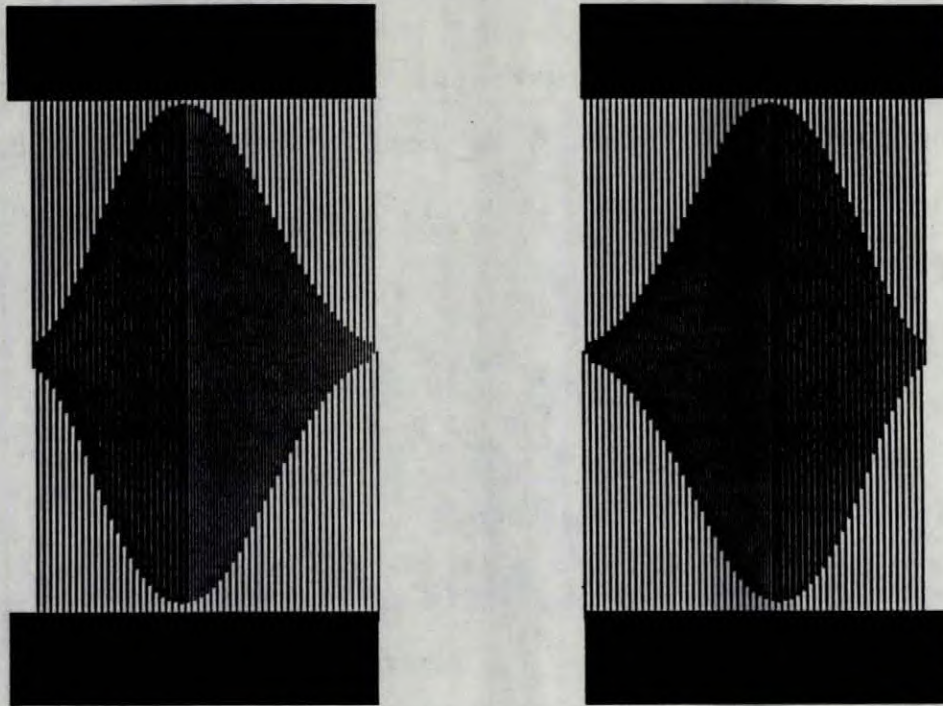
Because of the $C_{n,m}$ term, (A.18) does not, in general, split into two separate sums. As a consequence, the overall transfer function of an amplitude apodized device is not, in general, the product of the frequency responses of each comb. For the case of two similar apodized combs as shown here, [12] suggests deriving an approximately equivalent expression by visually breaking the transmitter-receiver pairs into strips as shown in Figure A.7b, then

$$H_T(f) = \sum_{k=1}^K \left[\sum_{m=1}^M B_m^k e^{-j2\pi f z_m / v} \right]^2 \quad (\text{A.21a})$$

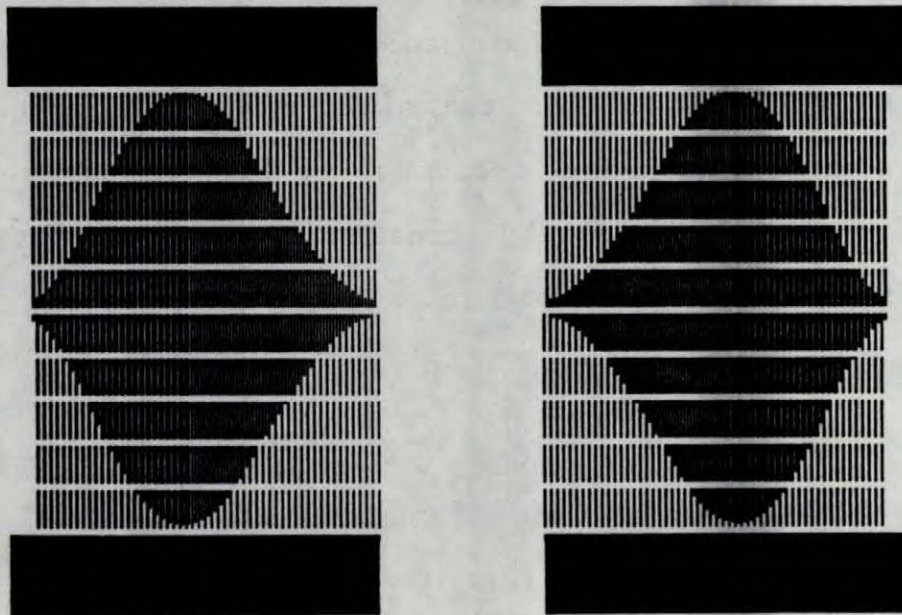
where

$$B_m^k = \begin{cases} \pm 1 & \text{if } |w(z_m)| > k/K \\ 0 & \text{if } |w(z_m)| < k/K \end{cases} \quad (\text{A.21b})$$

Figure A.7 An Input/Output Amplitude Apodized IDT pair



a) Input/Output IDT pair with amplitude apodization



b) Visually breaking the combs into unapodized segments

Figure redrawn from [12]

For the case where one comb is unapodized, equation A.18 reduces to

$$H_T(f) = \left[\sum_{k=1}^K w(z_m) B_m e^{-j2\pi f z_m / v} \right] \{ \gamma \} \quad (\text{A.22})$$

where γ is the broadband response of the unapodized comb, which is assumed to be broadband and is approximately a constant. Such a broadband comb is usually implemented with a small number of fingers (2 or 4).

The double delta function model will now be used to determine the finger placement and apodization rules for the design of an IDT comb. This procedure closely follows the technique used in [12].

Consider the infinite series of impulses which can be expressed as

$$\sum_{n=-\infty}^{\infty} \delta(\epsilon - n) = \sum_{n=0}^{\infty} E_n \cos(2\pi n \epsilon) \quad (\text{A.22a})$$

where

$$E_n = \begin{cases} 1 & \text{for } n = 0 \\ 2 & \text{for } n \neq 0 \end{cases} \quad (\text{A.22b})$$

and ϵ is a distance measured along the z direction.

Multiplying both sides by $\cos(2\pi \epsilon / \pi - \pi/4)$ and making the

substitution $\varepsilon = mg(z)$, where m is a non-zero integer, results in

$$\begin{aligned} & \sum_{n=-\infty}^{\infty} \cos(2\pi g(z) - \pi/4) \delta(mg(z) - n) \\ = & \sum_{n=0}^{\infty} E_n \cos(2\pi mng(z)) \cos(2\pi g(z) - \pi/4). \end{aligned} \quad (\text{A.23})$$

In (A.23), $g(z)$ can be interpreted as the instantaneous phase of the R.F. signal. Making use of the properties of the δ -function

$$\delta(mg(z) - n) = \delta(z - z_n) / |mg'(z_n)| \quad (\text{A.24a})$$

where

$$g(z_n) = n/m \quad (\text{A.24b})$$

and

$$g'(z) = dg(z)/dz. \quad (\text{A.24c})$$

Note that $g(z)$ is a monotonically increasing function so $|g'(z_n)| = g'(z_n)$.

To account for the finite duration of the IDT comb, multiply both sides of A.23 by the envelope function $e(z)$, where $e(z) = 0$ for $z > Z$. Also make the substitution given by (A.24) to get

$$\begin{aligned}
& \sum_{n=-\infty}^{\infty} e(z) \cos(2\pi g(z) - \pi/4) \delta(z - z_n) / mg'(z) \\
&= \sum_{n=0}^{\infty} e(z) E_n \cos(2\pi n g(z)) \cos(2\pi g(z) - \pi/4). \quad (\text{A.25})
\end{aligned}$$

Taking the Fourier transform of both sides of (A.25) results in

$$\text{L.H.S.} = \sum_{n=-\infty}^{\infty} \frac{e(z_n)}{mg'(z_n)} \cos(2\pi n/m - \pi/4) e^{-jkz_n} \quad (\text{A.26a})$$

$$\text{R.H.S.} = \int_{-\infty}^{\infty} \sum_{n=0}^{\infty} e(z) E_n \cos(2\pi n g(z)) \cos(2\pi g(z) - \pi/4) e^{-jkz} dz \quad (\text{A.26b})$$

where $k = 2\pi f/v$.

Setting $m = 4$ so that the polarity of the delta functions alternates in pairs, these equations become

$$\text{L.H.S.} = \sum_{n=-\infty}^{\infty} \frac{e(z_n)}{4g'(z_n)} \cos(\pi n/2 - \pi/4) e^{-jkz_n} \quad (\text{A.27a})$$

$$\text{R.H.S.} = \int_{-\infty}^{\infty} \sum_{n=0}^{\infty} e(z) E_n \cos(8\pi n g(z)) \cos(2\pi g(z) - \pi/4) e^{-jkz} dz. \quad (\text{A.27b})$$

Equation A.27b can be expressed as the sum of two cosine terms so that

$$\begin{aligned} \text{R.H.S.} = \int_{-\infty}^{\infty} \frac{1}{2} \sum_{n=0}^{\infty} e(z) E_n \left\{ \cos \left(2\pi g(z) (4n+1) - \pi/4 \right) \right. \\ \left. + \cos \left(2\pi g(z) (4n-1) + \pi/4 \right) \right\} e^{-jkz} dz. \end{aligned} \quad (\text{A.28})$$

Equation A.27a can be interpreted as the transfer function of the transducer $H_T(f)$ by expressing it as

$$H_T(f) = \sum_{n=-\infty}^{\infty} A_n e^{-j2\pi f z_n / v} \quad (\text{A.29a})$$

where

$$A_n = \pm (2)^{-\frac{1}{2}} e(z_n) / 4g'(z_n) \quad (\text{A.29b})$$

and the polarity of A_n alternating in pairs .

Expanding the summation of A.28 results in

$$\begin{aligned} \text{R.H.S.} = \int_{-\infty}^{\infty} e(z) \cos \left(2\pi g(z) - \pi/4 \right) e^{-jkz} dz \quad (\text{A.30}) \\ + \int_{-\infty}^{\infty} e(z) \cos \left(6\pi g(z) + \pi/4 \right) e^{-jkz} dz \\ + \int_{-\infty}^{\infty} e(z) \cos \left(10\pi g(z) - \pi/4 \right) e^{-jkz} dz + \text{etc.} \end{aligned}$$

The higher order harmonics will be attenuated by the frequency dependent attenuation of the substrate, and can be further reduced by filtering, thus only the fundamental

component is significant and (A.30) becomes

$$\int_{-\infty}^{\infty} e(z) \cos(2\pi g(z) - \pi/4) e^{-jkz} dz \quad (\text{A.31})$$

which can be interpreted as the Fourier transform of the impulse response

$$h(t) = e(t) \cos(2\pi g(t) - \pi/4). \quad (\text{A.32})$$

As an implementation example, the apodization and finger placement rules will be determined for a linearly chirped waveform with a rectangular envelope. In this case

$$g(t) = 2\pi f_0 t \pm \frac{1}{2} \mu t^2 \quad (\text{A.33a})$$

so

$$g(z/v) = (1/\lambda)z + \frac{1}{2} \beta z^2 \quad (\text{A.33b})$$

and

$$e(z) = \begin{cases} 1 & \text{for } 0 \leq z \leq Z \\ 0 & \text{otherwise.} \end{cases} \quad (\text{A.33c})$$

In (A.33) the substitutions $\lambda = f_0/v$ and $\beta = \pm\mu/v^2$ have been used.

Using equations A.24 and A.29, the finger placement rule becomes

$$z_n = \begin{cases} v f_0 / \mu \left[-1 + \sqrt{1 + \frac{n}{2} (\mu / f_0^2)} \right] & \mu > 0 \\ -v f_0 / \mu \left[-1 + \sqrt{1 - \frac{n}{2} (\mu / f_0^2)} \right] & \mu < 0 \end{cases} \quad (\text{A.34a})$$

$$|A_n| = \begin{cases} (2)^{-1/2} \left[4 \left(v / f_0 + (\mu / v^2) z_n \right) \right]^{-1} & \mu > 0 \\ (2)^{-1/2} \left[4 \left(v / f_0 - (\mu / v^2) z_n \right) \right]^{-1} & \mu < 0. \end{cases} \quad (\text{A.34b})$$

An example of the determined values of A_n , and the resulting waveform are shown in Figures A.8a and A.8b.

Some implicit assumptions and simplifications have been made in this derivation. It has been assumed that the samples (fingers) are taken at uniform phase intervals of 90° . Physically this implies that the finger width is equal to the finger spacing, and with this width varying as the spacing z_n (as is shown in Figure A.5). That is, d/L is equal to $1/2$, where d and L are defined by Figure A.2. In determining the apodization, frequency dependent propagation losses have also been ignored. Generally, these losses occur as

$$P(t) = P_0 e^{-\alpha(f)z} \quad (\text{A.35})$$

where

$P(t)$ is the acoustic power at time t

f is the frequency

and

P_0 is the acoustic power at time $t = 0$.

Figure A.8 Chirped waveform and corresponding impulse amplitudes

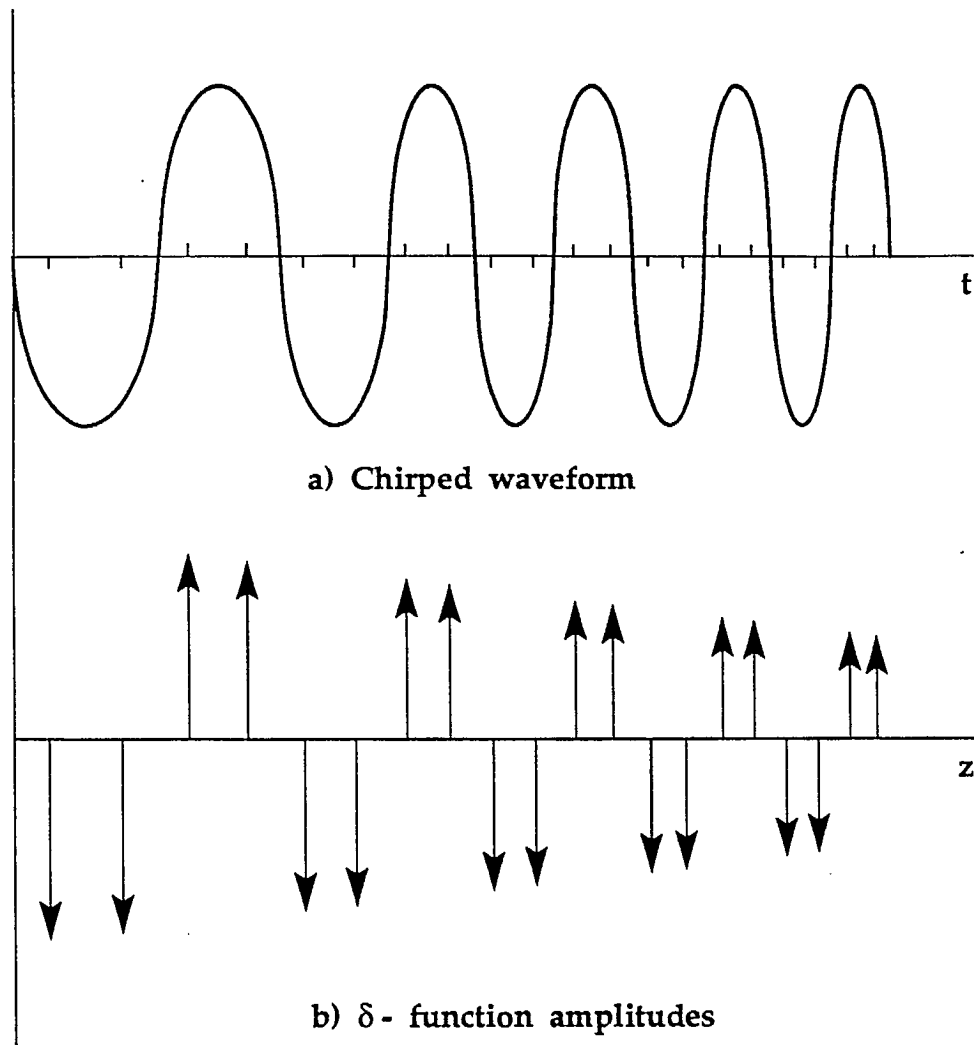


Figure redrawn from [12]

When this effect is accounted for, the values of A_n in (A.34b) must be modified accordingly.

A.2 Implementation Considerations

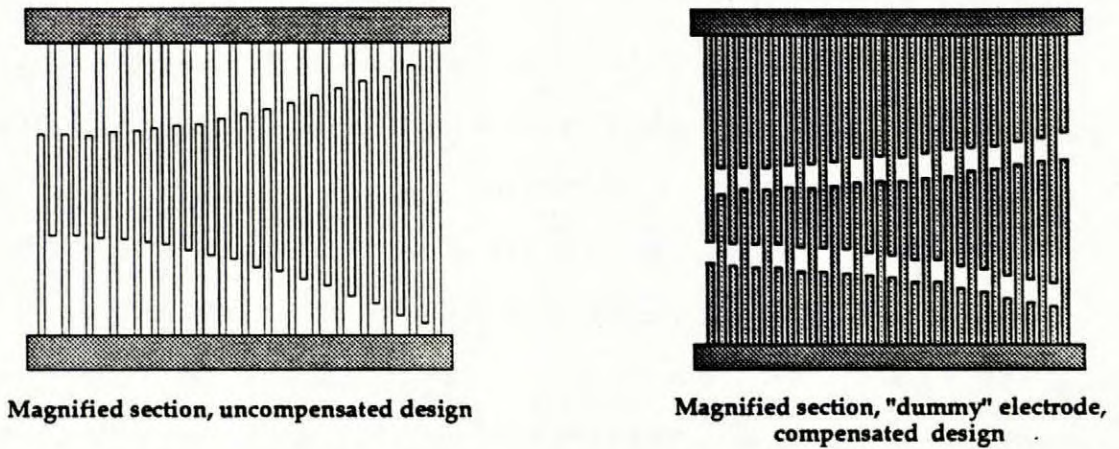
For the chirped waveform impulse response that was just specified, two other significant effects have been ignored. The SAW velocity used in this formulation has been assumed to be constant over the transducer region. However, as noted earlier, the presence of the metallized electrodes affects this velocity. This implies that an iterative design procedure must be used for accurate phase results. For a first approximation, an effective velocity, v_T , can be used in the transducer region where

$$v_T = 2v_o v_r / (v_o + v_r). \quad (\text{A.36})$$

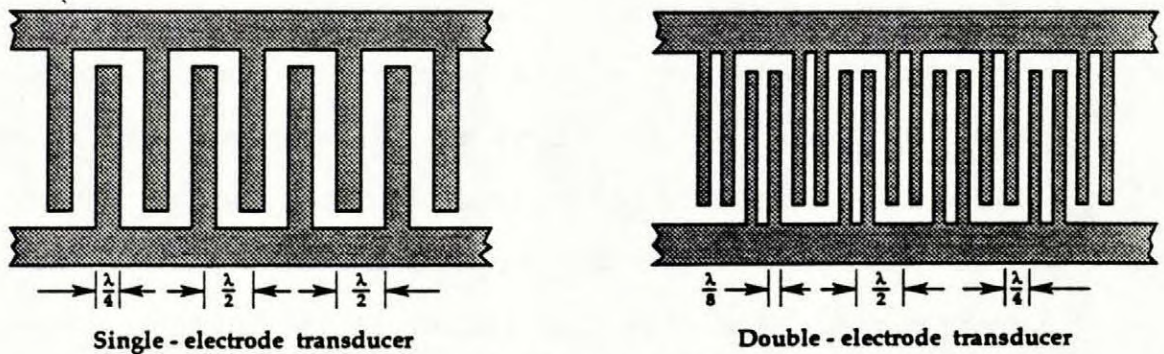
This velocity variation can have more pronounced effects as well. Because $v_r < v_o$, amplitude apodization will result in a curvature of the wavefront corresponding to the finger overlap. To overcome this problem, "dummy" electrodes can be inserted. These electrodes, as are shown in Figure A.9a, do not effect the transducer response, but help provide a constant velocity profile for the SAW.

Another adverse effect caused by electrode deposition is the possibility of acoustic wave reflection at each

Figure A.9 "Dummy" and double electrode structures



a) A comparison of electrode geometry with and without "dummy" electrode wavefront compensation



b) A comparison of single and double electrode configurations

Both Figures redrawn from [13]

electrode. This is a particularly serious problem for chirp filters since the electrodes are usually placed half an acoustic wavelength apart, resulting in coherent addition of reflected waves.

There are two common methods of overcoming this problem. The first is to use a weakly coupling piezoelectric substrate so that the reflections are small. The second technique is to use a "double electrode" structure as shown in Figure A.9b. In this case, two metal strips, which compromise one electrode, are placed on the quarter wavelength centers causing cancellation of reflections from adjacent strips.

A reflection problem also exists when the voltage generated in the output transducer is under an external load. In this case the load voltage across the output transducer will create another SAW which propagates to the input transducer and is similarly reflected, a phenomena known as triple transit echo (TTE). Because of this it is important to ensure that both input and output networks are well matched to the respective IDT characteristics.

Once the SAW device has been fabricated, care must be taken in mounting the crystal substrate. Any pressure incident on the piezoelectric crystal will effect its assumed electro-mechanical properties. Some form of acoustic absorption should also be included in this packaging to reduce the acoustic reflections that will occur at the

crystal interfaces (along the edges and bottom of the crystal).

It should also be noted that for some piezoelectric substrates (LiNbO_3 for instance), the SAW velocity is temperature dependent. For high accuracy applications these devices should be placed in a temperature stabilizing oven.

To conclude this discussion, physical parameters corresponding to the propagation of a SAW on the piezoelectric LiNbO_3 will be used to determine some numerical results for the $TB = 512$ and $TB = 1024$ SAW devices used in this study. It is assumed that the SAW propagates in the z-direction of Y-cut LiNbO_3 . It is also assumed that the input transducer in a broad-band comb of only one finger-pair.

For LiNbO_3 $v_r = 3488$ m/s and $K^2 = 0.048$. From equation A.36, this implies that $v_T = 3445$ m/s. For this application, a center frequency $f_0 = 100$ MHz is assumed and a dispersion $T = T_H = 50$ μsec is required. Using equations A.34a,b and these values, the critical device parameters, finger apodizations, and finger placements for a processor with $TB=512$ and a $TB=1024$ SAW device were determined and are given in Tables A.1 and A.2 respectively.

For TB = 512

$$\mu = 10.24 \text{ MHz} / 50 \text{ } \mu\text{sec} = 0.2048 \text{ MHz}/\mu\text{sec}$$

$$Z \cong v_{T_H} T_H = 17.23 \text{ cm}$$

Table A.1 Finger placements and Apodizations for the TB=512
chirped waveform filter

Finger edge	Z_m μm	A_m
1	8.612	A_0
2	17.22	$0.5A_0$
3	25.84	$0.33A_0$

For TB = 1024

$$\mu = 20.48 \text{ MHz} / 50 \text{ } \mu\text{sec} = 0.4096 \text{ MHz}/\mu\text{sec}$$

$$Z \cong v_{T_H} T_H = 17.23 \text{ cm}$$

Table A.2 Finger placements and Apodizations for the TB=1024
chirped waveform filter

Finger edge	Z_m μm	A_m
1	8.613	A_0
2	17.23	$0.499A_0$
3	25.84	$0.33A_0$

Note that sub micron resolution would be required to achieve the required device parameters. This implies that these large TB product devices cannot be implemented solely with an IDT structure. Another common device implementation, the reflective array compressor (RAC), would be capable of achieving these TB products, but a description of RAC implementation is beyond the scope of this study.

